

American Journal of Science

NOVEMBER 2008

THERMODYNAMICS OF RHOMBOHEDRAL OXIDE SOLID SOLUTIONS AND A REVISION OF THE FE-TI TWO-OXIDE GEOTHERMOMETER AND OXYGEN-BAROMETER

MARK S. GHIORSO*† and BERNARD W. EVANS**

ABSTRACT. A model for the thermodynamic properties of rhombohedral oxide solid solutions in the system $\text{Fe}_2\text{O}_3\text{-FeTiO}_3\text{-MgTiO}_3\text{-MnTiO}_3$ (containing minor amounts of Al_2O_3) is presented. The model accounts for temperature and compositionally dependent long-range cation-order and the related high to low symmetry structural phase transition. The model is calibrated from the cation-ordering data of Harrison and others (2000; Harrison and Redfern, 2001) and experimental data on $\text{Fe}^{+2}\text{Ti} \rightleftharpoons (\text{Fe}^{+3})_2$ exchange between rhombohedral oxide and spinel from Lattard and others (2005) and Evans and others (2006). Successful calibration require introduction of an energetic contribution attributed to short-range cation-order, which reduces the configurational entropy of the solid solution. The resultant thermodynamic model for the rhombohedral oxides is internally consistent with the model for spinel solid solutions of Sack and Ghiorso (1991a, 1991b) and with the endmember thermodynamic properties database of Berman (1988); a new model equation for the isobaric heat capacity of ulvöspinel (cubic Fe_2TiO_4) is proposed and values of the enthalpy of formation, -1490.417 kJ/mol , and third law entropy, 184.199 J/K-mol , at 298.15 K and 10^5 Pa are recommended.

The new model forms the basis of a revised Fe-Ti-oxide geothermometer/oxygen barometer, which is applied to a newly compiled dataset of natural two oxide pairs from silicic volcanic rocks. Results are compared to previous formulations with the general conclusion that the new model gives a better estimate of oxidation state for magmas that equilibrated under conditions more oxidizing than the nickel-nickel oxide buffer. Estimates of oxygen fugacity are fairly insensitive to analytical uncertainties in oxide compositions. By contrast, temperature estimates are especially sensitive to analytical error and to the abundances of “minor” constituents. Application of the geothermometer to oxide pairs that grew under conditions where the rhombohedral phase was cation disordered (that is high temperature or at oxygen fugacities greater by about one \log_{10} unit than the nickel-nickel oxide buffer) results in an uncertainty due solely to analytical error of at least 50°C and sometimes as high as 100°C . Temperature estimates from the new geothermometer can be made using either the $\text{Fe}^{+2}\text{Ti} \rightleftharpoons (\text{Fe}^{+3})_2$ exchange or $\text{Fe}^{+2} \rightleftharpoons \text{Mg}$ exchange between the two oxides. Comparison of the two temperature estimates provides a means of evaluating the internal consistency of coexisting oxide compositions and assessing the extent of disequilibrium. Temperatures calculated from the new model are found to be consistent with experimental phase relations for the stability of cummingtonite in silicic volcanics. Other petrologic constraints on derived temperatures are examined including limits on the width of the miscibility gap and the development of self-reversed remanent magnetization in the rhombohedral series.

Software that implements the new thermodynamic model and the two-oxide geothermometer/oxygen barometer is available from <http://www.ofm-research.org/>.

* OFM-Research—West, 7336 24th Avenue NE, Seattle, Washington 98115

** Department of Earth and Space Sciences, Box 351310, University of Washington, Seattle, Washington 98195-1310

† Corresponding author: ghiorso@ofm-research.org

INTRODUCTION

In this paper we develop a new thermodynamic model for rhombohedral oxide solid solutions in the system Fe_2O_3 - FeTiO_3 - MgTiO_3 - MnTiO_3 containing minor amounts of Al_2O_3 . The model is then applied to experimental data on coexisting rhombohedral oxide-spinel pairs in order to revise and correct the Fe-Ti oxide geothermometer and oxygen barometer calibration of Ghiorso and Sack (1991). The motivation for undertaking this study is two-fold. Firstly, since publication of the Ghiorso and Sack (1991) version of the geothermobarometer, high quality cation-ordering data have been collected for hematite-ilmenite solid solutions along the Fe_2O_3 - FeTiO_3 join (Harrison and others, 2000a, 2006; Harrison and Redfern, 2001). These data are at odds with previous measurements (Ishikawa, 1958) upon which the thermodynamic model of Ghiorso (1990a) was based; the Ghiorso (1990a) model is utilized in the Ghiorso and Sack (1991) calibration. Secondly, the geothermobarometer of Ghiorso and Sack (1991) has been found to overestimate the oxygen fugacity (f_{O_2}) of Mt. Pinatubo dacitic magma (Evans and Scaillet, 1997) and is suspected of overestimating both temperature (T) and (f_{O_2}) in most moderate- to highly-oxidized calc-alkaline magma series. Recent experimental data on coexisting rhombohedral and cubic (spinel) oxides (Lattard and others, 2005; Evans and others, 2006) confirm this suspicion and provide a high-quality data set for recalibration of the geothermobarometer over the temperature range 800° to 1300°C, and at oxidation state conditions plus or minus three \log_{10} units on either side of the nickel-nickel oxide (NNO) oxygen buffer.

THERMODYNAMICS OF HEMATITE-ILMENITE SOLID SOLUTIONS

Ghiorso (1990a, 1997) and Harrison and others (2000b; Harrison, 2006) summarize structural and magnetic features of hematite (Fe_2O_3)-ilmenite (FeTiO_3) solid solutions that influence the energetics of the series. The most important of these phenomena at igneous conditions is the temperature and compositional dependent long-range cation-ordering associated with the symmetry-breaking ($R\bar{3}c$ to $R\bar{3}$) phase transition. At elevated temperature, the idealized structure of these rhombohedral oxide solid solutions consists of hcp oxygen atoms with 2/3s of the intralayer octahedral interstices occupied by randomly distributed cations (Fe^{3+} , Fe^{2+} , Ti^{4+}). This configuration reflects the presence of two-fold axes of symmetry that are perpendicular to the c -axis of the unit cell and which relate the octahedral interstices on alternating layers. At low-temperatures, the Fe^{2+} and Ti^{4+} cations form an ordered arrangement over these layers, and this ordering destroys the two-fold axes of symmetry and lowers the configurational entropy of solution. This ordering is presumably driven by large positive enthalpic effects associated with intra-layer size-mismatch of Fe^{2+} and Ti^{4+} , an inference that is supported by the observation that the degree of order is enhanced at elevated pressure (Harrison and others, 2006). The symmetry breaking phase transition between the high-temperature ($R\bar{3}c$) and low-temperature ($R\bar{3}$) structure is an example of *convergent* cation-ordering. From an energetic perspective, spin-ordering associated with the paramagnetic to antiferrimagnetic magnetic phase transition has an even larger effect on the configurational entropy (Ghiorso, 1997). Together, the cation and magnetic ordering phenomena induce phase separation resulting in elemental partitioning between disordered and partial ordered structures. Consequently, there are extensive miscibility gaps in the series.

In addition to the long-range effects discussed above, short-range order (SRO) plays an important role in describing energetic relations along the hematite-ilmenite join. We will demonstrate below that incorporation of SRO in the thermodynamic treatment is essential for quantitative estimation of T and f_{O_2} . Fortunately, Harrison and Redfern (2001) have estimated the degree of SRO in Fe_2O_3 - FeTiO_3 solid solutions and this information can be utilized in order to develop an approach to correct for this effect empirically in the macroscopic thermodynamic formalism.

Formulation of a Thermodynamic Model

The composition variable X is taken to denote the mole fraction of FeTiO_3 in rhombohedral oxide solid solutions. Along the $\text{Fe}_2\text{O}_3\text{-FeTiO}_3$ join, the mole fraction of hematite is consequently given by $1-X$. Alternating layers of octahedral interstices in the structure are denoted “A” and “B.” Note that “A” and “B” octahedral interstices are symmetrically identical in the cation-disordered $R\bar{3}c$ structure and symmetrically distinct in the cation-ordered $R\bar{3}$ structure. Consequently, an ordering variable may be defined to quantify the extent of cation-ordering in the series by inventorying the relative proportion of Fe^{2+} or Ti^{4+} on each layer of octahedral sites. We prefer the definition:

$$s = X_{\text{Fe}^{2+}}^A - X_{\text{Fe}^{2+}}^B \quad (1)$$

where s is the ordering variable and X_i^j refers to the mole fraction of the i^{th} type cation on the j^{th} type octahedral site layer. In the absence of ordering, s is zero, which is always the case when the intermediate solid solutions have $R\bar{3}c$ structures. Alternately, the ordering state may be characterized by Q ($Q = sX$; Harrison and others, 2000a, 2000b; Harrison, 2006), which has the advantage of making ± 1 the range of the ordering variable, but the disadvantage of complicating our thermodynamic analysis, especially in the limit $X \rightarrow 0$.

Mass balance relations may be written:

$$X_{\text{Fe}^{3+}}^A + X_{\text{Fe}^{3+}}^B = 2(1 - X) \quad (2)$$

$$X_{\text{Fe}^{2+}}^A + X_{\text{Fe}^{2+}}^B = X \quad (3)$$

$$X_{\text{Ti}}^A + X_{\text{Ti}}^B = X \quad (4)$$

$$X_{\text{Fe}^{3+}}^A + X_{\text{Fe}^{2+}}^A + X_{\text{Ti}}^A = 1 \quad (5)$$

$$X_{\text{Fe}^{3+}}^B + X_{\text{Fe}^{2+}}^B + X_{\text{Ti}}^B = 1 \quad (6)$$

and, with equation (1), equations (2)-(6) may be solved to provide definitions of site mole fractions incorporating the assumption that there is no long-range ordering of Fe^{3+} over “A” and “B” layers:

$$X_{\text{Fe}^{3+}}^A = X_{\text{Fe}^{3+}}^B = 1 - X \quad (7)$$

$$X_{\text{Fe}^{2+}}^A = X_{\text{Ti}}^B = \frac{X + s}{2} \quad (8)$$

$$X_{\text{Fe}^{2+}}^B = X_{\text{Ti}}^A = \frac{X - s}{2} \quad (9)$$

This is the simplest approximation that can be made regarding the behavior of ferric iron in the solid solution (Ghiorso, 1990a; Harrison and others, 2000b; Harrison, 2006). The assumption is supported by the recent analysis of Burton and others (2005) and it is not in violation of any experimental observation.

The (long-range) configurational entropy of solution is then given by

$$\begin{aligned} \bar{S}^{\text{conf}} = -R &[X_{\text{Fe}^{3+}}^A \ln X_{\text{Fe}^{3+}}^A + X_{\text{Fe}^{3+}}^B \ln X_{\text{Fe}^{3+}}^B + X_{\text{Fe}^{2+}}^A \ln X_{\text{Fe}^{2+}}^A \\ &+ X_{\text{Fe}^{2+}}^B \ln X_{\text{Fe}^{2+}}^B + X_{\text{Ti}}^A \ln X_{\text{Ti}}^A + X_{\text{Ti}}^B \ln X_{\text{Ti}}^B] \end{aligned} \quad (10)$$

and, with the aid of equations (7)–(9), equation (10) may be written

$$\bar{S}^{conf} = -R \left[2(1-X) \ln(1-X) + (X+s) \ln \frac{X+s}{2} + (X-s) \ln \frac{X-s}{2} \right] \quad (11)$$

In the absence of SRO, the molar Gibbs free energy of solution is given by

$$\bar{G} = -T\bar{S}^{conf} + \bar{G}^* \quad (12)$$

where \bar{G}^* is termed the vibrational component.

Harrison and others (2000a) and Harrison and Redfern (2001) report time-of-flight neutron diffraction studies of ilmenite-hematite solid solutions over the composition range $0.6 < X < 1$ and at temperatures up to 1300°C . Harrison and others (2000b) demonstrate that the Gibbs free energy of ordering ($\bar{G} - \bar{G}|_{s=0} = -T(\bar{S}^{conf} - \bar{S}^{conf}|_{s=0}) + \bar{G}^* - \bar{G}^*|_{s=0}$) for each composition investigated can be modeled as a polynomial function of the ordering variable, Q ,

$$\bar{G} - \bar{G}|_{s=0} = \frac{aQ^2}{2} + \frac{bQ^n}{n} \quad (13)$$

where n is found to be ~ 4 and a and b vary as smooth functions of composition. This analysis suggests that a functional form for \bar{G}^* in equation (12) should involve terms that are at least fourth order in the ordering variable and that account for coupling of the ordering variable to composition. A generic Taylor expansion in X and s to fourth order generates 15 energy parameters

$$\begin{aligned} \bar{G}^* = & \bar{G}_0^* + \bar{G}_X^*X + \bar{G}_s^*s + \bar{G}_{XX}^*X^2 + \bar{G}_{Xs}^*Xs + \bar{G}_{ss}^*s^2 + \bar{G}_{XXX}^*X^3 + \bar{G}_{Xss}^*Xs^2 + \bar{G}_{XXs}^*X^2s \\ & + \bar{G}_{sss}^*s^3 + \bar{G}_{XXXX}^*X^4 + \bar{G}_{XXXs}^*X^3s + \bar{G}_{XXss}^*X^2s^2 + \bar{G}_{Xsss}^*Xs^3 + \bar{G}_{ssss}^*s^4 \end{aligned} \quad (14)$$

It is desirable to relate the Taylor expansion coefficients in equation (14) to more physically meaningful thermodynamic parameters, and it is especially important to discover if any of the Taylor expansion coefficients are correlated or are otherwise constrained by the existence of convergent cation-ordering in the system. One approach towards this aim is to construct an equivalent model expression for \bar{G}^* by considering a polynomial expansion of the vibrational Gibbs free energy in a composition-ordering space, with apices defined by the endmembers $[\text{Fe}^{3+}]^A[\text{Fe}^{3+}]^B\text{O}_3$, $[\text{Fe}^{2+}]^A[\text{Ti}^{4+}]^B\text{O}_3$, $[\text{Ti}^{4+}]^A[\text{Fe}^{2+}]^B\text{O}_3$. Such an expansion is given by

$$\begin{aligned} \bar{G}^* = & X_{Hm} \mu_{Hm}^o + X_{FeTi} \mu_{FeTi}^o + X_{TiFe} \mu_{TiFe}^o + X_{Hm}^3 X_{FeTi} W_{Hm-Hm-Hm-FeTi} \\ & + X_{Hm}^2 X_{FeTi}^2 W_{Hm-Hm-FeTi-FeTi} + X_{Hm} X_{FeTi}^3 W_{Hm-FeTi-FeTi-FeTi} + X_{Hm}^3 X_{TiFe} W_{Hm-Hm-Hm-TiFe} \\ & + X_{Hm}^2 X_{TiFe}^2 W_{Hm-Hm-TiFe-TiFe} + X_{Hm} X_{TiFe}^3 W_{Hm-TiFe-TiFe-TiFe} + X_{FeTi}^3 X_{TiFe} W_{FeTi-FeTi-FeTi-TiFe} \\ & + X_{FeTi}^2 X_{TiFe}^2 W_{FeTi-FeTi-TiFe-TiFe} + X_{FeTi} X_{TiFe}^3 W_{FeTi-TiFe-TiFe-TiFe} \\ & + X_{Hm}^2 X_{FeTi} X_{TiFe} W_{Hm-Hm-FeTi-TiFe} + X_{Hm} X_{FeTi}^2 X_{TiFe} W_{Hm-FeTi-FeTi-TiFe} \\ & + X_{Hm} X_{FeTi} X_{TiFe}^2 W_{Hm-FeTi-TiFe-TiFe} \end{aligned} \quad (15)$$

where X_{Hm} , X_{FeTi} , and X_{TiFe} denote the mole fractions of $[\text{Fe}^{3+}]^A[\text{Fe}^{3+}]^B\text{O}_3$, $[\text{Fe}^{2+}]^A[\text{Ti}^{4+}]^B\text{O}_3$, and $[\text{Ti}^{4+}]^A[\text{Fe}^{2+}]^B\text{O}_3$, respectively. The interaction parameters in

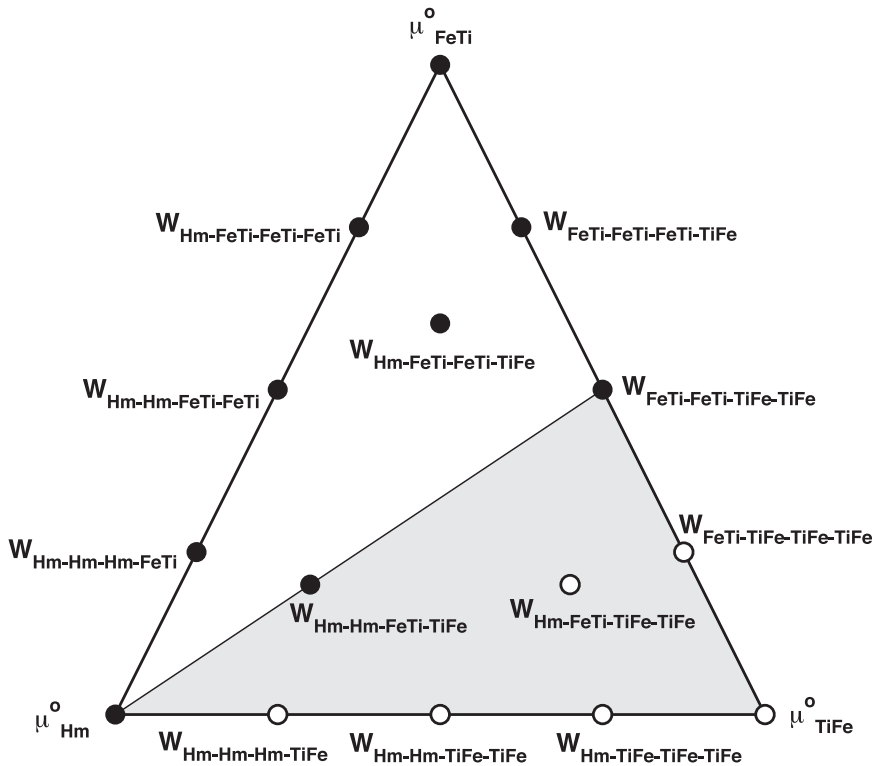


Fig. 1. Provisional model parameters for a 4th order Taylor expansion of the molar vibrational Gibbs free energy of solution are displayed in composition-ordering space for the binary system $\text{Fe}_2\text{O}_3\text{-FeTiO}_3$. **Hm** refers to Fe_2O_3 , **FeTi** to cation-ordered FeTiO_3 with titanium occupancy of the “B” octahedral layers, and **TiFe** to cation-ordered FeTiO_3 with Ti^{4+} occupying the “A” layer. Parameter symbols are plotted at the location of greatest influence on the shape of the Gibbs surface, that is the position where the mole fraction product that multiplies the parameter in equation (15) has a maximal value. Note that the Gibbs energy of the system is mirrored by the pseudobinary section that passes through the **Hm** apex with $\text{FeTi}/\text{TiFe} = 1$. Parameters plotted as *open circles* must consequently have values identical to their *closed circle* equivalents related by this energetic plane of symmetry.

equation (15) can be understood by examining figure 1. The free energy surface is warped from the standard state¹ plane ($X_{\text{Hm}} \mu_{\text{Hm}}^{\circ} + X_{\text{FeTi}} \mu_{\text{FeTi}}^{\circ} + X_{\text{TiFe}} \mu_{\text{TiFe}}^{\circ}$) that passes through the apices of the ternary by an excess free energy function that may be fixed at the topological locations of the labeled parameters. What is apparent from the figure is that a mirror plane of symmetry must exist in the free energy surface that relates the shaded and unshaded portions of the triangle. This is so because the A, B designation of octahedral layers in the structure is arbitrary, and consequently a relabeling of the layers (that is $[\text{Fe}^{2+}]^{\text{A}}[\text{Ti}^{4+}]^{\text{B}}\text{O}_3 \rightarrow [\text{Ti}^{4+}]^{\text{A}}[\text{Fe}^{2+}]^{\text{B}}\text{O}_3$) cannot alter the energy of the system. It follows that the labeled parameters denoted by the solid and open symbols must be related by this mirror plane, that is $\mu_{\text{FeTi}}^{\circ} = \mu_{\text{TiFe}}^{\circ}$, $W_{\text{FeTi}^3 - \text{TiFe}} = W_{\text{FeTi} - \text{TiFe}^3}$, *et cetera*.

Before reducing equation (15) to take advantage of the symmetry of the Gibbs surface, it is advantageous to recast the quartic parameterization into an equivalent

¹ The standard state is taken to be unit activity of the pure substance in an equilibrium state of structural order at any temperature and pressure.

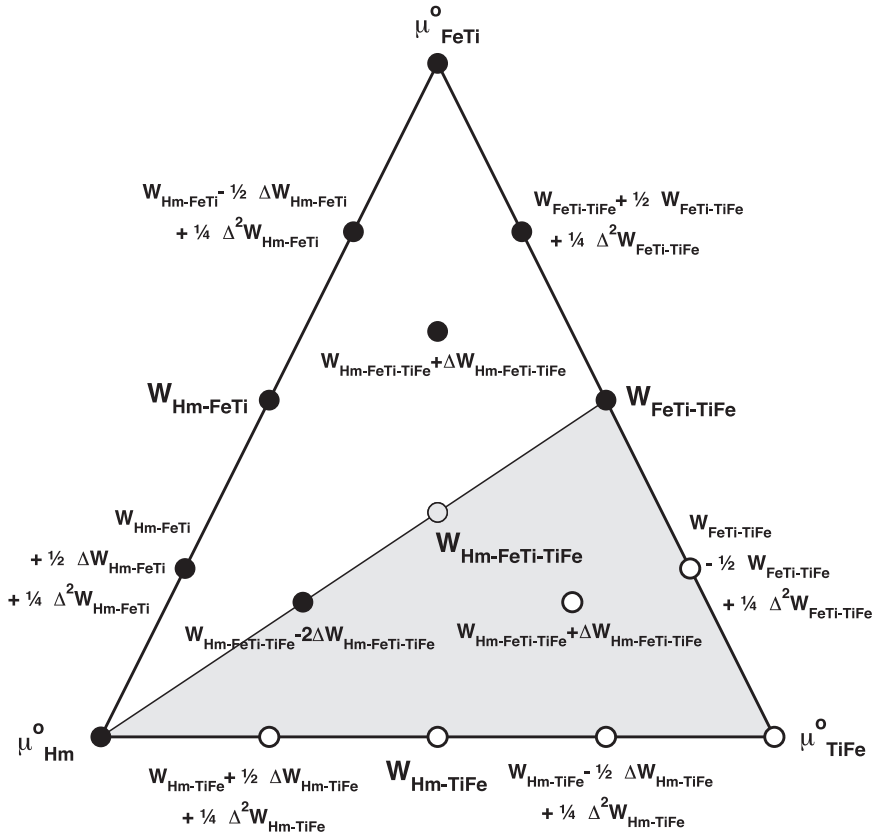


Fig. 2. Preferred model parameters for a 4th order Taylor expansion of the molar vibrational Gibbs free energy of solution are displayed in composition-ordering space for the binary system $\text{Fe}_2\text{O}_3\text{-FeTiO}_3$. See legend for figure 1. Plotted locations are identical to those in figure 1 with the exception of the ternary mid-point parameter, $\mathbf{W}_{\text{Hm-FeTi-TiFe}}$, which is the average of the other three 4th order ternary parameters. The mapping of parameters from figure 1 to this figure is reflected in the transformation of equation (15) to equation (16).

and hopefully more recognizable form. Following a set of parameter transformations developed in the Appendix [eqs (95), (97), (101), (102), (105), (106), (107), and (108)], equation (15) can be reduced to

$$\begin{aligned} \bar{G}^* = & X_{\text{Hm}} \mu_{\text{Hm}}^o + X_{\text{FeTi}} \mu_{\text{FeTi}}^o + X_{\text{TiFe}} \mu_{\text{TiFe}}^o + X_{\text{Hm}} X_{\text{FeTi}} [W_{\text{Hm-FeTi}} + \Delta W_{\text{Hm-FeTi}} (X_{\text{Hm}} - X_{\text{FeTi}}) \\ & + \Delta^2 W_{\text{Hm-FeTi}} (X_{\text{Hm}} - X_{\text{FeTi}})^2] + X_{\text{Hm}} X_{\text{TiFe}} [W_{\text{Hm-TiFe}} + \Delta W_{\text{Hm-TiFe}} (X_{\text{Hm}} - X_{\text{TiFe}}) \\ & + \Delta^2 W_{\text{Hm-TiFe}} (X_{\text{Hm}} - X_{\text{TiFe}})^2] + X_{\text{FeTi}} X_{\text{TiFe}} [W_{\text{FeTi-TiFe}} + \Delta W_{\text{FeTi-TiFe}} (X_{\text{FeTi}} - X_{\text{TiFe}}) \\ & + \Delta^2 W_{\text{FeTi-TiFe}} (X_{\text{FeTi}} - X_{\text{TiFe}})^2] + X_{\text{Hm}} X_{\text{FeTi}} X_{\text{TiFe}} W_{\text{Hm-FeTi-TiFe}} \\ & + X_{\text{Hm}} X_{\text{FeTi}} X_{\text{TiFe}} \Delta W_{\text{Hm-FeTi-TiFe}} \times (X_{\text{FeTi}} - X_{\text{Hm}}) \\ & + X_{\text{Hm}} X_{\text{FeTi}} X_{\text{TiFe}} \Delta W_{\text{Hm-FeTi-TiFe}}^2 (X_{\text{TiFe}} - X_{\text{Hm}}) \end{aligned} \quad (16)$$

Figure 2 demonstrates the mapping between the parameter set of equation (16) and that of equation (15). $W_{\text{Hm-FeTi}}$, $W_{\text{Hm-TiFe}}$, and $W_{\text{FeTi-TiFe}}$ are binary or regular solution-type interaction terms. The $\Delta W_{\text{Hm-FeTi}}$ and $\Delta^2 W_{\text{Hm-FeTi}}$ type terms embody

successively higher-order perturbations from a regular solution. Within the interior of the ternary, the quartic terms of (15) are recast in terms of deviations from a strictly ternary interaction parameter. The parameterization of equation (16) makes apparent which terms are binary, which are ternary, and which contribute to fourth order perturbations to the vibrational Gibbs free energy surface.

In terms of X and s , the endmember mole fractions X_{Hm} , X_{FeTi} , and X_{TiFe} have the following definitions:

$$X_{Hm} = X_{Fe^{3+}}^A = X_{Fe^{3+}}^B = 1 - X \quad (17)$$

$$X_{FeTi} = X_{Fe^{2+}}^A = X_{Ti}^B = \frac{X + s}{2} \quad (18)$$

$$X_{TiFe} = X_{Fe^{2+}}^B = X_{Ti}^A = \frac{X - s}{2} \quad (19)$$

Substitution of equations (17)–(19) into equation (16) yields

$$\begin{aligned} \bar{G}^* = & (1 - X)\mu_{Hm}^o + \frac{X + s}{2}\mu_{FeTi}^o + \frac{X - s}{2}\mu_{TiFe}^o + (1 - X)\frac{X + s}{2}W_{Hm-FeTi} + (1 \\ & - X)\frac{X + s}{2}\left[(1 - X) - \frac{X + s}{2}\right]\Delta W_{Hm-FeTi} + (1 - X)\frac{X + s}{2}\left[(1 - X) \right. \\ & \left. - \frac{X + s}{2}\right]^2\Delta^2 W_{Hm-FeTi} + (1 - X)\frac{X - s}{2}W_{Hm-TiFe} + (1 - X)\frac{X - s}{2}\left[(1 - X) \right. \\ & \left. - \frac{X - s}{2}\right]\Delta W_{Hm-TiFe} + (1 - X)\frac{X - s}{2}\left[(1 - X) - \frac{X - s}{2}\right]^2\Delta^2 W_{Hm-TiFe} \\ & + \frac{X + s}{2}\frac{X - s}{2}W_{FeTi-TiFe} + \frac{X + s}{2}\frac{X - s}{2}\left(\frac{X + s}{2} - \frac{X - s}{2}\right)\Delta W_{FeTi-TiFe} \\ & + \frac{X + s}{2}\frac{X - s}{2}\left(\frac{X + s}{2} - \frac{X - s}{2}\right)^2\Delta^2 W_{FeTi-TiFe} + (1 - X)\frac{X + s}{2}\frac{X - s}{2}W_{Hm-FeTi^2-TiFe} \\ & + (1 - X)\frac{X + s}{2}\frac{X - s}{2}\left[\frac{X + s}{2} - (1 - X)\right]\Delta W_{Hm-FeTi^2-TiFe} \\ & + (1 - X)\frac{X + s}{2}\frac{X - s}{2}\left[\frac{X - s}{2} - (1 - X)\right]\Delta W_{Hm-FeTi-TiFe^2} \end{aligned} \quad (20)$$

Energetic symmetry demands that

$$\mu_{FeTi}^o = \mu_{TiFe}^o \equiv \mu_R^o \quad (21)$$

$$W_{Hm-FeTi} = W_{Hm-TiFe} \equiv W_{Hm-II} \quad (22)$$

$$\Delta W_{Hm-FeTi} = \Delta W_{Hm-TiFe} \equiv \Delta W_{Hm-II} \quad (23)$$

$$\Delta^2 W_{Hm-FeTi} = \Delta^2 W_{Hm-TiFe} \equiv \Delta^2 W_{Hm-II} \quad (24)$$

$$\Delta W_{FeTi-TiFe} = 0 \quad (25)$$

$$\Delta W_{Hm-FeTi^2-TiFe} = \Delta W_{Hm-FeTi-TiFe^2} \equiv \Delta W_{Hm-II^3} \quad (26)$$

and permits the simplifying definitions

$$W_{FeTi-TiFe} = W_{II-II} \quad (27)$$

$$\Delta^2 W_{FeTi-TiFe} = \Delta^2 W_{II-II} \quad (28)$$

Substituting equations (21)–(28) into equation (20) along with some algebraic simplification results in:

$$\begin{aligned} \bar{G}^* = & (1-X)\mu_{Hm}^o + X\mu_{II}^o + (1-X)X[W_{Hm-II} + (1-X-X)\Delta W_{Hm-II}] \\ & + (1-X-X)^2\Delta^2 W_{Hm-II}] + (X^2 - s^2) \left[\frac{W_{II-II}}{4} + (1-X) \left(\frac{\Delta W_{Hm-II}}{2} + \frac{W_{Hm-II-II}}{4} \right) \right] \\ & + 3(1-X)X[4(1-X)X - (X^2 - s^2)] \frac{\Delta^2 W_{Hm-II}}{4} - (X^2 - s^2)(1-X)[2(1-X) \\ & - X] \frac{\Delta W_{Hm-II^3}}{4} + (X^2 - s^2)s^2 \frac{\Delta^2 W_{II-II}}{4} \end{aligned} \quad (29)$$

Equation (29) may be rearranged into a Taylor expansion form [that is eq (14)],

$$\begin{aligned} \bar{G}^* = & \mu_{Hm}^o + (\mu_{II}^o - \mu_{Hm}^o + W_{Hm-II} + \Delta W_{Hm-II} + \Delta^2 W_{Hm-II})X + \left(\frac{W_{II-II}}{4} + \frac{W_{Hm-II-II}}{4} - W_{Hm-II} \right. \\ & \left. - \frac{5}{2}\Delta W_{Hm-II} - 2\Delta^2 W_{Hm-II} - \frac{\Delta W_{Hm-II^3}}{2} \right) X^2 + \left(-\frac{W_{II-II}}{4} - \frac{\Delta W_{Hm-II}}{2} - \frac{W_{Hm-II-II}}{4} \right. \\ & \left. + \frac{\Delta W_{Hm-II^3}}{2} \right) s^2 + \left(\frac{3}{2}\Delta W_{Hm-II} + \frac{5}{4}\Delta^2 W_{Hm-II} - \frac{W_{Hm-II-II}}{4} + \frac{5}{4}\Delta W_{Hm-II^3} \right) X^3 \\ & + \left(\frac{3}{4}\Delta^2 W_{Hm-II} + \frac{\Delta W_{Hm-II}}{2} + \frac{W_{Hm-II-II}}{4} - \frac{5}{4}\Delta W_{Hm-II^3} \right) Xs^2 + \left(-\frac{\Delta^2 W_{Hm-II}}{4} \right. \\ & \left. - \frac{3}{4}\Delta W_{Hm-II^3} \right) X^4 + \left(\frac{\Delta^2 W_{II-II}}{4} - \frac{3}{4}\Delta^2 W_{Hm-II} + \frac{3}{4}\Delta W_{Hm-II^3} \right) X^2 s^2 - \frac{\Delta^2 W_{II-II}}{4}s^4 \end{aligned} \quad (30)$$

from which it is clear that the energetic symmetry constraint forces all terms involving odd powers of the ordering variable to vanish.

Combining equations (30), (11) and (12) gives a model equation for the molar Gibbs free energy of solution:

$$\begin{aligned} \bar{G} = & RT \left[2(1-X) \ln(1-X) + (X+s) \ln \frac{X+s}{2} + (X-s) \ln \frac{X-s}{2} \right] + \bar{G}_0^* + \bar{G}_X^* X \\ & + \bar{G}_{XX}^* X^2 + \bar{G}_{ss}^* s^2 + \bar{G}_{XXX}^* X^3 + \bar{G}_{Xss}^* Xs^2 + \bar{G}_{XXXs}^* X^4 + \bar{G}_{XXss}^* X^2 s^2 + \bar{G}_{sss}^* s^4 \end{aligned} \quad (31)$$

For reference, definitions of the Taylor expansion coefficients in terms of preferred model parameters are provided in table 1.

Calibration of the Model—Cation-Ordering

The molar Gibbs free energy of solution is minimal in an equilibrium state of cation-order. Therefore, from (31), this state may be modeled with the expression

$$\frac{\partial \bar{G}}{\partial s} = 0 = RT \ln \frac{X+s}{X-s} + 2(\bar{G}_{ss}^* + 2\bar{G}_{Xss}^* X + 2\bar{G}_{XXss}^* X^2)s + 4\bar{G}_{sss}^* s^3 \quad (32)$$

TABLE 1
Taylor expansion coefficients

Coefficient	Definition
\bar{G}_0^*	μ_{Hm}^o
\bar{G}_X^*	$\mu_{Hm}^o - \mu_{Hm}^o + W_{Hm-II} + \Delta W_{Hm-II} + \Delta^2 W_{Hm-II}$
\bar{G}_{XX}^*	$\frac{W_{II-II}}{4} + \frac{W_{Hm-II-II}}{4} - W_{Hm-II} - \frac{5}{2} \Delta W_{Hm-II} - 2 \Delta^2 W_{Hm-II} - \frac{\Delta W_{Hm-II^3}}{2}$
\bar{G}_{ss}^*	$-\frac{W_{II-II}}{4} - \frac{\Delta W_{Hm-II}}{2} - \frac{W_{Hm-II-II}}{4} + \frac{\Delta W_{Hm-II^3}}{2}$
\bar{G}_{XXX}^*	$\frac{3}{2} \Delta W_{Hm-II} + \frac{5}{4} \Delta^2 W_{Hm-II} - \frac{W_{Hm-II-II}}{4} + \frac{5}{4} \Delta W_{Hm-II^3}$
\bar{G}_{Xss}^*	$\frac{3}{4} \Delta^2 W_{Hm-II} + \frac{\Delta W_{Hm-II}}{2} + \frac{W_{Hm-II-II}}{4} - \frac{5}{4} \Delta W_{Hm-II^3}$
\bar{G}_{XXXX}^*	$-\frac{\Delta^2 W_{Hm-II}}{4} - \frac{3}{4} \Delta W_{Hm-II^3}$
\bar{G}_{XXss}^*	$\frac{\Delta^2 W_{II-II}}{4} - \frac{3}{4} \Delta^2 W_{Hm-II} + \frac{3}{4} \Delta W_{Hm-II^3}$
\bar{G}_{ssss}^*	$-\frac{\Delta^2 W_{II-II}}{4}$

and measurements of the degree of order made as a function of composition and temperature may be utilized to calibrate values for four of the Taylor expansion coefficients. In figure 3 the time-of-flight neutron diffraction measurements of LRO by Harrison and others (2000a) and Harrison and Redfern (2001) are plotted. At lower ilmenite contents ($X = 0.7, 0.65$, and 0.6) there is a hysteresis effect evident in measurements of the ordering state that reflect different values obtained along heating and cooling paths of the experiments. Given that samples were prepared by synthesis at 1300°C (Harrison and others, 2000a), which corresponds to a randomly ordered condition for these bulk compositions, we interpret this hysteresis as a kinetic phenomenon associated with the inability to achieve an equilibrium state of order in the time frame of the experiment (5 minutes of pre-heating and 50 minutes of data collection at each temperature, *loco citato*). Alternatively, it should be noted that the three compositions that show the most notable hysteresis do so in the subsolidus region of the phase diagram (Ghiorso, 1990a; see below). At the measurement temperature these samples may contain microdomains of phases with distinct compositions and ordering states (Harrison and others, 2000b), and Harrison (2006) demonstrates using Monte Carlo simulation techniques that fine-scale chemical segregation can generate the observed Q vs T ordering profile for $X = 0.7$.

In order to avoid the hysteresis effect and minimize any systematic offset that might potentially arise from the sluggish kinetics of ordering or chemical segregation, only data collected at temperatures in excess of $\sim 700^\circ\text{C}$ are utilized in the calibration of equation (32). It is found that an optimal fit can be achieved with only three parameters, namely \bar{G}_{ss}^* , \bar{G}_{Xss}^* , and \bar{G}_{ssss}^* ; the data cannot be used to assign statistically a unique value for \bar{G}_{XXss}^* . This result can be interpreted to imply that fourth order

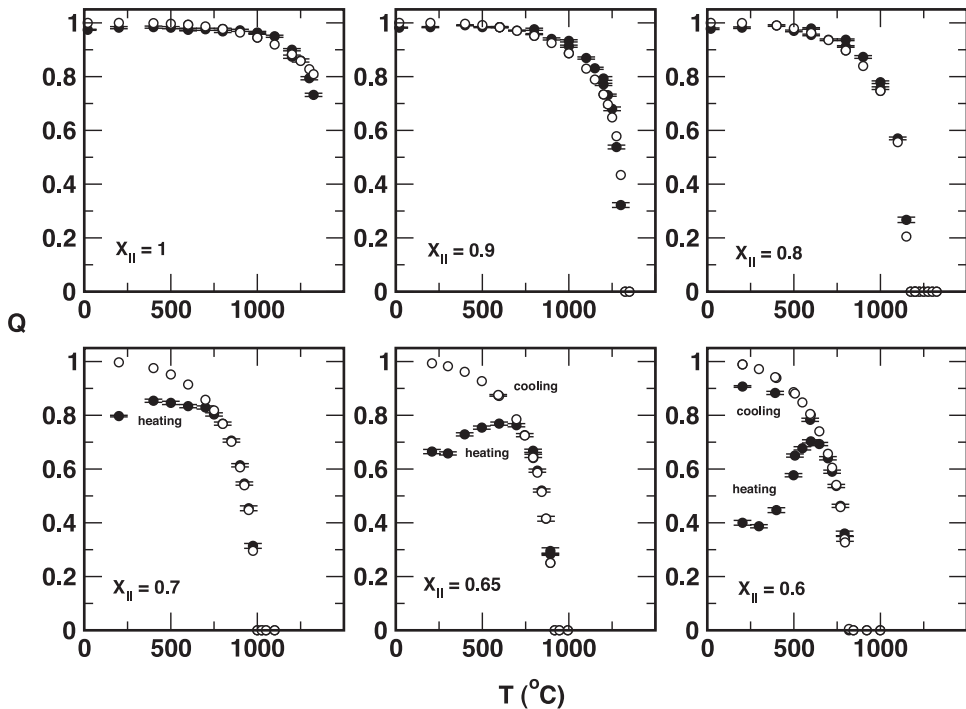


Fig. 3. Cation-ordering data from Harrison and others (2000a) and Harrison and Redfern (2001) are plotted. Ordinate is the normalized ordering parameter Q , defined as s/X . Panels are labeled for bulk composition. Closed circles are experimental data points, open circles are model calculations. Uncertainties on data points are indicated. Note the heating/cooling hysteresis effect for bulk compositions at X of 0.7, 0.65, and 0.6.

parameters like $\Delta^2 W_{Hm-II}$ and ΔW_{Hm-II^3} have a negligible effect on the free energy of solution. Setting these parameters to zero implies that \bar{G}_{XXss}^* equals $-\bar{G}_{ssss}^*$ (see table 1), and under this constraint an optimization of the ordering data generates the fit shown in figure 3 and the calibration:

$$\bar{G}_{ss}^* = -\frac{W_{II-II}}{4} - \frac{\Delta W_{Hm-II}}{2} - \frac{W_{Hm-II-II}}{4} = -14.455 \text{ kJ/mol} \quad (33)$$

$$\bar{G}_{XXss}^* = \frac{\Delta W_{Hm-II}}{2} + \frac{W_{Hm-II-II}}{4} = -3.022 \text{ kJ/mol} \quad (34)$$

$$\bar{G}_{ssss}^* = -\bar{G}_{XXss}^* = -\frac{\Delta^2 W_{II-II}}{4} = -3.189 \text{ kJ/mol} \quad (35)$$

The locus of T - X points that corresponds to the *critical ordering curve* (T_C) defines the onset of cation-ordering and the location of the symmetry breaking phase transition. It may be calculated from the limit (Prigogine and Defay, 1954)

$$\lim_{s \rightarrow 0} \frac{\partial^2 \bar{G}}{\partial s^2} = 0 \quad (36)$$

where from equation (32)

$$\frac{\partial^2 \bar{G}}{\partial s^2} = \frac{2RTX}{X^2 - s^2} + 2(\bar{G}_{ss}^* + 2\bar{G}_{Xss}^*X + 2\bar{G}_{XXss}^*X^2) + 12\bar{G}_{ssss}^*s^2 \quad (37)$$

and substitution yields

$$T_C = -\frac{X}{R}(\bar{G}_{ss}^* + 2\bar{G}_{Xss}^*X + 2\bar{G}_{XXss}^*X^2) \quad (38)$$

The critical ordering curve consistent with our analysis of the ordering data is plotted in figure 4. At temperatures above the curve, solid solutions have space group symmetry $R\bar{3}c$; below the curve compositions have the structure $R\bar{3}$.

The dashed curve in figure 4 is a locus of inflection points on the Gibbs free energy surface. These points satisfy the equality

$$\lim_{s \rightarrow 0} \frac{\partial^3 \bar{G}}{\partial s^3} = 0 \quad (39)$$

where from equation (37)

$$\frac{\partial^3 \bar{G}}{\partial s^3} = \frac{4RTXs}{(X^2 - s^2)^2} + 24\bar{G}_{ssss}^*s \quad (40)$$

The dashed curve in figure 4 intersects the critical ordering curve at X_C , the composition at which the thermodynamic character of the symmetry breaking phase transition changes from 2nd order to 1st order; X_C is a *critical point* in ordering space. This change in order can be illustrated using the Gibbs free energy diagrams plotted in figure 5. For temperatures along T_C and $X < X_C$ (fig. 5A, where $X = 0.75$), the Gibbs free energy surface is concave up with respect to variation in the order parameter and the minimum in this surface (located at $s = 0$) is coincident with the minimum of $\frac{\partial^2 \bar{G}}{\partial s^2}$ and a zero of $\frac{\partial^3 \bar{G}}{\partial s^3}$. At X_C and T_C the simple zero in $\frac{\partial^3 \bar{G}}{\partial s^3}$ transforms into a point of inflection (fig. 5B, where $X_C = 0.8754$). At $X > X_C$ along T_C (fig. 5C, where $X = 1$) the Gibbs free energy surface exhibits a maximum and $\frac{\partial \bar{G}}{\partial s}$ passes through a point of inflection. Note from figure 5C that the temperature defined by T_C has no special significance when $X > X_C$. The stable phase, which in this illustrative case is chosen to be pure ilmenite, has a cation-ordering state defined by the minima in \bar{G} that happen to be located at $s = \pm 0.6316$. As temperature is raised for this bulk composition, the minima are elevated relative to the maxima at zero, until some temperature is reached where the three points are coincident (fig. 5D). This is the temperature of the first order phase transition. Two phases coexist at this temperature. One is ordered ($s = \pm 0.5538$) with symmetry $R\bar{3}$ and the other is disordered with symmetry $R\bar{3}c$. For the special case illustrated (namely $X = 1$, or pure ilmenite), both coexisting phases have the same bulk composition! At temperatures above the 1st order transition temperature (fig. 5E) a single disordered phase is stable as evidenced by the single minimum in

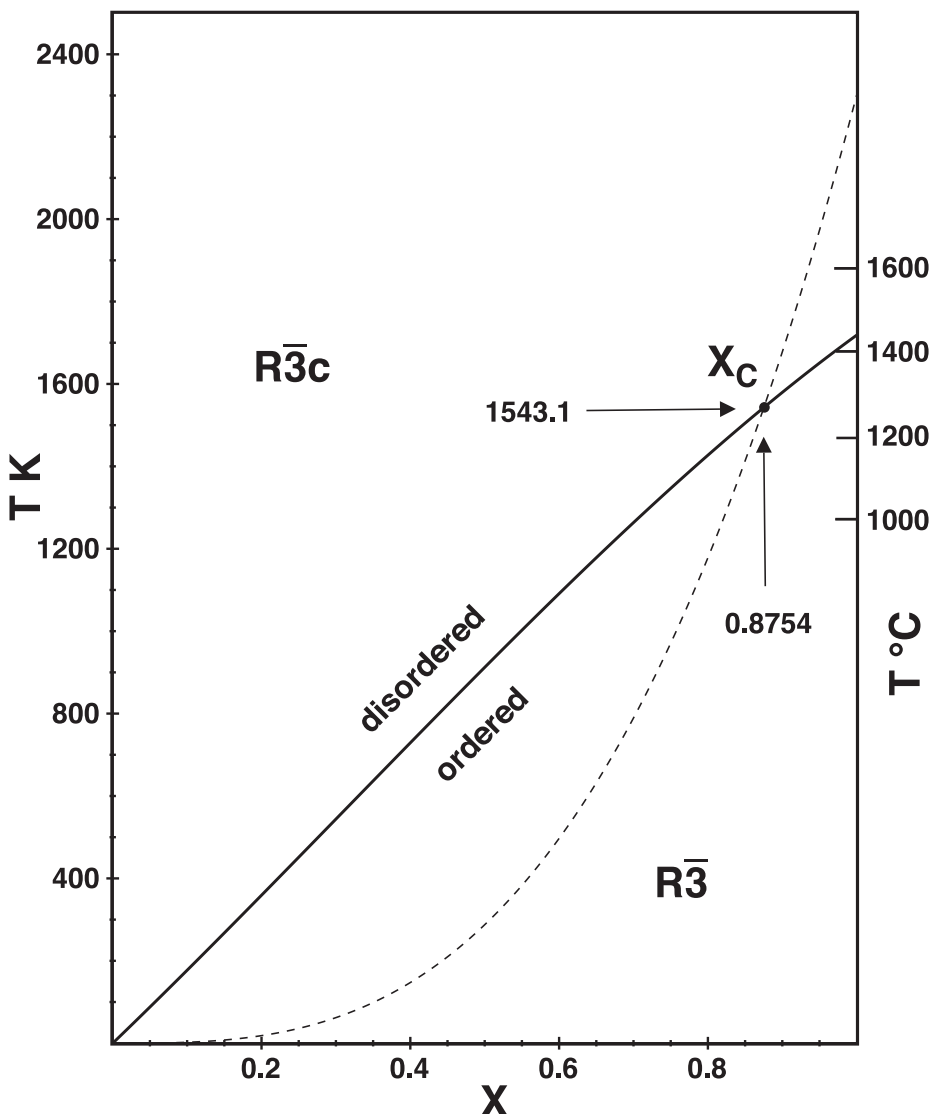


Fig. 4. T - X path of the critical ordering curve $\left(\lim_{s \rightarrow 0} \frac{\partial^2 \bar{G}}{\partial s^2} = 0\right)$. The curve delineates low- (cation *ordered*) and high- (cation *disordered*) symmetry structural states. The dashed curve is the solution to $\lim_{s \rightarrow 0} \frac{\partial^3 \bar{G}}{\partial s^3} = 0$, which intersects the critical ordering curve at the indicated composition, denoted in the text as X_C . To the left of X_C the phase transition is second-order. To the right of X_C it is first-order.

\bar{G} at $s = 0$. In summary, for $X < X_C$ as temperature is raised the ordering variable changes continuously, becoming zero at T_C and is zero everywhere above T_C . The transition is 2nd order because structural changes are continuous across the transition temperature. By contrast, for $X > X_C$, the structure changes abruptly at some $T > T_C$

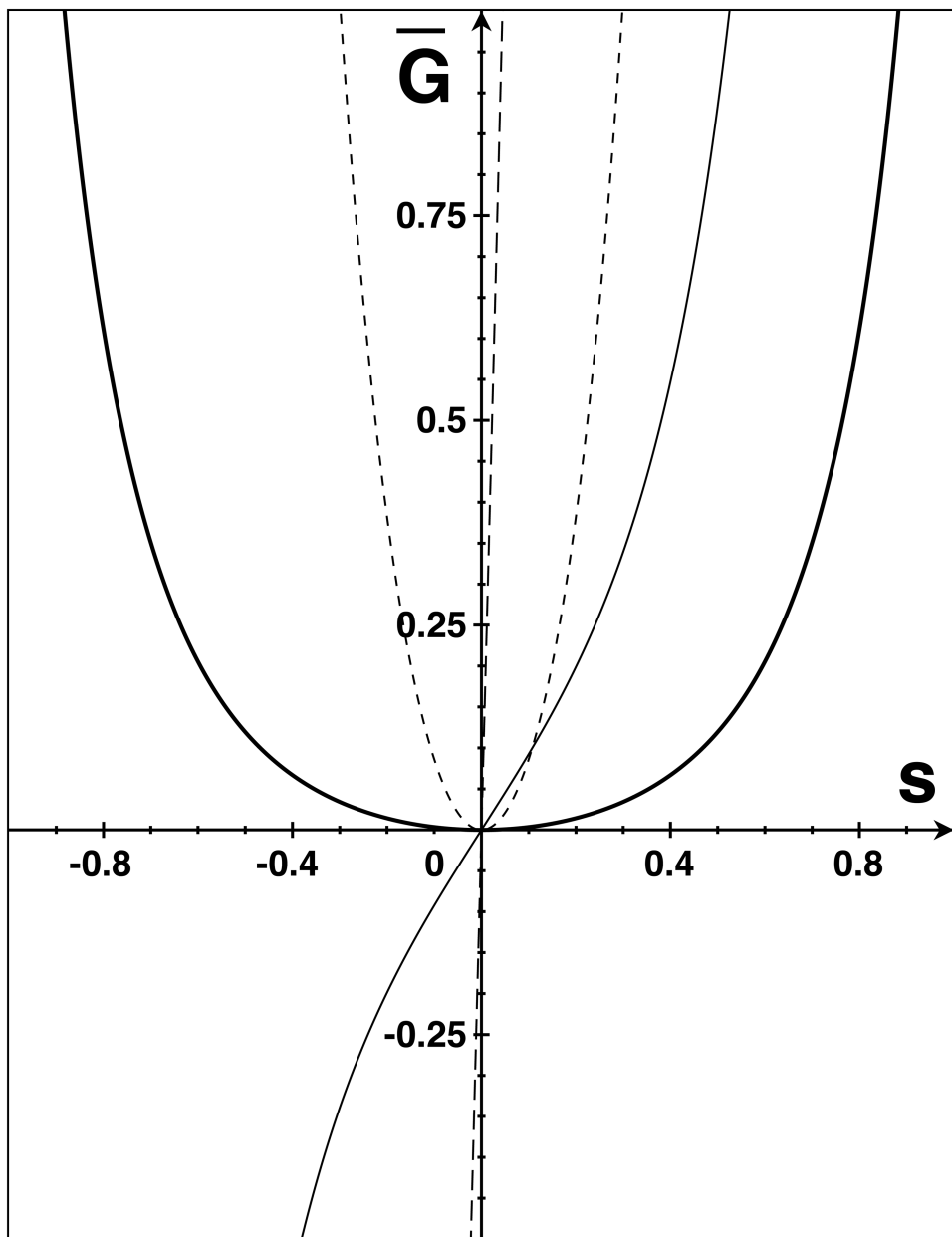


Fig. 5. Plots of the molar Gibbs free energy of solution (heavy solid curve)—adjusted to zero intercept—displayed along with its 1st (light solid curve), 2nd (dashed line), and 3rd (long-dashed line) derivatives with respect to ordering variable, s . (A) Temperature at T_C for $X = 0.75$ (on the critical ordering curve, to the left of X_C and at the second-order phase transition).

and the character of the transition is 1st order. A 1st order phase transition at $X = 1$ requires a two-phase loop to extend into the binary relating a more ilmenite-poor disordered phase to a more ilmenite-rich ordered phase. This two-phase loop must

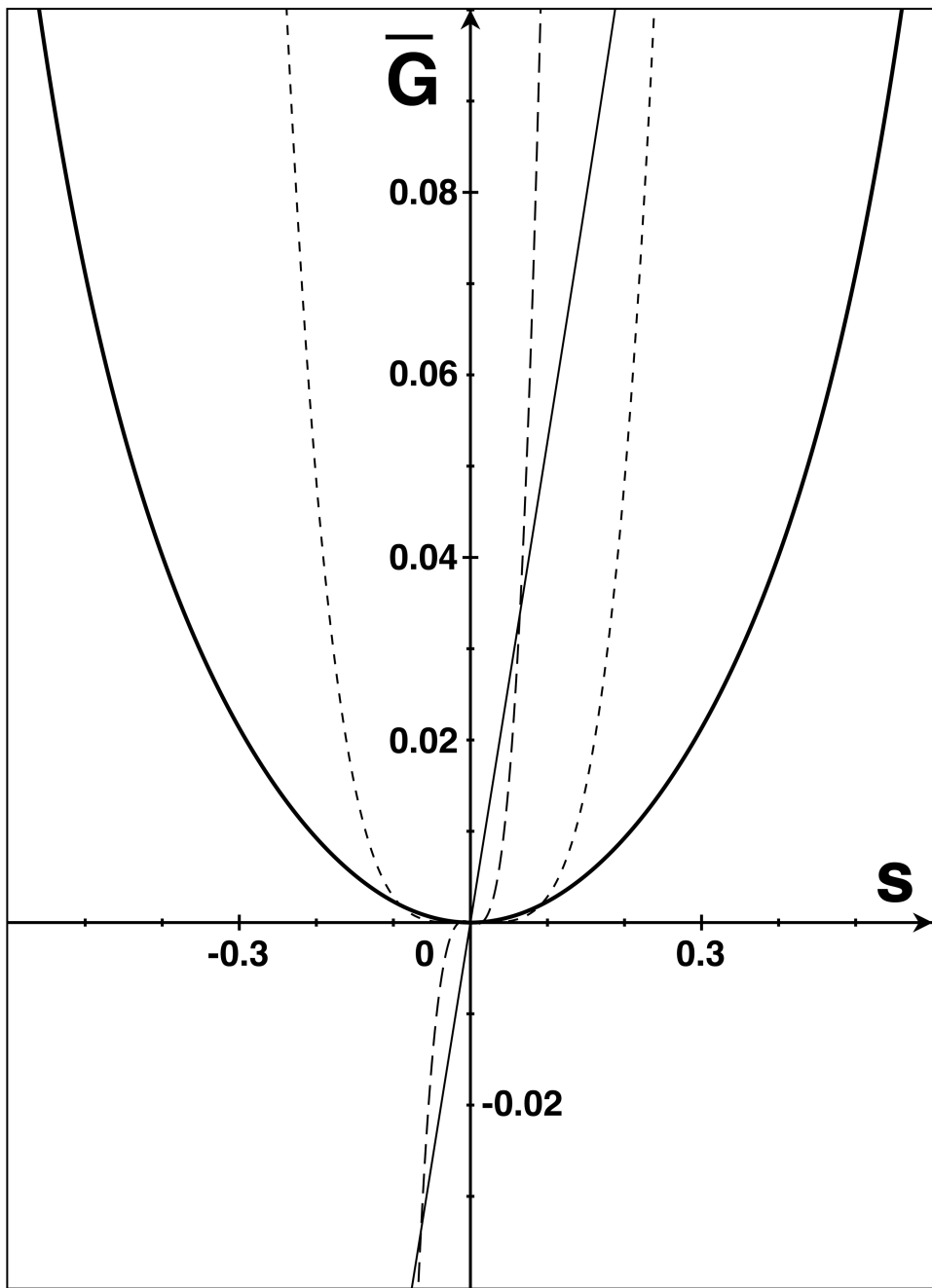


Fig. 5 (continued). (B) Temperature at T_C for $X = X_{C_0}$ (on the critical ordering curve, at the point where the order of the phase transition changes from 1st to 2nd).

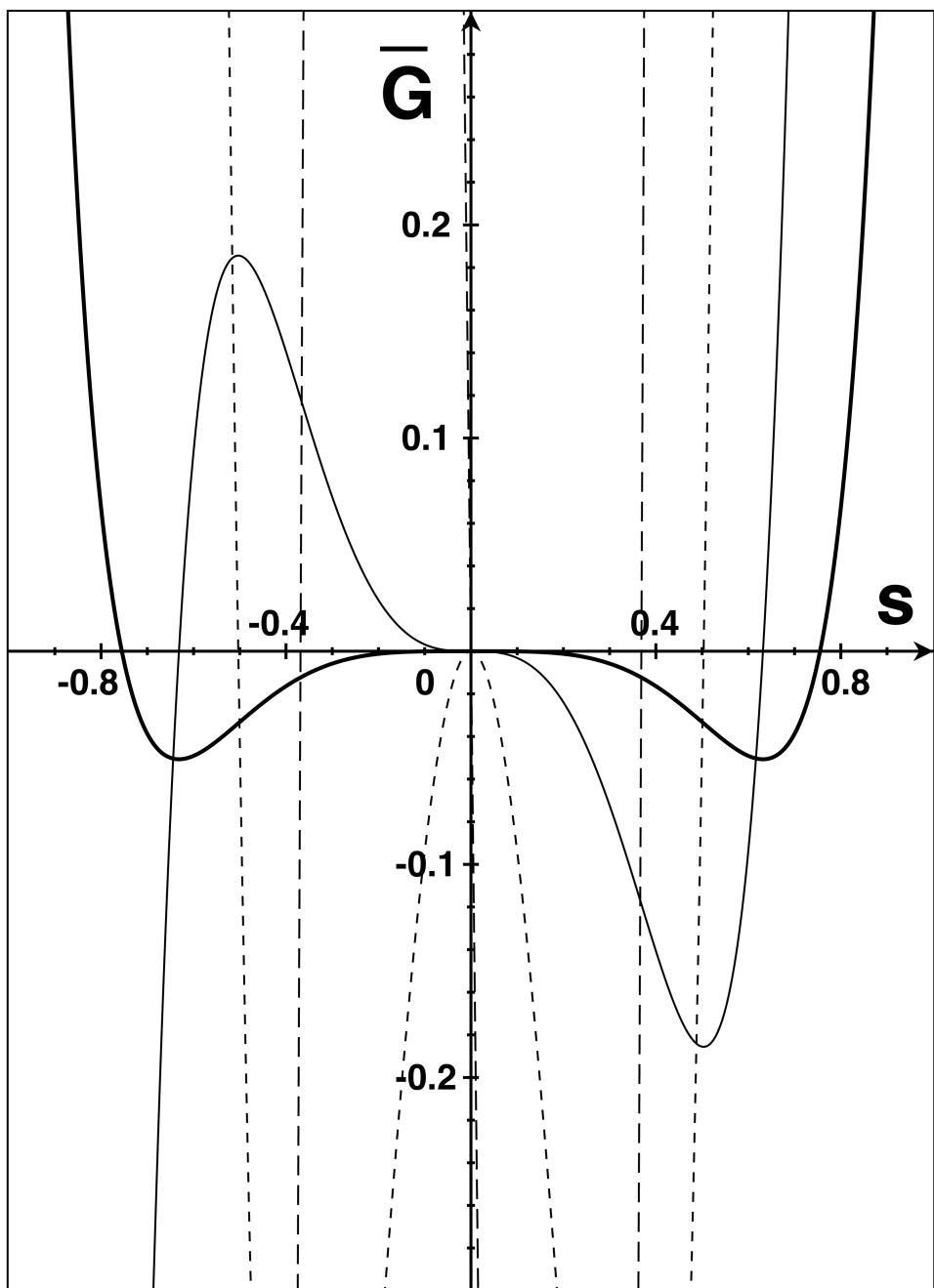


Fig. 5 (continued). (C) Temperature at T_C for $X = 1$ (pure ilmenite; on the critical ordering curve, but here the disordered state, $s = 0$, is metastable with respect to unmixing to ordered states defined by the minima in \bar{G} located at $s = \pm 0.6316$).

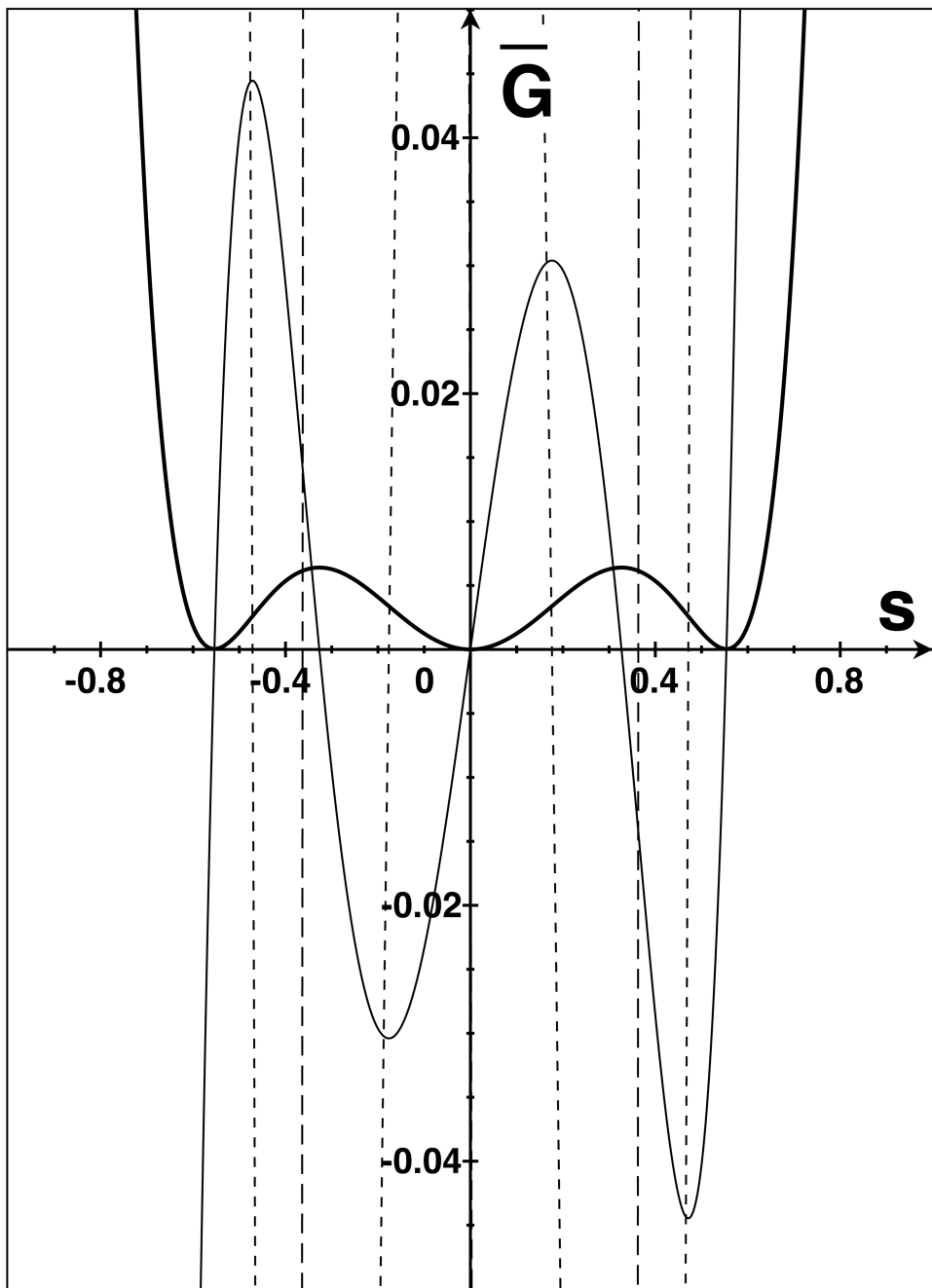


Fig. 5 (continued). (D) Temperature at $T_c + 15.9^\circ\text{C}$ for $X = 1$ (pure ilmenite). This is the temperature of the first order phase transition between disordered FeTiO_3 ($s = 0$) and ordered FeTiO_3 ($s = \pm 0.5538$). All ordering states (stable phases) have the same \bar{G} at equilibrium.

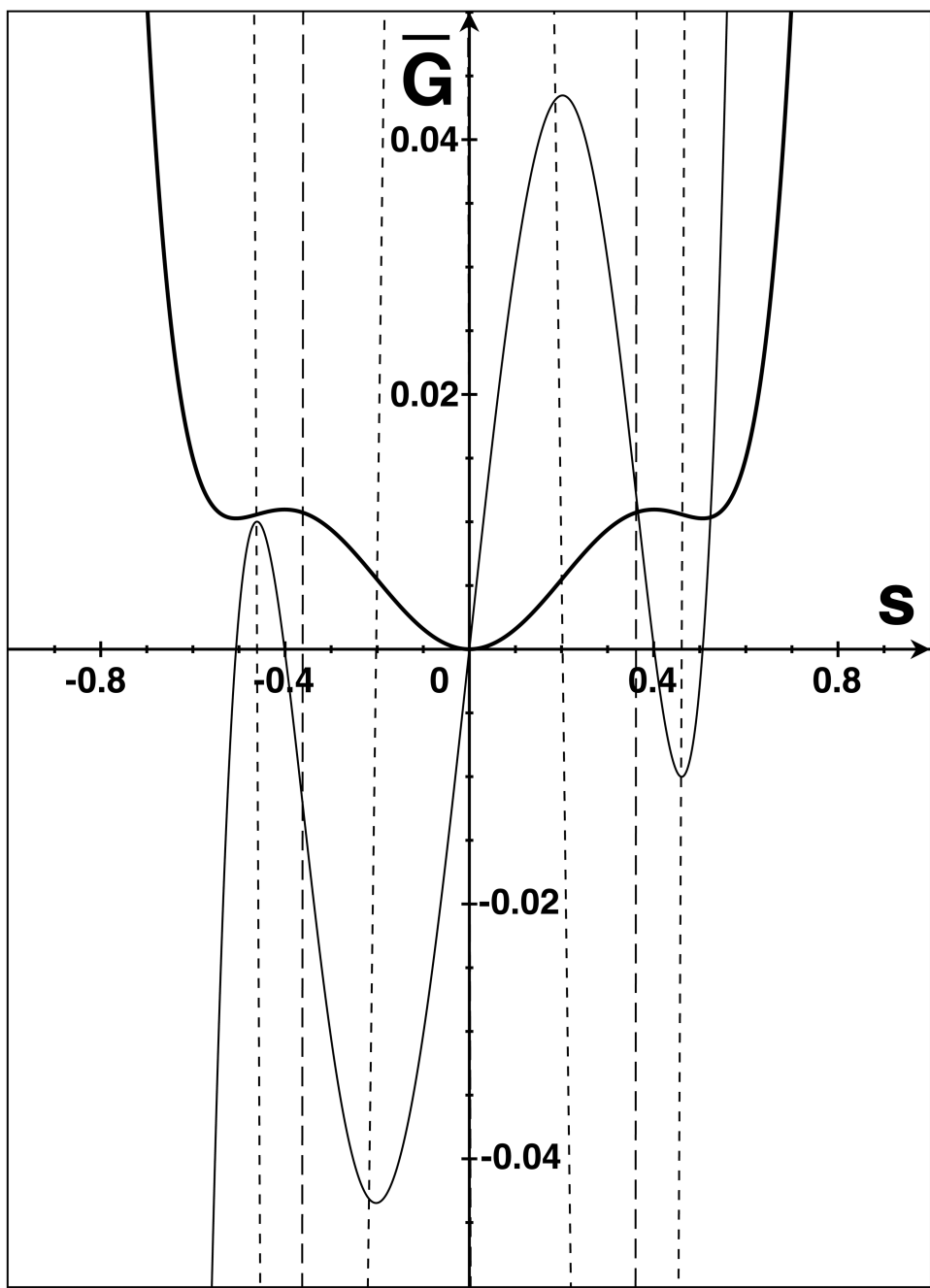


Fig. 5 (continued). (E) Temperature at $T_C + 20^\circ\text{C}$ for $X = 1$ (pure ilmenite; above the 1st order phase transition for this composition). The stable phase is disordered.

extend down the critical ordering curve and either terminate at a *regular critical point*² or at absolute zero. Further analysis aimed at distinguishing the two possibilities necessitates calibration of the remaining model parameters.

Calibration of the Model—Miscibility Gap Data

Experimental data from Burton (ms, 1982) that place constraints on the extent of solid solution in the Fe_2O_3 - FeTiO_3 binary are plotted in figure 6. These experiments provide information on the locations of the left- and right-limbs of a miscibility gap in the system. While theory would suggest that the left-hand limb is closely related to the position of the critical ordering curve (Burton and Davidson, 1988), the symmetry transition does not constrain the position of the right-hand limb, and the experimental data of Burton (ms, 1982) are permissive with respect to its placement. In this section we choose an approximate location for this limb that is roughly consistent with these experimental data, doing so largely to explore the permissible topologies of the gap that are permitted by our model calibration of the cation-ordering data. In a later section, we refine the location of the right limb utilizing additional experimental data involving Fe-Ti exchange between rhombohedral oxide and spinel.

Since compositions of equilibrium coexisting phases must have identical chemical potentials of endmember components, the miscibility gap data of figure 6 may be utilized to constrain a preliminary calibration of the remaining model parameters:

$$\mu_{\text{FeTiO}_3}^{ll-poor} = \mu_{\text{FeTiO}_3}^{ll-rich} \quad (41)$$

$$\mu_{\text{Fe}_2\text{O}_3}^{ll-poor} = \mu_{\text{Fe}_2\text{O}_3}^{ll-rich} \quad (42)$$

The chemical potentials of FeTiO_3 and Fe_2O_3 are obtained from the model equation for \bar{G} by application of the extended Darken relation (Ghiorso, 1990b)

$$\mu_{\text{FeTiO}_3}^{\text{rhm}} = \bar{G} + (1 - X) \frac{\partial \bar{G}}{\partial X} - s \frac{\partial \bar{G}}{\partial s} \quad (43)$$

$$\mu_{\text{Fe}_2\text{O}_3}^{\text{rhm}} = \bar{G} - X \frac{\partial \bar{G}}{\partial X} - s \frac{\partial \bar{G}}{\partial s} \quad (44)$$

Substitution into equations (41) and (42) gives the following model expressions for the limbs of the miscibility gap

$$\bar{G}\Big|_{X_{ll-poor}} + (1 - X_{ll-poor}) \frac{\partial \bar{G}}{\partial X}\Big|_{ll-poor} = \bar{G}\Big|_{X_{ll-rich}} + (1 - X_{ll-rich}) \frac{\partial \bar{G}}{\partial X}\Big|_{ll-rich} \quad (45)$$

$$\bar{G}\Big|_{X_{ll-poor}} - X_{ll-poor} \frac{\partial \bar{G}}{\partial X}\Big|_{ll-poor} = \bar{G}\Big|_{X_{ll-rich}} - X_{ll-rich} \frac{\partial \bar{G}}{\partial X}\Big|_{ll-rich} \quad (46)$$

where the derivative $\frac{\partial \bar{G}}{\partial X}$ is given by

$$\begin{aligned} \frac{\partial \bar{G}}{\partial X} &= RT \left[\ln \frac{X+s}{2} + \ln \frac{X-s}{2} - 2 \ln(1-X) \right] + \bar{G}_X^* \\ &\quad + 2\bar{G}_{XX}^*X + 3\bar{G}_{XXX}^*X^2 + \bar{G}_{Xss}^*s^2 + 4\bar{G}_{XXXX}^*X^3 + 2\bar{G}_{XXss}^*Xs^2 \end{aligned} \quad (47)$$

² The T - X point where both $\frac{d\bar{G}}{dX}$ and $\frac{d^2\bar{G}}{dX^2}$ are zero (Prigogine and Defay, 1954).

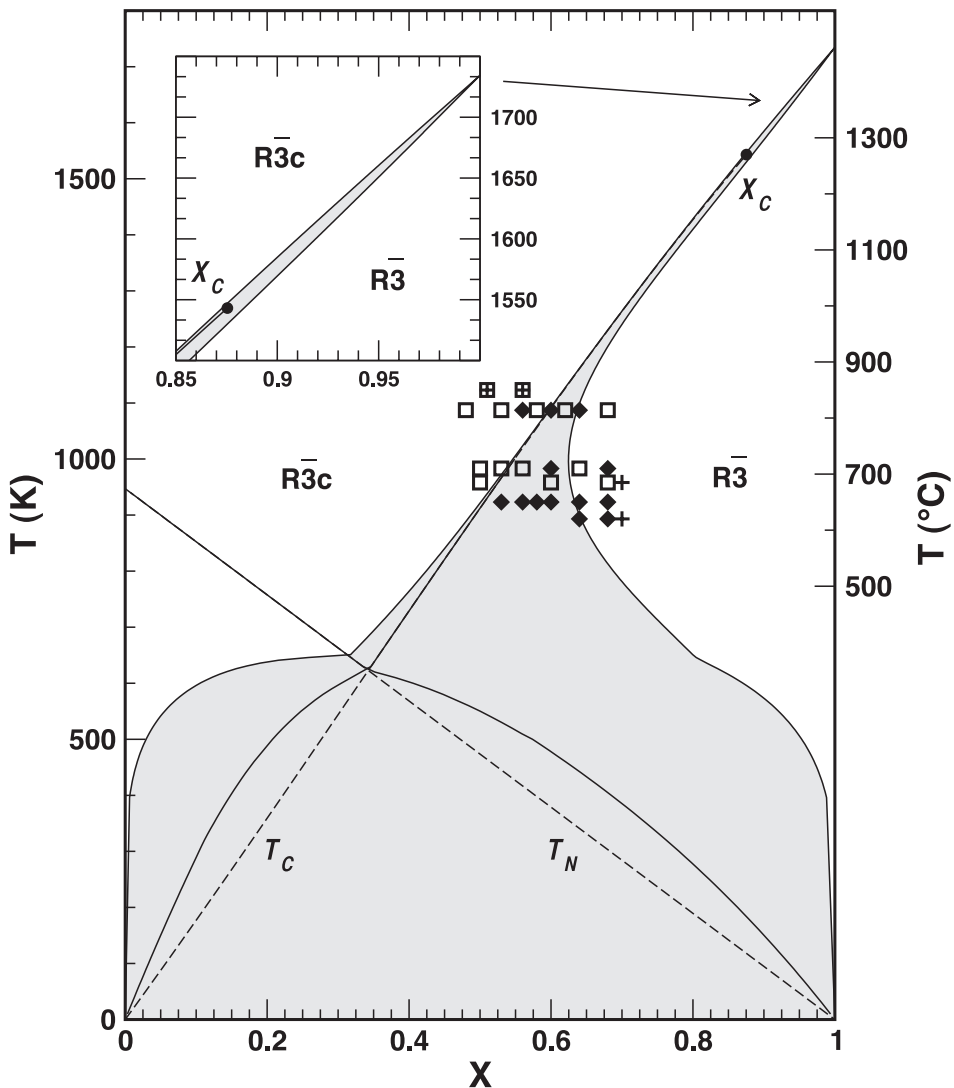


Fig. 6. Miscibility gaps calculated for the system $\text{Fe}_2\text{O}_3\text{-FeTiO}_3$. Experimental constraints are from Burton (ms, 1982). These experiments were conducted in evacuated silica tubes and run for long durations. Data plotted as crosses correspond to single phase starting compositions that remained homogeneous during the experiment. Open squares denote bulk compositions that started out as mixtures of an ilmenite-poor and ilmenite rich phase and homogenized in the course of the experiment. Data plotted as solid diamonds correspond to bulk compositions that started out as mixtures and remained as two-phase assemblages at the close of the experiment. T_c refers to the critical ordering curve and T_N to the path of the Néel curve, the magnetic critical ordering curve that separates the high-temperature paramagnetic structure from the low-temperature antiferromagnetic phase. Both are plotted as solid curves with metastable extensions dashed. The effect of magnetic ordering on the shape of the miscibility gap and the critical ordering curve, as well as the effect of cation-order on the Néel curve are calculated according to the methods discussed in Ghiorso (1997). X_C is the composition along the critical ordering curve where the character of the phase transition changes from second-to first-order. (A) $W_{Hm-II} = 21.2 \text{ kJ/mol}$, $\Delta W_{Hm-II} = 0 \text{ kJ/mol}$.

The ordering variable derivatives that should be found in equations (45) and (46) have vanished because both phases are assumed to be in a state of equilibrium cation-order. A calibration of the miscibility gap data involves determining optimal values for model

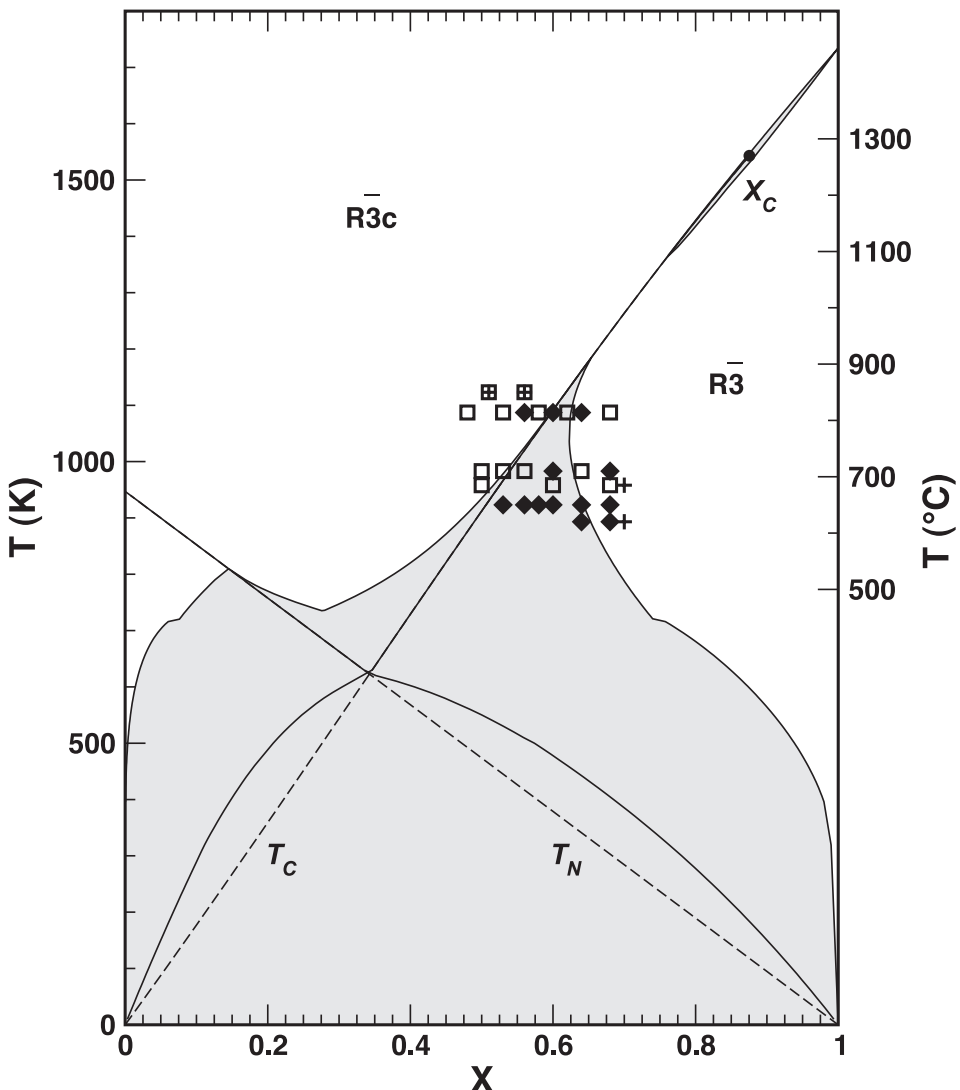


Fig. 6 (continued). (B) $W_{Hm-II} = 27.2 \text{ kJ/mol}$, $\Delta W_{Hm-II} = 8.5 \text{ kJ/mol}$. Note the development of the “magnetic cone” and the formation of two tricritical points (Burton and Davidson, 1988) that close and open the miscibility gap along the critical ordering curve.

parameters that are otherwise unconstrained by our previous analysis of the cation-ordering data (table 2). Trial and error solution of equations (45) and (46) reveals that there is a family of parameter values that satisfy the constraints:

$$\Delta W_{Hm-II} = 1.7185 \times W_{Hm-II} - 38.226 \quad (48)$$

and give essentially the same right-hand limb location at $\sim 700^\circ\text{C}$. This family of solutions represents a compromise among inconsistent experimental results (fig. 6, see legend).

The dependence of ΔW_{Hm-II} on W_{Hm-II} implies a trade-off between the height of the gap (W_{Hm-II}) and its asymmetry (ΔW_{Hm-II}). This family of solutions generates gaps of three distinct topologies, which are illustrated in figures 6A–6C.

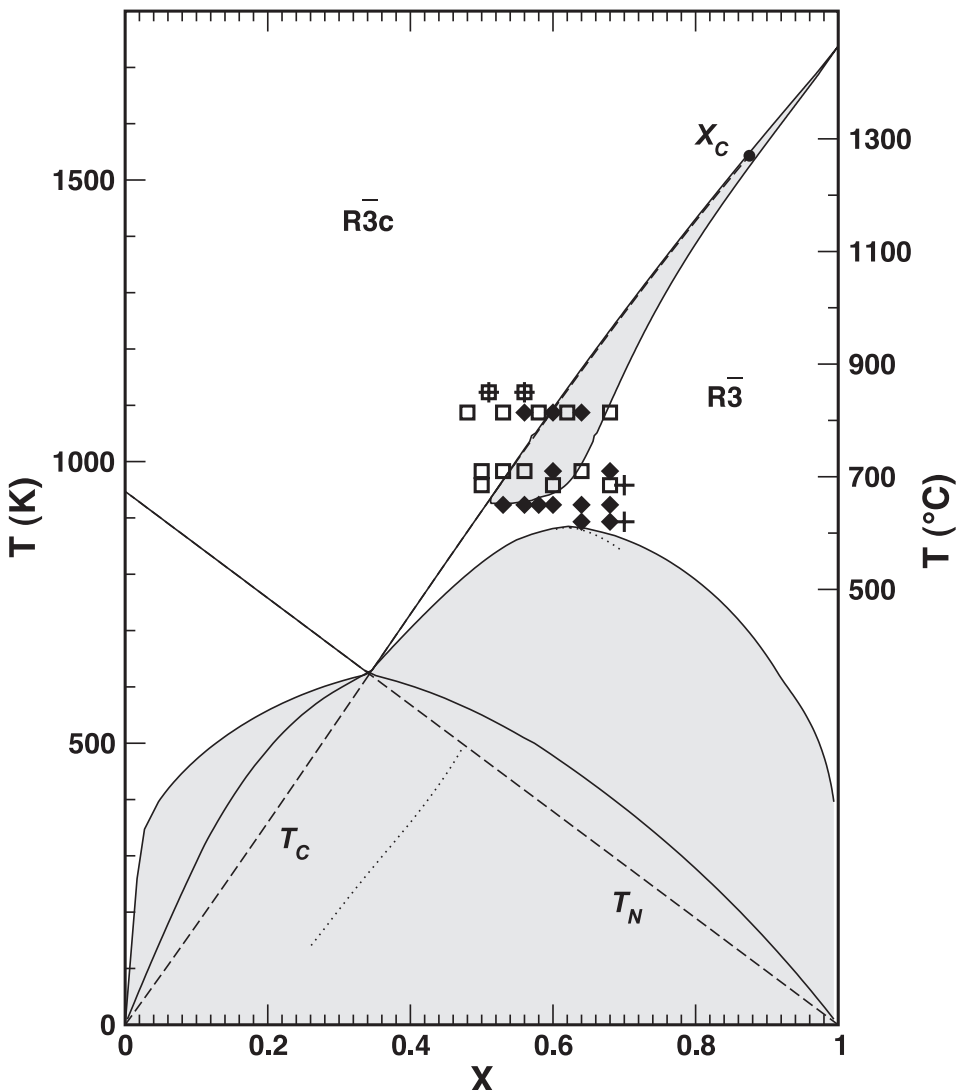


Fig. 6 (continued). (C) $W_{Hm-II} = 16.2 \text{ kJ/mol}$, $\Delta W_{Hm-II} = -10.4 \text{ kJ/mol}$. Note the separation of the low-temperature miscibility gap from the high-temperature one, resulting in a critical endpoint (Burton and Davidson, 1988) for the latter that terminates on the critical ordering curve. The consolute point of the lower- T_{gap} is terminal to the spinode, indicated by the dotted curve.

Figure 6A corresponds to a solution with ΔW_{Hm-II} equal to zero. The peculiar shape of the gap is dictated by the symmetry breaking phase transition; the ilmenite-poor phase is disordered and the ilmenite-rich phase is ordered, and the gap follows the critical ordering curve. The width of the gap is essentially determined by the parameter W_{Hm-II} and the asymmetry of the gap by the temperature-dependence of the cation-ordering state; the reduction of entropy associated with cation-ordering destabilizes the ilmenite-rich phase and serves to broaden the immiscible region. Note that there is no critical point between the lower temperature experimental brackets and high-temperature first order transition region. Consequently, the miscibility gap

TABLE 2
Preferred values of model parameters

Parameter	Value (kJ/mol)		Source/constraint
	Fe-Ti sub-system	Super-system	
μ_{Hm}^o			Berman (1988)
μ_{II}^o			Berman (1988)
W_{Hm-II}	22.688	22.536	Two-oxide equilibria (miscibility gap analysis)
ΔW_{Hm-II}	-5.064	-5.627	Two-oxide equilibria (miscibility gap analysis)
$\Delta^2 W_{Hm-II}$	0	0	Ordering analysis
W_{II-II}	69.908	69.908	Ordering analysis
$\Delta^2 W_{II-II}$	12.756	12.756	Ordering analysis
$W_{Hm-II-II}$	-1.960	-0.833	Ordering analysis, depends on value for ΔW_{Hm-II} as $\frac{\Delta W_{Hm-II}}{2} + \frac{W_{Hm-II-II}}{4} = -3.022$.
ΔW_{Hm-II^3}	0	0	Ordering analysis
ΔH^o	-0.728	-2.039	Correction to standard state properties of two-oxide exchange reaction; indirectly, the negative of the correction to the standard state properties of ulvöspinel.
ΔS^o	-0.2	-1.248	J/K-mol
α	0.073430	0.073021	Two-oxide equilibria
$W_{Hm-Gk}, W_{Hm-Py},$		$\equiv W_{Hm-II}$	(estimate)
$W_{II-Cr}, W_{Gk-Cr}, W_{Py-Cr}$			
$\Delta W_{Hm-Gk}, \Delta W_{Hm-Py},$		$\equiv \Delta W_{Hm-II}$	(estimate)
$\Delta W_{II-Cr}, \Delta W_{Gk-Cr}, \Delta W_{Py-Cr}$			
W_{II-Gk}	2.6		Pownceby and Fisher-White (1999)
$W_{(II-Gk)^T}$	88.100		Two-oxide equilibria
W_{Gk-Gk}, W_{Py-Py}		$\equiv W_{II-II}$	(estimate)
$\Delta^2 W_{Gk-Gk}, \Delta^2 W_{Py-Py}$		$\equiv \Delta^2 W_{II-II}$	(estimate)
$W_{Hm-Gk-Gk}, W_{Hm-Py-Py}$		$\equiv W_{Hm-II-II}$	(estimate)
W_{II-Py}	2.2		O'Neill and others (1989)
$W_{(II-Py)^T}$	30.244		Two-oxide equilibria
W_{Gk-Py}		$\equiv W_{II-Gk}$	(estimate)
$W_{(Gk-Py)^T}$		$\equiv W_{II-Gk}$	(estimate)
W_{Hm-Cr}	69.0		± 5 ; regular solution approximation estimated by Majzlan and others, 2002
ΔW_{Hm-Cr}	0		regular solution approximation estimated by Majzlan and others, 2002

extends continuously as temperature increases to pure ilmenite. This result is in contrast to the previously calculated phase diagram (Burton, 1984; Ghiorso, 1990a; Harrison, 2006) where the gap terminated at a tricritical point on the critical ordering curve (Burton and Davidson, 1988) at a temperature ~ 1025 K. The widening of the gap at lower temperatures is caused by magnetic ordering of the ilmenite-poor phase, and is calculated according to analysis and calibration of Ghiorso (1997).

Figure 6B displays a gap generated with a solution that has ΔW_{Hm-II} strongly positive, inducing asymmetry towards the hematite side of the diagram. This choice necessitates a larger value of W_{Hm-II} to satisfy equation (48). For this solution the lower gap has two peaks or “cones.” The first at $X \sim 0.15$ is generated by the magnetic spin-ordering transition (Ghiorso, 1997), while the second at about $X \sim 0.65$ is related to the cation-order-disorder phase transition. In contrast to figure 6A, two critical points are present along the critical ordering curve, delimiting two separate immiscible regions. The lower- T and upper- T gaps terminate at these critical points and between them is a compositional interval where the solid solution changes symmetry upon cooling without passing through an interval of phase separation. The lower- T gap in figure 6B resembles more closely the calculation of Ghiorso (1990a, 1997). The upper- T gap is present entirely as a consequence of the first-order phase transition to the ilmenite-rich side of X_C . Recall that a miscibility gap extends into the binary from pure ilmenite as a consequence of the first order nature of the symmetry breaking phase transition. This gap must extend to compositions at least as Fe_2O_3 -rich as X_C , at which point the transition changes to second order, and the gap is permitted to close if the entropy of mixing can contribute a sufficiently negative contribution to the Gibbs energy of solution to overwhelm the positive enthalpy of mixing. The model parameter values that give rise to the gap shown in figure 6B imply an enthalpy of mixing that permits this closure of the high-temperature gap. The gap reopens again at lower T because the entropic contribution to the Gibbs energy is diminished with falling T and the enthalpic term once again wins out. As in figure 6A, the widening of the miscibility gap at lower temperatures (< 700 K) is caused by magnetic ordering.

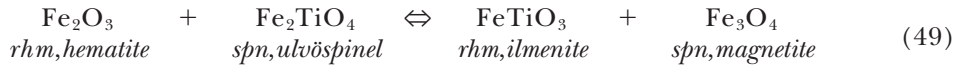
The gap plotted in figure 6C represents the situation where ΔW_{Hm-II} is strongly negative, which shifts the excess vibrational Gibbs free energy to higher ilmenite contents. In order to fit the experimental constraints, this value of ΔW_{Hm-II} necessitates a smaller W_{Hm-II} . The result is again two miscibility gaps, but in this case the lower gap pulls away from the critical ordering curve and terminates at a critical point *within* the low symmetry region of composition-space. At temperatures below about ~ 620 K, an antiferromagnetic hematite-rich phase coexists with ordered ilmenite_{ss}, while above that temperature the limbs of the lower gap are defined by a weakly ordered hematite-rich composition which coexists with a strongly ordered ilmenite-rich phase. The high temperature gap satisfies the experimental brackets and terminates on T_C at a critical point. It extends continuously to pure ilmenite following the critical ordering curve. As in the gap displayed in figure 6A, and the high-temperature gap plotted in figure 6B, the high- T gap in figure 6C associates low- and high-symmetry phases.

In principle, model parameters determined from the cation-ordering and miscibility gap constraints provide a complete representation of the thermodynamic mixing properties of the $FeTiO_3-Fe_2O_3$ join. However, as is witnessed by the variety of permissible miscibility gaps shown in figure 6, these experimental constraints are insufficient to differentiate among the allowable phase diagram topologies. Additional data are required to make this selection, and to that end two-oxide equilibria and heat of solution measurements are examined next.

Calibration of the Model—Two Oxide Equilibria

A wealth of experimental data are available that document the compositions of coexisting rhombohedral (*rhm*) and cubic (*spn*) Fe-Ti oxides that have been equili-

brated under conditions of known temperature, pressure and oxygen fugacity. These data can be evaluated in terms of the following *exchange*:



and oxidation-reduction (*redox*)



equilibria. Equation (49) leads to the thermodynamic equilibrium constraint

$$\Delta \bar{G}^{\text{exchange}} = 0 = (\mu_{\text{FeTiO}_3}^{\text{rhm}} - \mu_{\text{Fe}_2\text{O}_3}^{\text{rhm}}) - (\mu_{\text{Fe}_2\text{TiO}_4}^{\text{spn}} - \mu_{\text{Fe}_3\text{O}_4}^{\text{spn}}) \quad (51)$$

while equation (50) results in

$$\Delta \bar{G}^{\text{redox}} = 0 = (4\mu_{\text{Fe}_3\text{O}_4}^{\text{spn}} + \mu_{\text{O}_2}^{\text{gas}}) - 6\mu_{\text{Fe}_2\text{O}_3}^{\text{rhm}} \quad (52)$$

The right-hand-sides of equations (51) and (52) may be estimated from previously published activity-composition relations for spinels (Sack and Ghiorso, 1991a, 1991b), the model parameters of table 2, and from standard state properties of the endmembers. The latter are taken from Berman (1988) for ilmenite, hematite, magnetite and oxygen gas. The standard state entropy of ulvöspinel is taken from Sack and Ghiorso (1991a) and a new expression for the high-temperature isobaric heat capacity of ulvöspinel is derived in the Appendix. A preliminary estimate of the enthalpy of formation of ulvöspinel is obtained from Ghiorso and Sack (1991a). Both the entropy and the enthalpy of ulvöspinel can be optimized to better accommodate the two-oxide equilibria.

Data from Lattard and others (2005) and from Evans and others (2006) are evaluated in figures 7 and 8, where the exchange Gibbs free energy of equation (51) and the redox Gibbs free energy of equation (52) are plotted as a function of the ilmenite content of the rhombohedral phase. Phases in the lower temperature experiments of Evans and others (2006) contain aluminum, but this element partitions largely into the spinel phase (as the component hercynite— FeAl_2O_4) and its presence and effect on the chemical potentials of Fe_2TiO_4 and Fe_3O_4 are accounted for in the model of Sack and Ghiorso (1991a, 1991b). Figures 7A and 8A represent recovery of the exchange and redox energies for the case where $\Delta W_{\text{Hm}-\text{Il}}$ is near zero, equivalent to the miscibility gap solution displayed in figure 6A. Figures 7B and 8B display reaction energies calculated for the case of strongly positive values of $\Delta W_{\text{Hm}-\text{Il}}$ corresponding to figure 6B. Calculated reaction energies plotted in figures 7C and 8C correspond to a solution with strongly negative $\Delta W_{\text{Hm}-\text{Il}}$, which yields the miscibility gap shown in figure 6C.

The data plotted in figure 7 should show no dependence on X and the average value of the exchange energy should be zero. Permissible adjustments to the standard state enthalpy of ulvöspinel can raise or lower the plotted points, but cannot eliminate any compositional correlation exhibited by the data array. The redox energies plotted in figure 8 cannot be raised or lowered, because the standard state properties of the reaction are fixed by Berman (1988) from experimental data on the hematite-magnetite buffer. As with the exchange equilibria, the data plotted in figure 8 should show no dependence on X . Clearly, all three of the solutions examined in figures 7 and 8 fail to accommodate the two-oxide phase equilibrium data. Focusing on the redox energies, the least problematic solution is the one with near-zero $\Delta W_{\text{Hm}-\text{Il}}$, as the average value of the redox energy approaches zero for $X < 0.6$ for this solution. However, even for this solution the plotted arrays of exchange and redox energies

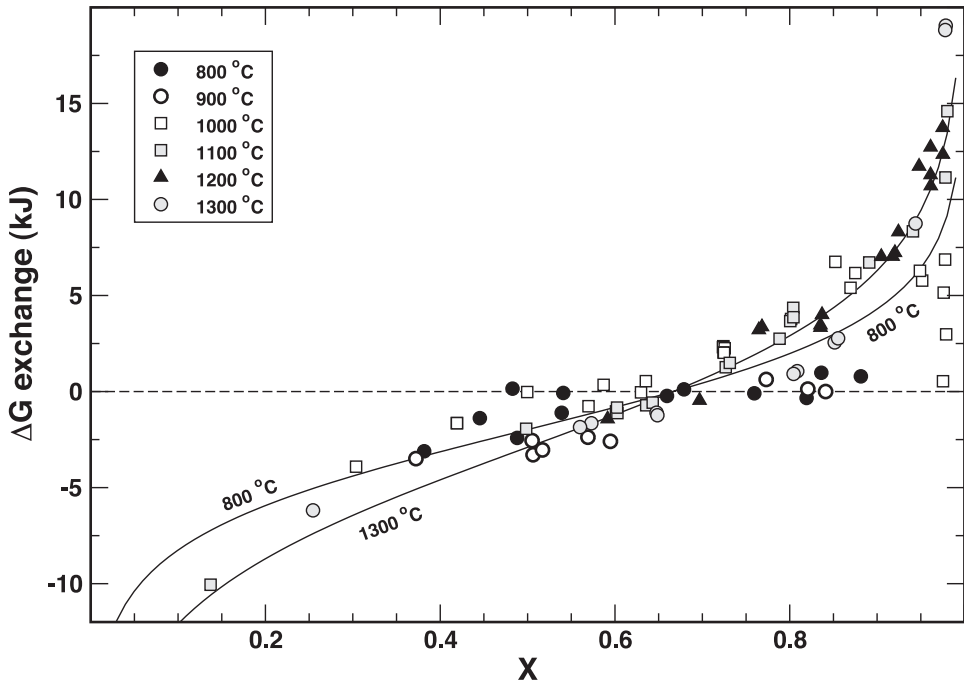


Fig. 7. Gibbs free energy of the Fe-Ti exchange reaction between coexisting rhombohedral and spinel oxides, defined as in equation (51). Data plotted are derived from the 1000–1300°C one atmosphere experiments in the system Fe-Ti-O of Lillard and others (2005) and the 800–900°C synthetic haplorhyolite experiments of Evans and others (2006). The curves, which represent SRO corrections to the $\Delta G_{exchange}$, are plots of the function $\alpha 2RT [\ln(X/2) - \ln(1-X)]$ at 800°C and 1300°C, as labeled. (a) $W_{Hm-II} = 21.2$ kJ/mol, $\Delta W_{Hm-II} = 0$ kJ/mol, $\alpha = 0.16$.

suggest a functional dependence that implies failure of the model to capture some essential feature of the energetics.

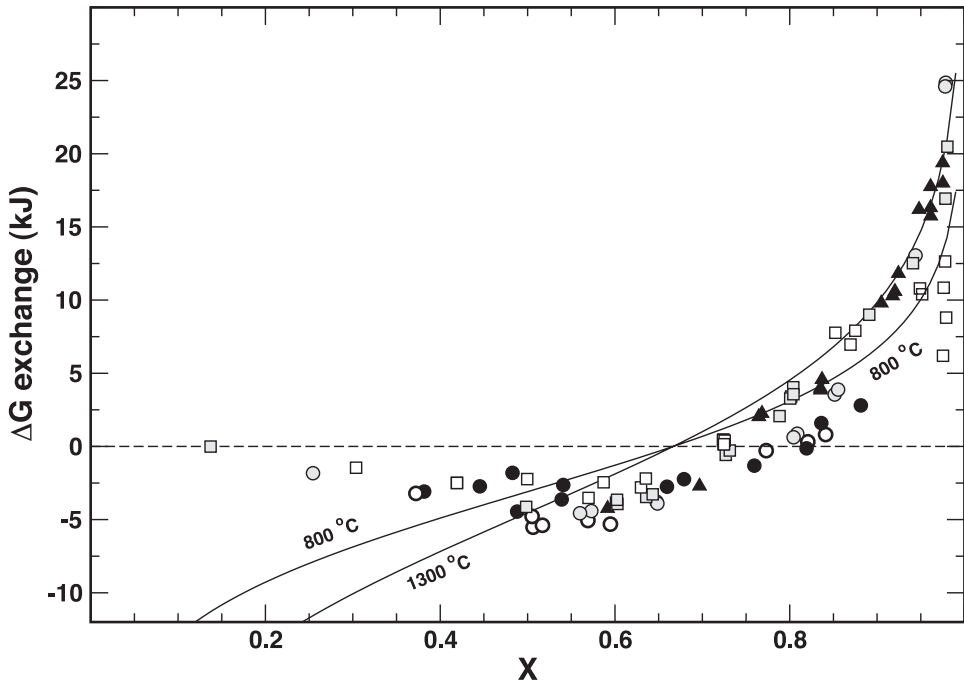
To investigate the cause of the misfit, equation (51) is expanded to

$$\begin{aligned} \Delta \bar{G}_{exchange}^* = 0 = RT \left[\ln \frac{X+s}{2} + \ln \frac{X-s}{2} - 2 \ln(1-X) \right] + \bar{G}_X^* + 2\bar{G}_{XX}^*X + 3\bar{G}_{XXX}^*X^2 \\ + \bar{G}_{Xss}^*s^2 + 4\bar{G}_{XXXs}^*Xs^3 + 2\bar{G}_{XXss}^*Xs^2 - (\mu_{Fe_2TiO_4}^{spn} - \mu_{Fe_3O_4}^{spn}) \quad (53) \end{aligned}$$

and Taylor coefficients are substituted to identify relevant model parameters

$$\begin{aligned} \Delta \bar{G}_{exchange}^* = (\mu_H^o - \mu_{Hm}^o) - (\mu_{Fe_2TiO_4}^{spn} - \mu_{Fe_3O_4}^{spn}) + RT \left[\ln \frac{X+s}{2} + \ln \frac{X-s}{2} - 2 \ln(1-X) \right] \\ + 2 \left(\frac{W_{II-II}}{4} + \frac{\Delta W_{Hm-II}}{2} + \frac{W_{Hm-II-II}}{4} \right) X - 3 \left(\frac{\Delta W_{Hm-II}}{2} + \frac{W_{Hm-II-II}}{4} \right) (3X^2 - s^2) + \frac{\Delta^2 W_{II-II}}{2} Xs^2 \\ + [W_{Hm-II} + (1-2X)\Delta W_{Hm-II}] (1-2X) + 2X(1-X)\Delta W_{Hm-II} \quad (54) \end{aligned}$$

Recall that the cation-ordering analysis fixes values for the parameter combinations in the 4th, 5th and 6th terms in equation (54), while the standard state contributions (the 1st and 2nd terms) can only displace points along the ordinate in figures 7 and 8. The adjustable model parameters that govern the slope and curvature of the data array are

Fig. 7 (continued). (b) $W_{Hm-II} = 27.2 \text{ kJ/mol}$, $\Delta W_{Hm-II} = 8.5 \text{ kJ/mol}$, $\alpha = 0.14$.

W_{Hm-II} and ΔW_{Hm-II} , which are the same parameters that influence the width and asymmetry of the miscibility gap (see above). Importantly, both parameters can at best provide a quadratic correction to the reaction energy. The misfit displayed in figures 7 and 8 however, is not quadratic in X . It is instead logarithmic in form, and is proportional to the function $\ln(X) - \ln(1-X) - \ln(2)$. This is illustrated in figures 7A and 8A by the solid curves, which are plots of $\alpha 2RT[\ln(X) - \ln(1-X) - \ln(2)]$, where the proportionality constant α is chosen so that the curve passes through the data array. What is the origin of this logarithmic term? The clue comes from the configurational contribution to the exchange reaction [eq (53)], that is,

$$RT \left[\ln \frac{X+s}{2} + \ln \frac{X-s}{2} - 2 \ln(1-X) \right] \quad (55)$$

which in the limit of the disordered phase ($s \rightarrow 0$) becomes

$$2RT [\ln X - \ln(1-X) - \ln 2] \quad (56)$$

Equation (56) is identical (within a constant multiple) to the misfit function implied by the exchange data. This analysis suggests that the configurational entropy of the system be modified from equation (11) to

$$\begin{aligned} \bar{S}^{conf} = -R & \left[2(1-X) \ln(1-X) + (X+s) \ln \frac{X+s}{2} + (X-s) \ln \frac{X-s}{2} \right] \\ & + \alpha 2R [(1-X) \ln(1-X) + X \ln X - X \ln 2] \end{aligned} \quad (57)$$

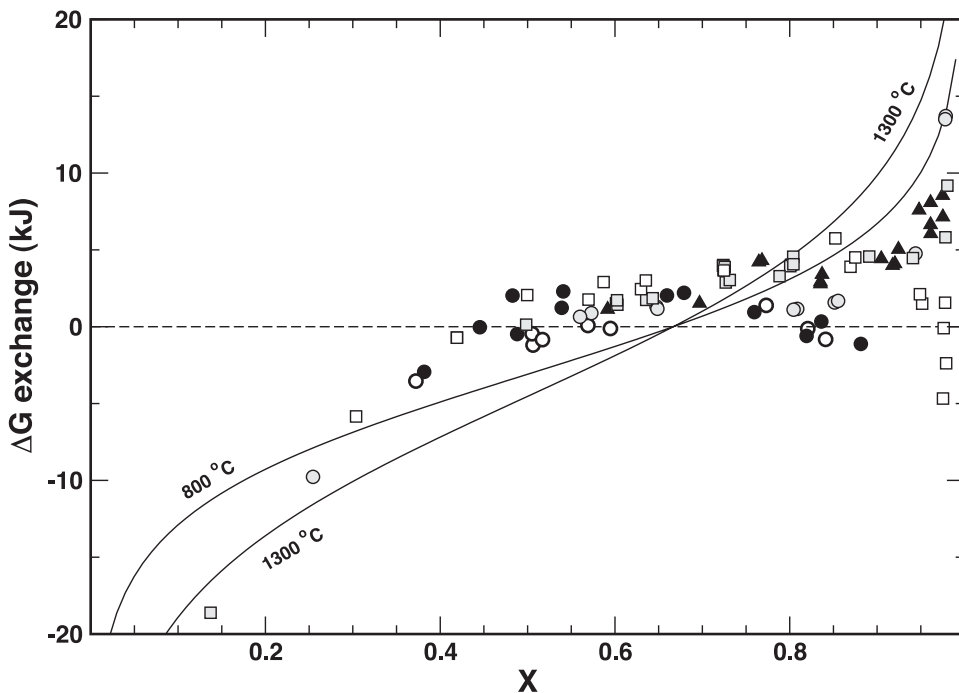


Fig. 7 (continued). (c) $W_{Hm-II} = 16.2 \text{ kJ/mol}$, $\Delta W_{Hm-II} = -10.4 \text{ kJ/mol}$.

which has the compositional derivative

$$\frac{\partial \bar{G}^{conf}}{\partial X} = RT \left[\ln \frac{X+s}{2} + \ln \frac{X-s}{2} - 2 \ln(1-X) \right] - \alpha 2RT [\ln X - \ln(1-X) - \ln 2] \quad (58)$$

If α is positive, the origin of this correction can be justified in terms of short-range ordering (SRO) of Fe^{2+} and Ti^{4+} cations, including the formation of local clusters of cations. Such ordering diminishes the entropy developed in the fully random high-symmetry structural state. Because the long-range cation-ordering is captured by the model developed above without SRO, and because the exchange/redox data appear to demand a correction term that is independent of the state of long-range cation-order (for example, figs. 7A and 8A), the SRO correction term embodied in equation (57) does not include a long-range ordering contribution. Harrison and Redfern (2001) suggested a similar approach to dealing with SRO in the ilmenite-hematite series by scaling the point entropy. CVM calculations performed by these workers show that at temperatures of $\sim 800^\circ\text{C}$, the point entropy should be scaled by a factor of ~ 0.9 to accommodate the effects of SRO. In principle, one would expect α in equation (57) to be dependent on both composition and intensive thermodynamic variables; the exchange/redox data of figures 7 and 8 suggest that a constant approximation is sufficient for this data set.

In figure 9, a calibration of W_{Hm-II} , ΔW_{Hm-II} , and α , and both ΔH° and ΔS° of equation (51) is obtained by optimization of the exchange/redox data set. Parameter values are tabulated in table 2. It is not appropriate to extract only values for α , ΔH° , and ΔS° , fixing W_{Hm-II} and ΔW_{Hm-II} from the miscibility gap analysis, because the

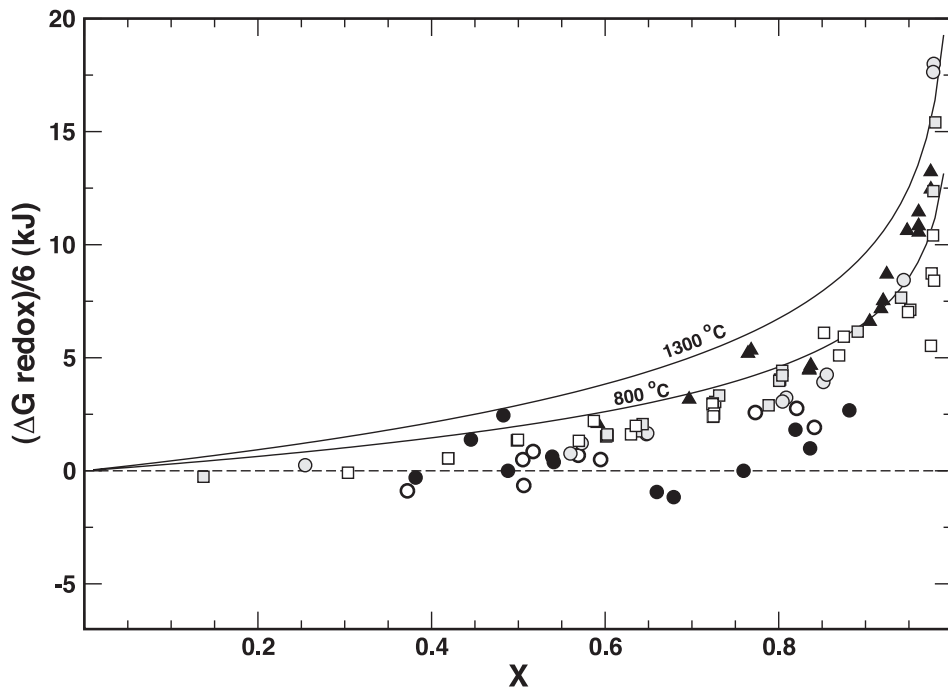


Fig. 8. Gibbs free energy of the Fe-Ti redox reaction between coexisting rhombohedral and spinel oxides, defined as in equation (52). The correction curves (as in fig. 7) are plots of the function $\alpha 2RT [\ln(X/2) - \ln(1-X)]$ at 800°C and 1300°C, as labeled. (A) $W_{Hm-II} = 21.2$ kJ/mol, $\Delta W_{Hm-II} = 0$ kJ/mol, $\alpha = 0.16$.

latter parameters are correlated to α ; the larger the value of α , the smaller the configurational entropy, and the smaller the non-ideal contribution to the Gibbs free energy (W_{Hm-II} , ΔW_{Hm-II}) that is required to accommodate the miscibility gap experimental constraints. Figure 9 shows that the parameterization optimized from the two-oxide equilibria data does a reasonable job in recovering the measurements, except at high-mole fractions of ilmenite, where small compositional uncertainties translate into enormous uncertainties in the exchange energy. The standard error in data recovery is ± 2.683 and ± 1.829 kJ for the exchange and redox equilibria, respectively. If equilibria with $X > 0.9$ are excluded from the statistics, the errors reduce to ± 1.555 and ± 1.078 kJ. There is no simple way to translate this energy uncertainty into more familiar quantities like composition or temperature because the energy is a strongly non-linear function of the natural variables. One way to try to understand this translation is to utilize the model to back-calculate experimental temperatures and oxidation states, varying compositional variables within their measured uncertainty to establish the range of model temperatures and oxygen fugacities that are consistent with the input data. These results are displayed in figure 10.

Several features of the data array plotted in figure 10 are worth noting. First, uncertainties in back-calculated values of oxygen fugacity (fig. 10A) tend to be largest at high mole fractions of ilmenite, which is due primarily to the $\ln(1-X)$ dependence of the chemical potential of hematite. While the range of model temperatures (fig. 10B) back-calculated from the compositional data also reflects this trend, the uncertainties are additionally very large at intermediate to low values of X , which is not due primarily to the $\ln X$ dependence of the chemical potential of ilmenite, but rather to

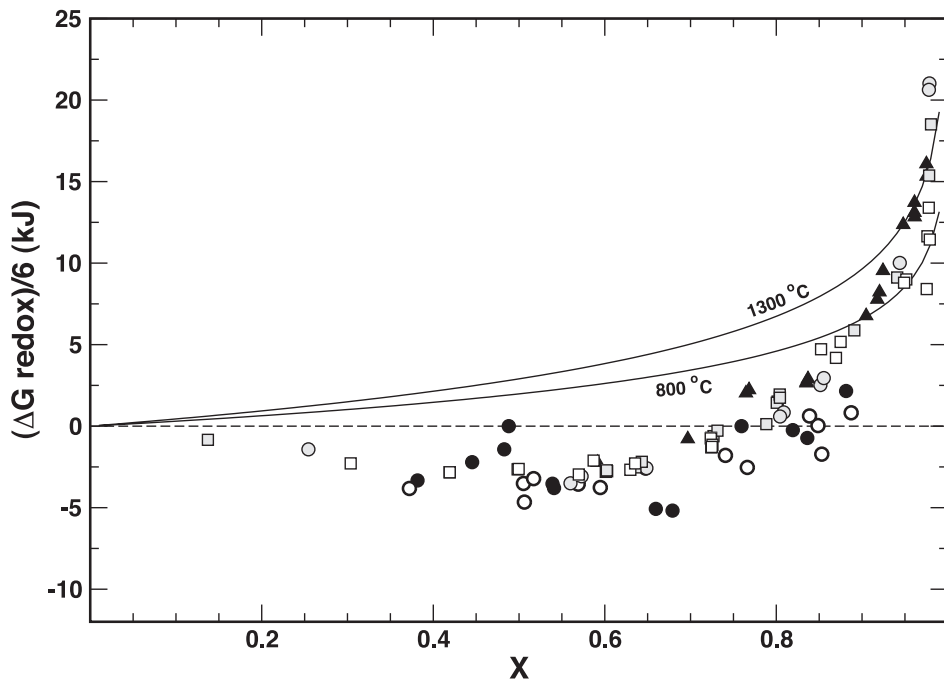


Fig. 8 (continued). (B) $W_{Hm-II} = 27.2 \text{ kJ/mol}$, $\Delta W_{Hm-II} = 8.5 \text{ kJ/mol}$, $\alpha = 0.14$.

the fact that the entropy of the exchange reaction in equation (51) is smaller when the rhombohedral phase is disordered, resulting in greater sensitivity of energy to temperature. The model calibration clearly has difficulty with temperature recovery for the low-temperature experiments; at 900°C the model temperature is systematically high (fig. 10B), a trend that can also be inferred from figure 9A, which displays systematically negative exchange energies for the 900°C data array. The problem may be due to the failure to reach equilibrium in some of the hydrothermal experiments of Evans and others (2006). In figure 11 reversal brackets for two oxide experiments determined by Lindsley and coworkers (see legend and Ghiorso, 1990a, Appendix) are compared to model predictions. The data span a range of oxygen fugacities and are largely consistent with the model calibration developed here. This observation suggests that our model calibration, which is largely dominated by the higher-temperature results of Lillard and others (2005), extrapolates well to lower temperatures.

As practical application of the Fe-Ti oxide geothermometer/oxygen barometer to mineral assemblages in rocks generally applies to the temperature range 700 to 900 °C, it is important to employ as many experimental constraints as are available to model calibration in that temperature range. To this end, and in order to explore the effects of the addition of minor components on the calibration, Evans and others (2006) obtained experimental results in synthetic rhyolite doped with Mg, Mn, and Mg+Mn. These results may be combined with the nominal Fe-Ti experiments to refine the model calibration, but in order to do so the thermodynamic model developed here must be extended to the Fe-Ti-Mg-Mg-Al-O supersystem. This extension is developed next so that all the experimental data may be utilized in calibrating the final model and the geothermometer/oxygen barometer can be more generally applied to natural samples.

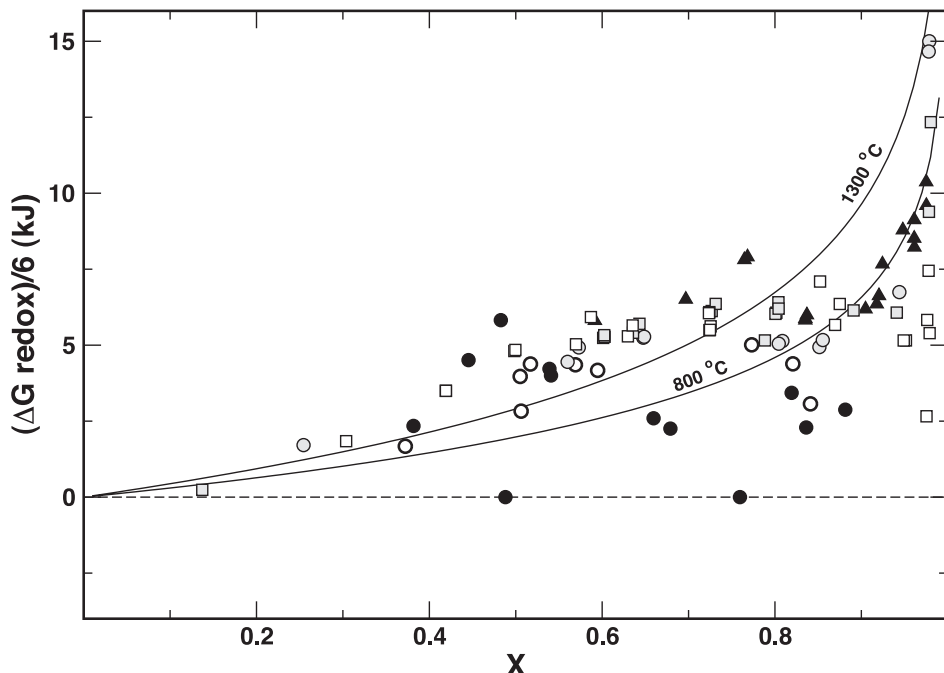


Fig. 8 (continued). (C) $W_{Hm-II} = 16.2 \text{ kJ/mol}$, $\Delta W_{Hm-II} = -10.4 \text{ kJ/mol}$. Data plotted same as figure 7.

Calibration of the Model—Two Oxide Equilibria in the Supersystem

The supersystem corresponds to rhombohedral oxide solid solutions in the five-component composition space with vertices FeTiO_3 - MgTiO_3 - MnTiO_3 - Fe_2O_3 - Al_2O_3 . Two assumptions will be made in extending equation (29) to the supersystem. First, cation-ordering along the Fe_2O_3 - MgTiO_3 join (hematite-geikielite) and along the MnTiO_3 - Fe_2O_3 join (hematite-pyrophanite) will be treated similarly to that along the Fe_2O_3 - FeTiO_3 join. Independent order parameters are adopted for both Mg

$$t = X_{\text{Mg}^{2+}}^A - X_{\text{Mg}^{2+}}^B \quad (59)$$

and Mn

$$u = X_{\text{Mn}^{2+}}^A - X_{\text{Mn}^{2+}}^B \quad (60)$$

which permits non-random Fe^{2+} - Mg^{2+} and Fe^{2+} - Mn^{2+} partitioning to develop in the solid solution with addition of Mg or Mn to the Fe_2O_3 - FeTiO_3 binary. The ordering of Ti^{4+} is consequently no longer defined simply in terms of s , but is instead given by

$$s + t + u = X_{\text{Ti}^{4+}}^B - X_{\text{Ti}^{4+}}^A \quad (61)$$

The second assumption involves the behavior of Al, which is taken to follow that of Fe^{3+} and not partition between A and B octahedral layers. This assumption ignores the existence of the ordered compound along the Fe_2O_3 - Al_2O_3 join (Majzlan and others, 2002), but should be valid for small concentrations of Al typically found in naturally occurring rhombohedral oxides.

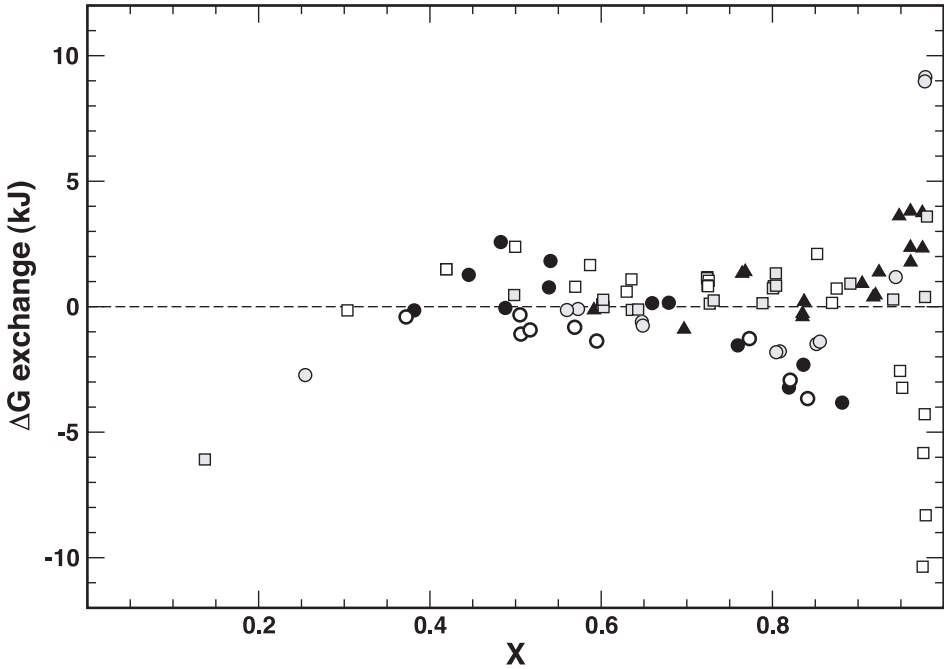


Fig. 9. Gibbs free energy of the Fe-Ti exchange (A) and redox (B) reactions between coexisting rhombohedral and spinel oxides as defined in equations (51) and (52), respectively. Calibration of model parameters from cation-ordering and two-oxide experimental data. $W_{Hm-N} = 22.6882 \text{ kJ/mol}$, $\Delta W_{Hm-N} = -5.06382 \text{ kJ/mol}$, $\alpha = 0.0734302$, $\Delta \bar{H}^{cor,exchg} = -0.727831 \text{ kJ/mol}$, $\Delta \bar{S}^{cor,exchg} = -0.199738 \text{ J/K-mol}$. Data plotted same as fig. 7.

In the supersystem, Y denotes the bulk mole fraction of the MgTiO_3 component, Z the mole fraction of MnTiO_3 component, and C is the mole fraction of the Al_2O_3 component. With these definitions equation (2) becomes

$$X_{Fe^{3+}}^A + X_{Fe^{3+}}^B = 2(1 - X - Y - Z - C) \quad (62)$$

Mass balance requires equation (3) and

$$X_{Mg^{2+}}^A + X_{Mg^{2+}}^B = Y \quad (63)$$

$$X_{Mn^{2+}}^A + X_{Mn^{2+}}^B = Z \quad (64)$$

$$X_{Al^{3+}}^A + X_{Al^{3+}}^B = 2C \quad (65)$$

The mass balance of Ti given previously by equation (4) is now written as

$$X_{Ti}^A + X_{Ti}^B = X + Y + Z \quad (66)$$

Finally, the site constraints of equations (5) and (6) are now written

$$X_{Fe^{3+}}^A + X_{Al^{3+}}^A + X_{Fe^{2+}}^A + X_{Mg^{2+}}^A + X_{Mn^{2+}}^A + X_{Ti}^A = 1 \quad (67)$$

$$X_{Fe^{3+}}^B + X_{Al^{3+}}^B + X_{Fe^{2+}}^B + X_{Mg^{2+}}^B + X_{Mn^{2+}}^B + X_{Ti}^B = 1 \quad (68)$$

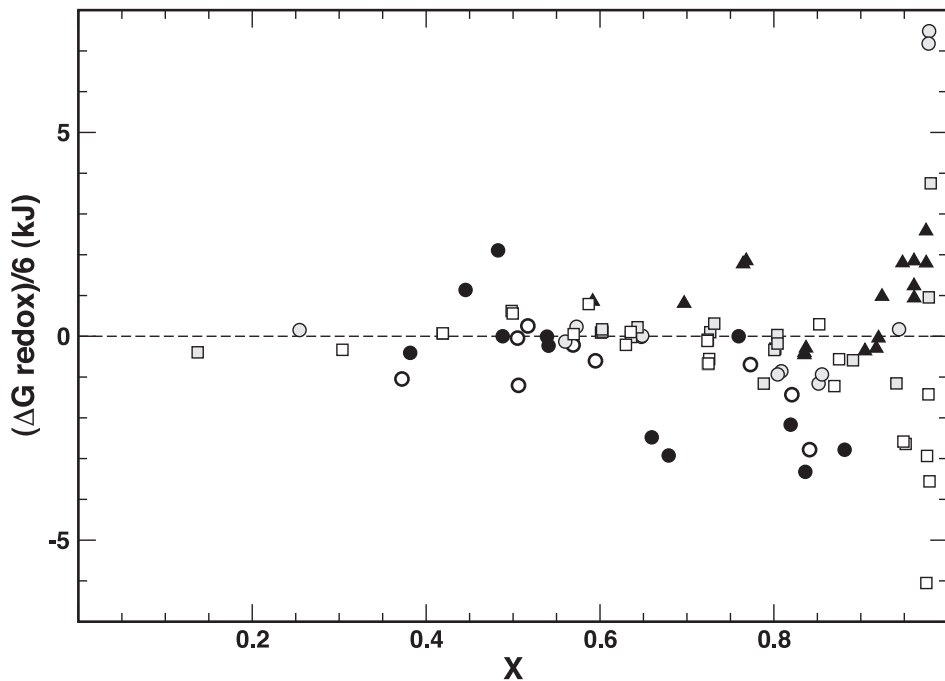


Fig. 9 (continued).

Solving equations (1), (3), (59), (60) and (62)–(68) simultaneously provides definitions for the site mole fractions in terms of composition and ordering variables

$$X_{Fe^{3+}}^A = X_{Fe^{3+}}^B = 1 - X - Y - Z - C \quad (69)$$

$$X_{Fe^{2+}}^A = \frac{X + s}{2} \quad (70)$$

$$X_{Mg^{2+}}^A = \frac{Y + t}{2} \quad (71)$$

$$X_{Mn^{2+}}^A = \frac{Z + u}{2} \quad (72)$$

$$X_{Ti^{4+}}^A = \frac{X + Y + Z - s - t - u}{2} \quad (73)$$

$$X_{Fe^{2+}}^B = \frac{X - s}{2} \quad (74)$$

$$X_{Mg^{2+}}^B = \frac{Y - t}{2} \quad (75)$$

$$X_{Mn^{2+}}^B = \frac{Z - u}{2} \quad (76)$$

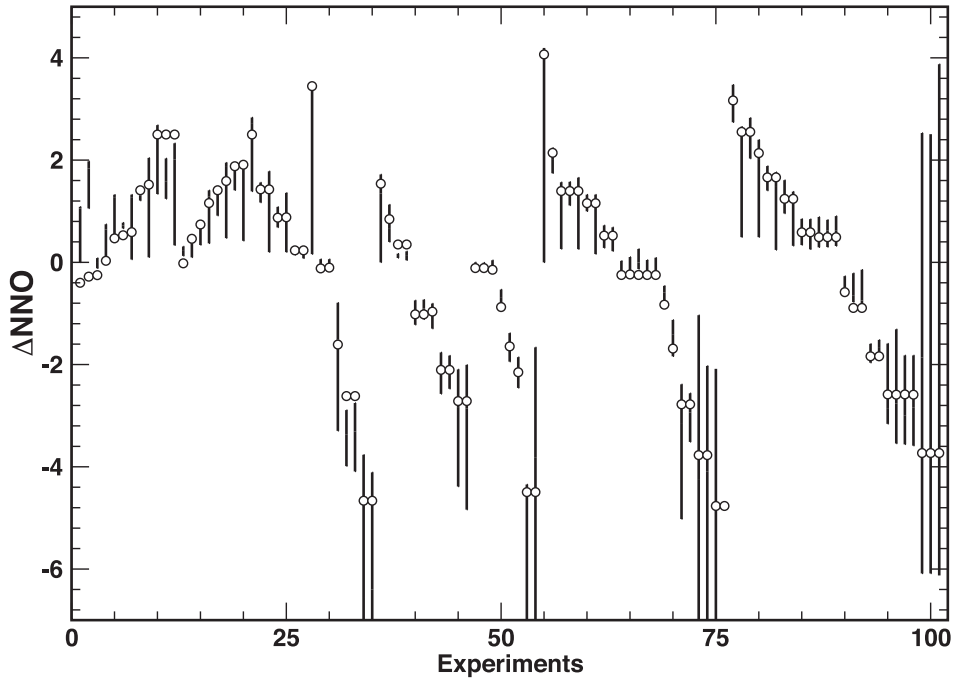


Fig. 10. Recovery of oxidation state (A) and temperature (B) corresponding to the model fit displayed in figure 9. The open circles are plotted at reported values. Model estimates are shown by the vertical solid lines. These estimates are calculated by varying oxide composition of both phases over $\pm 2\sigma$. The abscissa is an arbitrary numerical index of sample number. Within each temperature series (see B) samples are ranked by ilmenite content. Oxidation state (A) is reported in terms of ΔNNO , or relative to the Nickel-nickel oxide oxygen buffer. The buffer calibration of O'Neill and Pownceby (1993) is used.

$$X_{Ti^{4+}}^B = \frac{X + Y + Z + s + t + u}{2} \quad (77)$$

An expression equivalent to equation (57) for the configurational entropy of the supersystem modified for the effects of SRO is developed in the Appendix as equation (124) along with an expression for the vibrational Gibbs free energy of solution, equation (121). The two combine to provide a model for \bar{G} in the supersystem:

$$\bar{G} = RT$$

$$\times \left[\begin{array}{l} \frac{X+s}{2} \ln \frac{X+s}{2} + \frac{X-s}{2} \ln \frac{X-s}{2} - \alpha X \ln \frac{X}{2} + \frac{Y+t}{2} \ln \frac{Y+t}{2} + \frac{Y-t}{2} \ln \frac{Y-t}{2} \\ - \alpha Y \ln \frac{Y}{2} + \frac{Z+u}{2} \ln \frac{Z+u}{2} + \frac{Z-u}{2} \ln \frac{Z-u}{2} - \alpha Z \ln \frac{Z}{2} \\ + \frac{X+Y+Z-s-t-u}{2} \ln \frac{X+Y+Z-s-t-u}{2} \\ + \frac{X+Y+Z+s+t+u}{2} \ln \frac{X+Y+Z+s+t+u}{2} - \alpha(X+Y+Z) \ln \left(\frac{X+Y+Z}{2} \right) \\ + 2(1-\alpha)(1-X-Y-Z-C) \ln (1-X-Y-Z-C) + 2(1-\alpha)C \ln C \\ + (1-X-Y-Z-C)\mu_{Hm}^o + X\mu_{Il}^o + Y\mu_{Gk}^o + Z\mu_{Py}^o + C\mu_{Cr}^o \end{array} \right]$$

Equation (78) continues on next page.

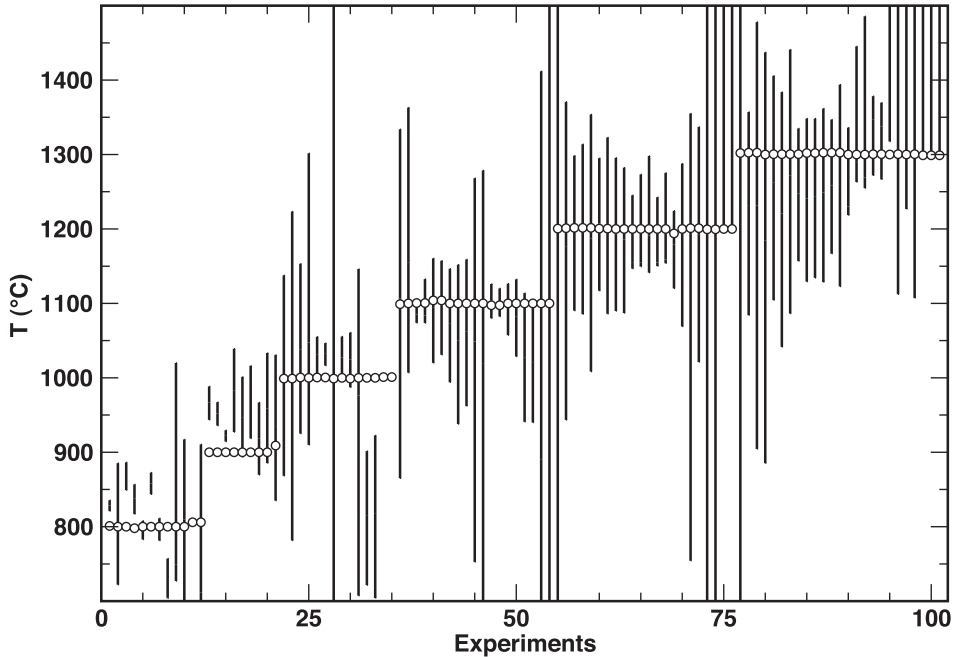


Fig. 10 (continued).

$$\begin{aligned}
& + \{W_{Hm-II} + [(1 - X - Y - Z - C) - X]\Delta W_{Hm-II}\}(1 - X - Y - Z - C)X \\
& + \{W_{Hm-Gk} + [(1 - X - Y - Z - C) - Y]\Delta W_{Hm-Gk}\}(1 - X - Y - Z - C)Y \\
& + \{W_{Hm-Py} + [(1 - X - Y - Z - C) - Z]\Delta W_{Hm-Py}\}(1 - X - Y - Z - C)Z \\
& + \{W_{Hm-Cr} + [(1 - X - Y - Z - C) - C]\Delta W_{Hm-Cr}\}(1 - X - Y - Z - C)C \\
& + \frac{1}{2}XY(W_{Il-Gk} + W_{(Il-Gk)^T}) + \frac{1}{2}st(W_{Il-Gk} - W_{(Il-Gk)^T}) + \frac{1}{2}XZ(W_{Il-Py} + W_{(Il-Py)^T}) \\
& + \frac{1}{2}su(W_{Il-Py} - W_{(Il-Py)^T}) + \frac{1}{2}YZ(W_{Gk-Py} + W_{(Gk-Py)^T}) + \frac{1}{2}tu(W_{Gk-Py} - W_{(Gk-Py)^T}) \\
& + [W_{Il-Cr} + (X - C)\Delta W_{Il-Cr}]XC + [W_{Gk-Cr} + (Y - C)\Delta W_{Gk-Cr}]YC + [W_{Py-Cr}] \\
& + (Z - C)\Delta W_{Py-Cr}]ZC + \left[\frac{W_{Il-II}}{4} + (1 - X - Y - Z - C) \left(\frac{1}{2}\Delta W_{Hm-II} + \frac{W_{Hm-II}}{4} \right) \right. \\
& \left. - \frac{1}{2}C\Delta W_{Il-Cr} \right] (X^2 - s^2) + \left[\frac{W_{Gk-Ck}}{4} + (1 - X - Y - Z - C) \left(\frac{1}{2}\Delta W_{Hm-Gk} \right. \right. \\
& \left. \left. + \frac{W_{Hm-Gk-Gk}}{4} \right) - \frac{1}{2}C\Delta W_{Gk-Cr} \right] (Y^2 - t^2) + \left[\frac{W_{Py-Py}}{4} + (1 - X - Y - Z - C) \right. \\
& \times \left(\frac{1}{2}\Delta W_{Hm-Py} + \frac{W_{Hm-Py-Py}}{4} \right) - \frac{1}{2}C\Delta W_{Py-Cr} \left. \right] (Z^2 - u^2) \\
& + \frac{\Delta^2 W_{Il-II}}{4}(X^2 - s^2)s^2 + \frac{\Delta^2 W_{Gk-Gk}}{4}(Y^2 - t^2)t^2 + \frac{\Delta^2 W_{Py-Py}}{4}(Z^2 - u^2)u^2
\end{aligned} \tag{78}$$

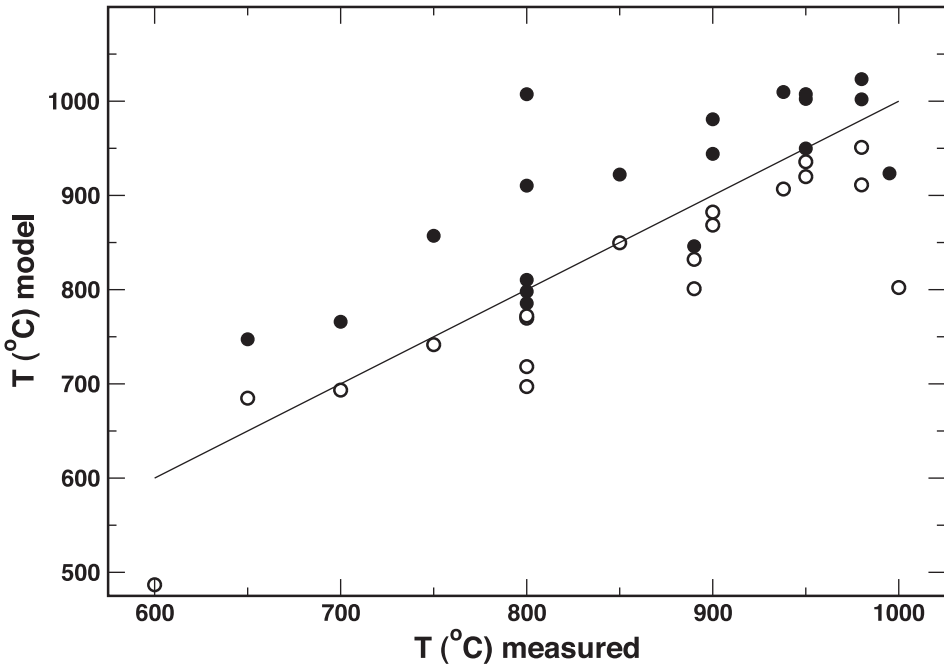


Fig. 11. Recovery of the two-oxide equilibrium brackets of Lindsley and coworkers (data as tabulated in the Appendix of Ghiorso, 1990a). Open circles correspond to model temperatures calculated from experimental oxide pairs grown in hydrothermal experiments where the initial composition of the rhombohedral phase is more ilmenite-rich than the run product. Solid circles correspond to oxide pairs grown from initial conditions where the rhombohedral phase is more ilmenite-poor than the run product.

Although equation (78) looks cumbersome, a close inspection reveals that the terms involving all parameters applicable to the titanite-ferrite joins are similar, and the titanite-aluminate joins are patterned after these. The novel terms in equation (78) involve energetic interactions between the titanites, which includes order parameter coupling. The parameter combination $W_{II-Gk} - W_{(II-Gk)^T}$ for example, governs whether the Gibbs energy is lowered when both Fe^{2+} and Mg^{2+} preferentially partition onto the same octahedral layer ($W_{II-Gk} - W_{(II-Gk)^T} < 0$) thereby enhancing the ordering of Ti^{4+} on the alternate layer, or whether Fe^{2+} and Mg^{2+} partition onto *alternate* octahedral layers ($W_{II-Gk} - W_{(II-Gk)^T} > 0$), which leads to a diminution of the apparent state of Ti^{4+} order.

Along the $\text{FeTiO}_3\text{-MgTiO}_3$ join, equation (78) reduces to

$$\begin{aligned} \bar{G} = RT & \left[\frac{X+s}{2} \ln \frac{X+s}{2} + \frac{X-s}{2} \ln \frac{X-s}{2} - \alpha X \ln \frac{X}{2} + \frac{Y+t}{2} \ln \frac{Y+t}{2} + \frac{Y-t}{2} \ln \frac{Y-t}{2} \right. \\ & \left. - \alpha Y \ln \frac{Y}{2} + \frac{1-s-t}{2} \ln \frac{1-s-t}{2} + \frac{1+s+t}{2} \ln \frac{1+s+t}{2} - \alpha \ln \left(\frac{1}{2}\right) \right] \\ & + X\mu_H^o + Y\mu_G^o + \frac{1}{2} XY(W_{II-Gk} + W_{(II-Gk)^T}) + \frac{1}{2} st(W_{II-Gk} - W_{(II-Gk)^T}) \\ & + \left[\frac{W_{II-II}}{4} + \frac{\Delta^2 W_{II-II}}{4} s^2 \right] (X^2 - s^2) + \left[\frac{W_{Gk-Gk}}{4} + \frac{\Delta^2 W_{Gk-Gk}}{4} t^2 \right] (Y^2 - t^2) \end{aligned} \quad (79)$$

If the solid solutions along this join are essentially fully long-range ordered and if the effects of SRO are negligible, then \bar{G} may be further simplified to

$$\bar{G} \approx RT(X \ln X + Y \ln Y) + X\mu_{II}^o + Y\mu_{Gk}^o + XYW_{II-Gk} \quad (80)$$

A value for parameter W_{II-Gk} can be adopted from the work of Pownceby and others (1999). This value is consistent with the experimental work on olivine-rhombohedral oxide, Fe^{2+} -Mg exchange of Andersen and Lindsley (1979). For the MnTiO_3 - FeTiO_3 join, the EMF measurements of O'Neill and others (1989) provide an estimate for the parameter W_{II-Py} . Values are reported in table 2.

In the absence of experimental constraints, a preliminary estimate for parameter values governing cation-ordering in MgTiO_3 and MnTiO_3 is obtained by assuming that the calibration for FeTiO_3 applies to these endmembers. Similarly, parameters applicable to the MgTiO_3 - Fe_2O_3 and MnTiO_3 - Fe_2O_3 joins are assumed to be identical to those on the FeTiO_3 - Fe_2O_3 join (table 2)³. Interaction parameters for the Fe_2O_3 - Al_2O_3 join are taken from Majzlan and others (2002). Aluminate-titanite interactions are assumed comparable to those on the respective ferrite joins.

There is little hope of refining the majority of model parameters from analysis of the supersystem exchange/redox equilibria, as the amounts of Mg, Mn and Al in the rhombohedral phase are small; compositions of the oxides are far removed from the operative portion of composition space where these parameters exhibit their greatest effect on the geometry of the Gibbs surface. However, two adjustable parameters, $W_{(II-Gk)^T}$ and $W_{(II-Py)^T}$ are operative, because they control directly the effect of Mg and Mn respectively on the degree of cation-order, and hence the second order phase transition and location of the miscibility gap in the supersystem.

In order to analyze exchange and redox equilibria in the supersystem, the derivative $\frac{\partial \bar{G}}{\partial X}$ and μ_{Hm} must be obtained from equation (78). These expressions are derived in the Appendix and are given by equations (133) and (134) respectively. In utilizing these expressions, the equilibrium ordering state is calculated by simultaneous solution of equations (125), (126) and (127). In addition to the supersystem rhombohedral oxide model, evaluation of exchange and redox energies for two oxide pairs necessitates estimation of the activity of Fe_3O_4 and Fe_2TiO_4 in supersystem spinels. The model of Sack and Ghiorso (1991a) is adopted and the effect of Mn is proxied by Mg. The justification of this assumption is based on the observation (Lucchesi and others, 1997) that Mn^{2+} exhibits a strong tetrahedral site preference in spinels, more similar to that of Mg^{2+} than Fe^{2+} . Implicit in our analysis is the assumption that Mn enters spinel as a divalent cation under the T and f_{O_2} conditions of interest.

A model calibration for the supersystem is reported in table 2, with those parameters estimated from the data labeled as “Two-oxide equilibria.” The model is based on the complete supersystem data set of Evans and others (2006), the “simple” system experiments of Lattard and others (2005), the supersystem two-oxide equilibria determined by Scaillet and Evans (1999; with revised chemical analyses), and selected naturally occurring two-oxide pairs from Mt. Pinatubo⁴ and the Bishop Tuff⁵. We

³ Intermediate compositions along the MgTiO_3 - Fe_2O_3 binary join may exhibit a greater degree of cation-order than corresponding compositions along the FeTiO_3 - Fe_2O_3 join (H. St. C. O'Neill, personal communication), in violation of our simplifying assumption. As we are concerned mainly with activity composition relations of FeTiO_3 in rhombohedral oxides containing less than 20 mole % MgTiO_3 , errors introduced by this assumption are ameliorated by calibrating values for Fe^{2+} -Mg energetic parameters between ordered and disordered titanate endmembers (for example, $W_{(II-Gk)^T}$) from exchange/redox data among supersystem oxides. The net result of this calibration is that the order-disorder energetics for compositions close to the FeTiO_3 - Fe_2O_3 binary are correctly accommodated by the thermodynamic model regardless of our assumption regarding ordering behavior on the MgTiO_3 - Fe_2O_3 join.

⁴ Sample PH13D (average composition from Dacite XP, Pallister and others, 1996) assumed to be at 730°C, sample from dacite reported by Rutherford and Devine (1996) assumed to be at 720°C, sample UK29AY (Dacite WP, Hattori, 1996) assumed to be at 750°C.

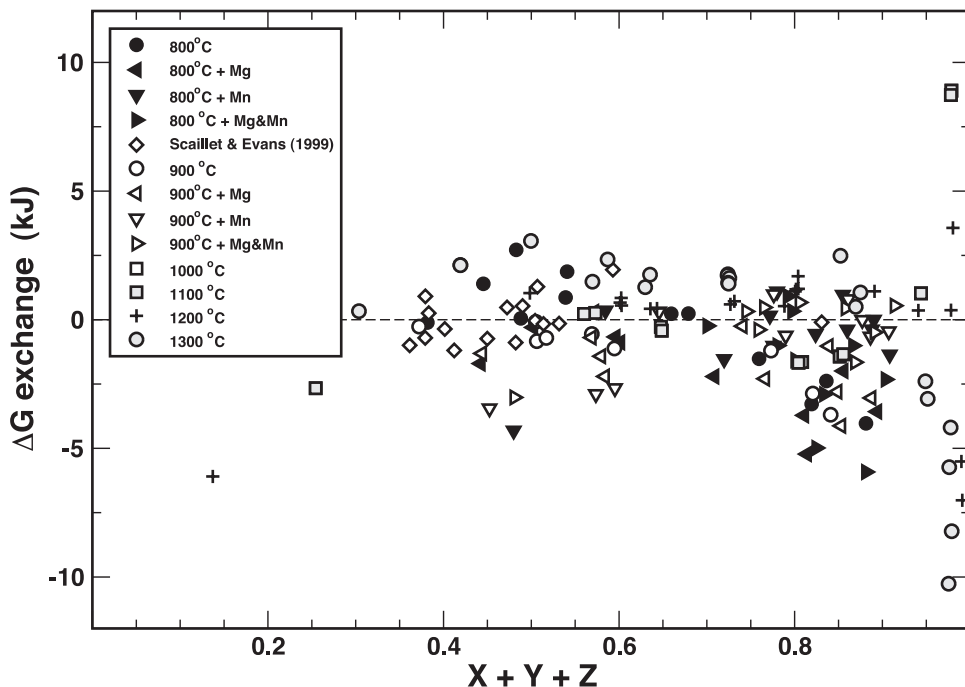


Fig. 12. Gibbs free energy of the Fe-Ti exchange (A) and redox (B) reactions between coexisting rhombohedral and spinel oxides as defined in equations (51) and (52), respectively. Supersystem calibration of model parameters reported in table 2 is used for this analysis. All experiments performed at 800° and 900° C are taken from Evans and others (2006) and those at higher temperatures are from Lattard and others (2005).

chose to include four natural two-oxide pairs (for $\text{Fe}^{+2}\text{Ti}[\text{Fe}^{3+}]_2$ exchange temperature constraints only) for two reasons: (1) model calibrations without these constraints generated temperature estimates for equilibration of naturally occurring two oxide pairs that routinely fell below the solidus, and (2) elemental ratio concentrations of “minor” constituents in naturally occurring oxides, in particular Mg/Al ratios in spinels, are not represented in the experimental dataset. The second is arguably the more compelling reason for inclusion of the additional constraints. In the calibration of supersystem model parameters, the natural pairs were weighted to optimize temperature-recovery; inclusion of the four natural two-oxide pairs had the greatest impact on recovery of the temperatures from the Mg-doped synthetic rhyolite experiments of Evans and others (2006). Importantly, the quality of the fitting to the Mn– and Mg+Mn-doped experiments was largely uncompromised.

Recovery of exchange [eq. (51)] and redox [eq. (52)] energies for the supersystem calibration are displayed in figure 12. Back-recovery of experimental intensive variables is demonstrated in figure 13. The fit is comparable to that in the “simple” system (figs. 9 and 10) but with better overall agreement at 900°C. Recovery of oxidation state is good and errors of model estimates correlate as before with ilmenite-content (and low ΔNNO) of the rhombohedral phase (fig. 13A).

Model temperature estimates from the supersystem fit are subject to enormous uncertainties (fig. 13B). To understand this situation better, it is useful to recast the

⁵ Sample BT111, Hildreth (ms, 1977) assumed to be at 700°C.

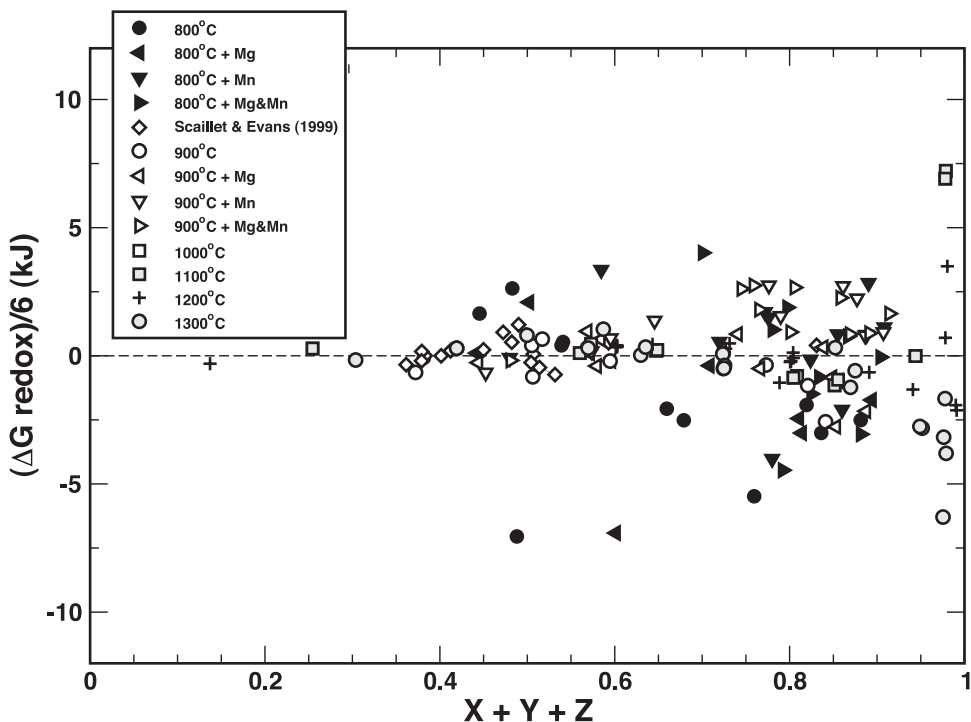


Fig. 12 (continued).

analysis of the two-oxide data graphically in the form of a Roozeboom diagram, plotting mole fraction of Fe_2TiO_4 in spinel versus mole fraction of FeTiO_3 in the rhombohedral phase. The Roozeboom diagram plotted in figure 14 reveals a number of interesting features. The widely spaced equilibrium-coexistence isotherms in the upper part of the diagram define a composition-temperature region where the rhombohedral phase is cation-ordered. The dotted line corresponds to the path of the symmetry breaking phase transition. Within the high-symmetry phase, the isotherms are closely spaced. Note how a typical compositional uncertainty of about two-mole percent translates into a temperature uncertainty of about 50°C in the disordered region. At low or high FeTiO_3 or Fe_2TiO_4 mole fractions, the same compositional uncertainty translates into an even larger uncertainty in temperature, because the isotherms become more closely spaced. By contrast, within the ordered region, model temperature is much less sensitive to composition, but if the phase is grown under conditions that place it slightly above or within the T - X field of the miscibility gap, then the ability to tightly define an equilibrium composition of the rhombohedral phase is diminished because the chemical potential is a very weak function of composition under these conditions and a range of rhombohedral oxide compositions can coexist with a given spinel in an approximate state of equilibrium. Another way to look at the effect of miscibility gap is to note the near vertical nature of the isotherms right around $X_n \sim .6$ to $\sim .7$. The limbs of the miscibility gap are defined along any given isotherm by two rhombohedral oxide compositions that coexist with the same spinel. Thus the break in slope of the isotherms at the symmetry-breaking phase transition curve defines one limb of the miscibility gap. Compositions that plot close to this break in slope are very sensitive to model calibration. It should be kept in mind that the

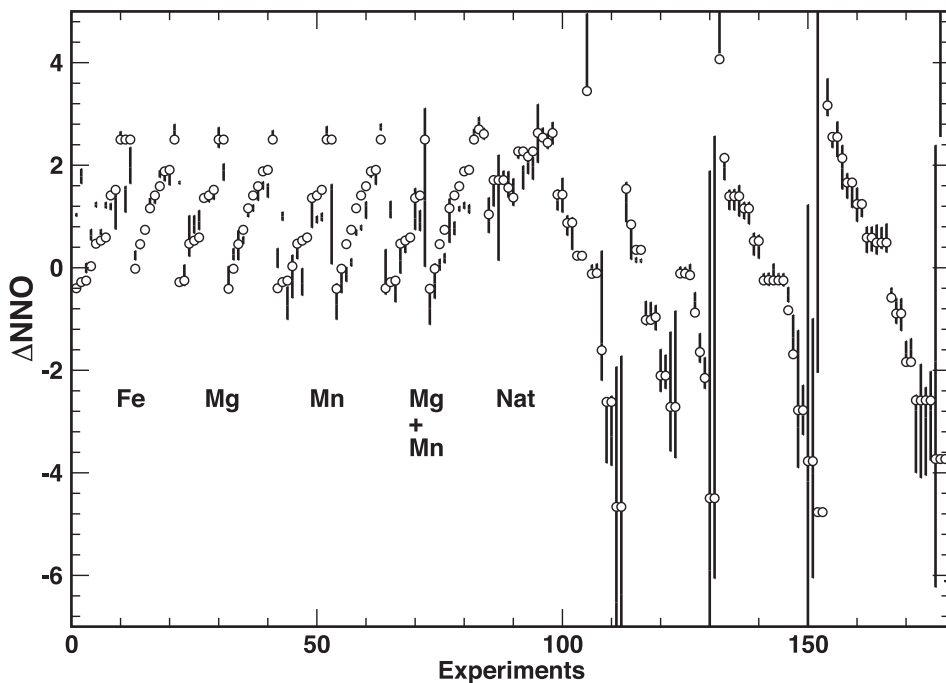


Fig. 13. Recovery of oxidation state (A) and temperature (B) corresponding to the model fit displayed in figure 12. See legend of figure 10. The sets of 800° and 900° C experiments labeled Fe, Mg, Mn, and Mg+Mn are from Evans and others (2006) and refer to nominal Fe-Ti-O oxides, Fe-Mg-Al-Ti-O oxides, Fe-Mn-Al-Ti-O oxides, and Fe-Mg-Mn-Al-Ti-O oxides, respectively. The group labeled "Nat" are supersystem oxides from Scaillet and Evans (1999). The high-temperature pairs are from Lattard and others (2005).

composition-temperature path of these slope breaks is defined entirely from the cation-ordering measurements of Harrison and others (2000a) and Harrison and Redfern (2001).

Relative spacing of isotherms plotted in figure 14 reveals that the success of two-oxide exchange equilibria as a geothermometer depends entirely on the composition of the spinel and rhombohedral phase. At oxidation state conditions below that of NNO, coexisting Fe-Ti oxides define a geothermometer of reasonable sensitivity. Other $T-f_{O_2}$ conditions must be evaluated on a case-by-case basis however, and results may very well be problematic.

By contrast, the isopleths of constant oxidation state (plotted relative to the nickel-nickel oxide oxygen buffer in fig. 14) are uniformly spaced except under very reducing conditions. In the high-symmetry T - X region of the Roozeboom plot the ilmenite-content of the rhombohedral phase is an excellent indicator of relative oxidation state. This simple correlation breaks down in the ordered region, but above the miscibility gap the isopleths still depend principally on ilmenite mole fraction. Overall, figure 14 reveals that coexisting Fe-Ti oxides make an excellent oxygen barometer.

Energetic Features of the Model

In the paramagnetic state, the configurational energy of rhombohedral oxide solid solutions is dominated by the effects of cation ordering. The reduction in entropy

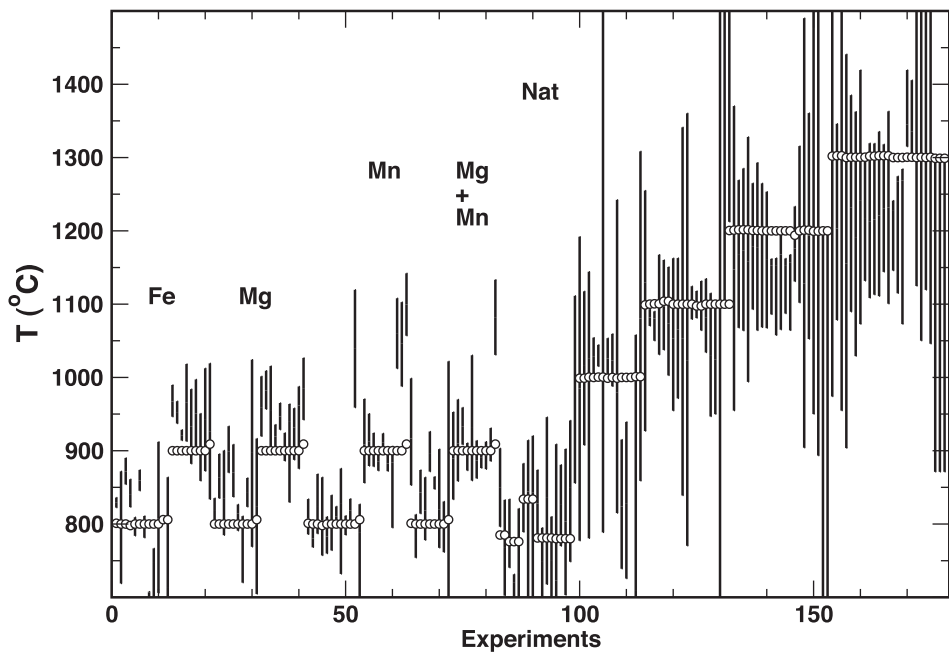


Fig. 13 (continued).

associated with the development of cation order raises the configurational Gibbs free energy and simultaneously increases the enthalpy of mixing. Cation ordering induces phase separation, and gives rise to highly non-linear activity-composition relations in the series. In this section we explore some of these energetic consequences, starting first with an examination of experimental data on the enthalpy of solution in the system $\text{FeTiO}_3\text{-Fe}_2\text{O}_3$.

Enthalpy of solution.—Brown and Navrotsky (1994) report drop solution calorimetry measurements on ilmenite-hematite solid solutions. Their data are plotted in figure 15. Samples were synthesized at 1300°C under controlled atmosphere conditions and annealed at temperatures between 700° and 1300°C for an unspecified interval before being dropped into the lead borate flux of the calorimeter at 1057 K. Care was taken to prevent oxidation during annealing and dissolution. It is noteworthy that the three measurements clustered at $X \sim 0.6$ represent samples annealed at 725°, 800° and 1300° C and that those at $X \sim 0.7$ correspond to pre-drop annealing temperatures of 750°, 1000°, and 1300° C and that neither cluster demonstrates an effect of quenching temperature on the enthalpy of dissolution. Brown and Navrotsky (1994) attribute this to the development of extensive SRO. The model curves plotted in the figure are calculated from the formal definition of the enthalpy of solution

$$\bar{H} = \bar{G} + T\bar{S} \quad (81)$$

where the molar entropy of solution

$$\bar{S} = - \left. \frac{\partial \bar{G}}{\partial T} \right|_{eq,X,P} \quad (82)$$

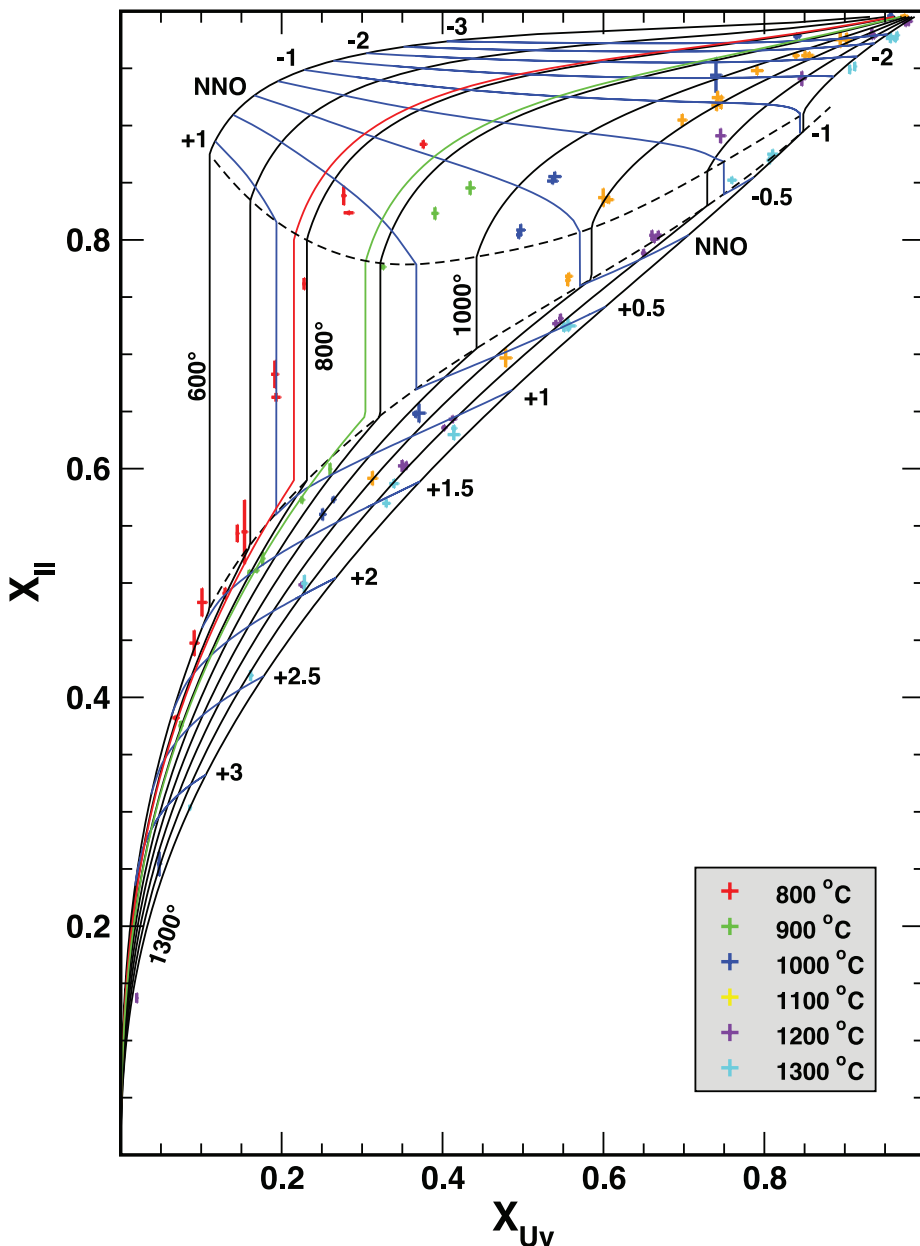


Fig. 14. Roozeboom plot showing isotherms and isopleths of relative oxidation state for two-oxide equilibria in the system Fe-Ti-O. The supersystem calibration is used to model the curves. Isotherms are labeled in $^{\circ}\text{C}$. Isopleths (blue) are labeled in displacements of $\log_{10} f_{\text{O}_2}$ units from the nickel-nickel oxide buffer (NNO). The dashed curves enclose the region of the miscibility gap in the rhombohedral series; the ilmenite-poor segment of the gap limb falls very close to the critical ordering curve for the series. Phase equilibrium data from Evans and others (2006) and Lattard and others (2005) are plotted. Symbols indicate $\pm 2\sigma$ reported compositional uncertainty. Colored isotherms at 800° and 900° C indicate the displacement calculated for addition of Al to spinel (as FeAl_2O_4) in amounts comparable to the nominal “Fe-Ti-O” experiments reported by Evans and others (2006). Note that the isotherms and isopleths are vertical within the miscibility gap.

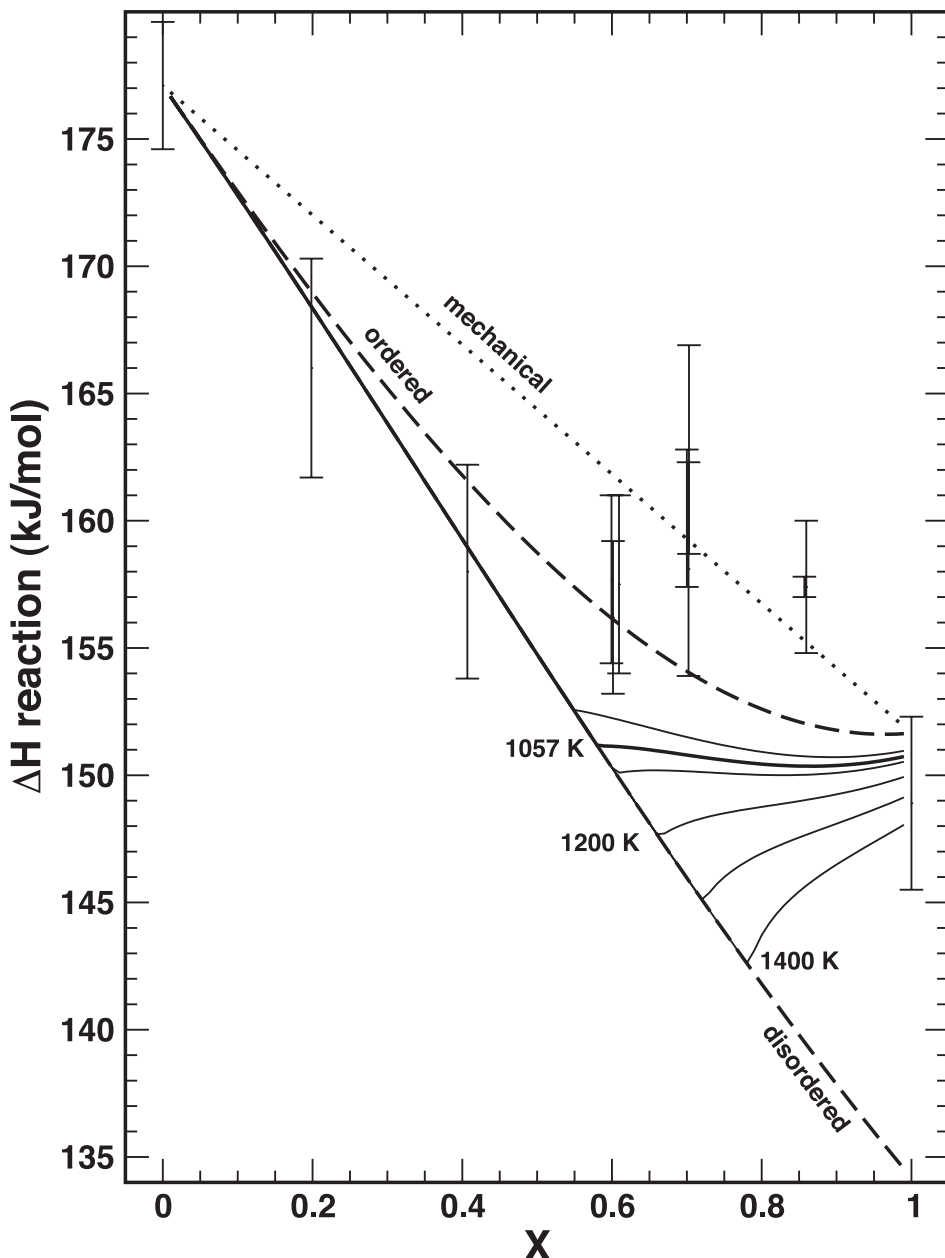


Fig. 15. Enthalpy of reaction as reported from the drop solution calorimetry measurements of Brown and Navrotsky (1994). Values (with $\pm 2\sigma$ brackets) plotted correspond to heat released when pre-annealed samples are dissolved in molten lead borate at 1057 K. Curves are calculated from the supersystem model with intercepts adopted from the calorimetry measurements. The *dashed curves* model the fully cation-ordered (upper) and cation-disordered (lower) phases. The *solid curves* give the modeled heat of reaction for an equilibrium ordered structure at the temperatures: 1000, 1057 (*heavy solid curve*), 1100, 1200, 1300, and 1400 K.

is defined at a given T and X in an *equilibrium state of cation-order (eq)*. The latter is obtained from the variation in \bar{G}

$$d\bar{G} = \frac{\partial \bar{G}}{\partial X} dX + \frac{\partial \bar{G}}{\partial s} ds + \frac{\partial \bar{G}}{\partial T} dT + \frac{\partial \bar{G}}{\partial P} dP \quad (83)$$

which results in

$$\left. \frac{\partial \bar{G}}{\partial T} \right|_{eq,X,P} = \frac{\partial \bar{G}}{\partial T} \quad (84)$$

because $\frac{\partial \bar{G}}{\partial s}$ is zero in a state of equilibrium cation-order. Consequently equation (81) becomes,

$$\bar{H} = \bar{G} - T \frac{\partial \bar{G}}{\partial T} \quad (85)$$

and from equation (78) the enthalpy of solution in the $\text{FeTiO}_3\text{-Fe}_2\text{O}_3$ binary is

$$\begin{aligned} \bar{H} = & (1 - X)\bar{h}_{Hm}^o + X\bar{h}_{Il}^o + (1 - X)X[W_{Hm-II} + (1 - X - X)\Delta W_{Hm-II}] \\ & + (X^2 - s^2) \left[\frac{W_{Il-II}}{4} + (1 - X) \left(\frac{\Delta W_{Hm-II}}{2} + \frac{W_{Hm-II-Il}}{4} \right) \right] + (X^2 - s^2)s^2 \frac{\Delta^2 W_{Il-II}}{4} \end{aligned} \quad (86)$$

The dotted line in figure 15 corresponds to the mechanical mixing of *fully cation ordered* endmembers; pivot points are taken from the data of Brown and Navrotsky (1994), where the measured intercept value for FeTiO_3 is corrected for the modeled state of order ($s = 0.93$) and its associated enthalpy of disorder ($\Delta\bar{H}^{dis} = 2.756 \text{ kJ/mol}$) at the annealing temperature of 1338 K. The heavy dashed curves correspond to the modeled enthalpy in the fully ordered ($s = X$) and fully disordered ($s = 0$) states, as labeled. The solid curves are calculated in an equilibrium state of order and are plotted for the indicated temperatures. The entire collection of curves can be displaced along the ordinate according to uncertainties associated with the location of the intercepts, which at the ilmenite end of the diagram is on the order of $\pm 3.5 \text{ kJ/mol}$ (Brown and Navrotsky, 1994). The measurements at $X < 0.5$ are consistent with the model calibrated here. The cluster of points at ~ 0.6 are consistent with the model if the samples are taken to be fully ordered—either due to LRO or SRO. Within the uncertainty of the intercept location, measurements at $X \sim 0.7$ and ~ 0.85 are also consistent with the modeled enthalpy of the fully ordered state. Brown and Navrotsky (1994) interpret the measurements at high mole fraction of ilmenite to imply a *negative* enthalpy of mixing, but this is certainly not borne out by the model calibration, where all enthalpies of mixing are positive in any ordering state across the join. However, there is a possibility for interpreting the measurements in a self-consistent way that yields positive enthalpies of mixing if the ilmenite intercept for mechanical mixing for those points with $X < 0.9$ is different and about 10 kJ/mol more positive than that measured for pure ilmenite. The difference in intercepts might arise if there is an enthalpy associated with the first order phase transition at X_C . Our analysis of the ordering data did not identify the need for such an enthalpy, but perhaps the drop-calorimetry measurements of Brown and Navrotsky (1994) offer some justification for an interpretation along these lines.

Entropy and Gibbs free energy of mixing; activity-composition relations.—The modeled molar entropy of mixing is plotted in figure 16. The solid lines correspond to isotherms calculated for an equilibrium state of cation LRO. The dashed curve is a

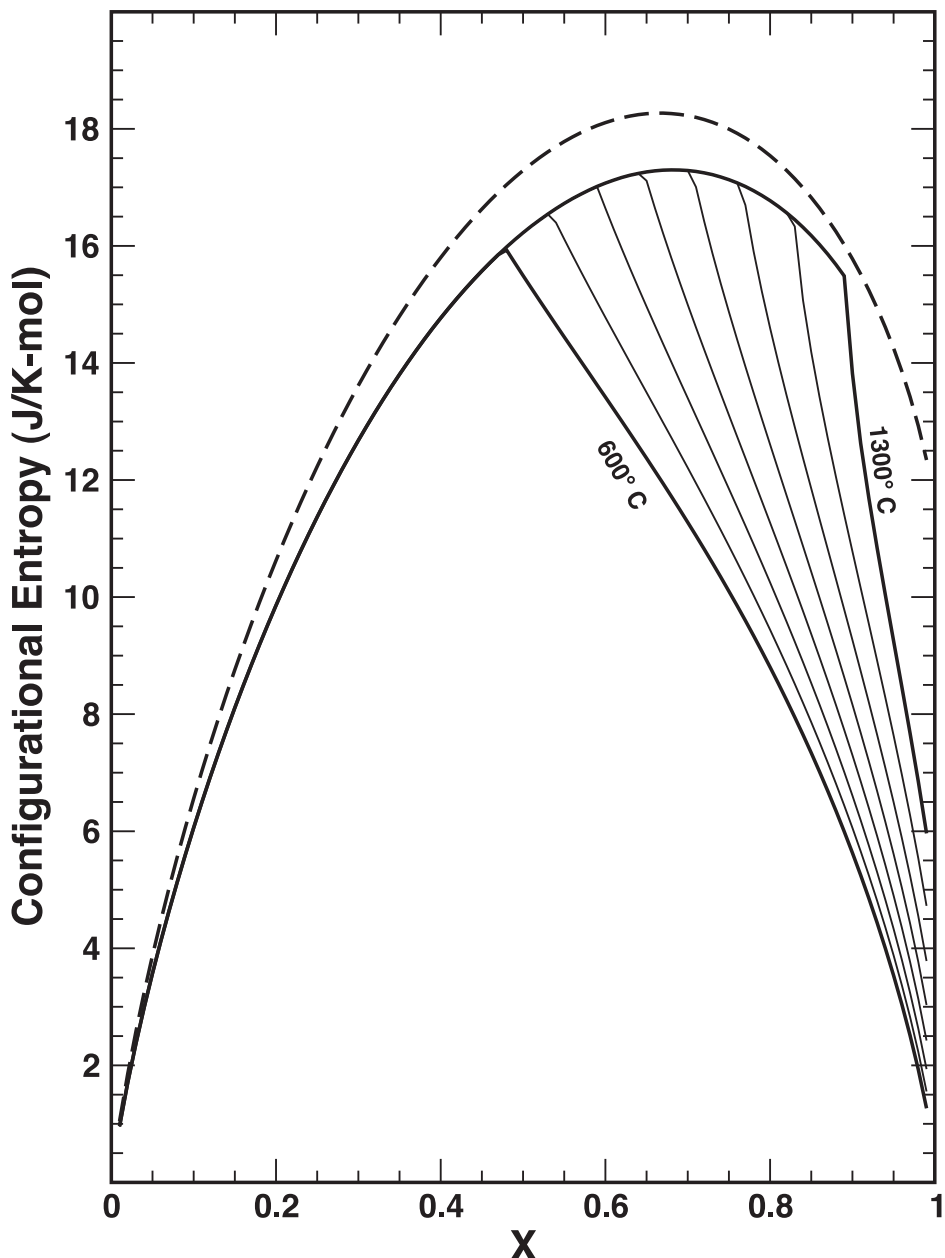


Fig. 16. Modeled configurational entropy—including the effects of SRO—in the system Fe₂O₃-FeTiO₃. Isotherms are spaced at 100°C. The dashed curve refers to the ideal site-mixing configurational entropy. Note that this is not a plot of the entropy of mixing as the standard state contribution of the configurational entropy for pure ilmenite has not been subtracted to zero the intercept at X = 1.

reference corresponding to ideal random mixing. The offset between the random mixing curve and the envelope of isotherms reflects the SRO reduction in entropy, which is about 7 percent in the supersystem model.

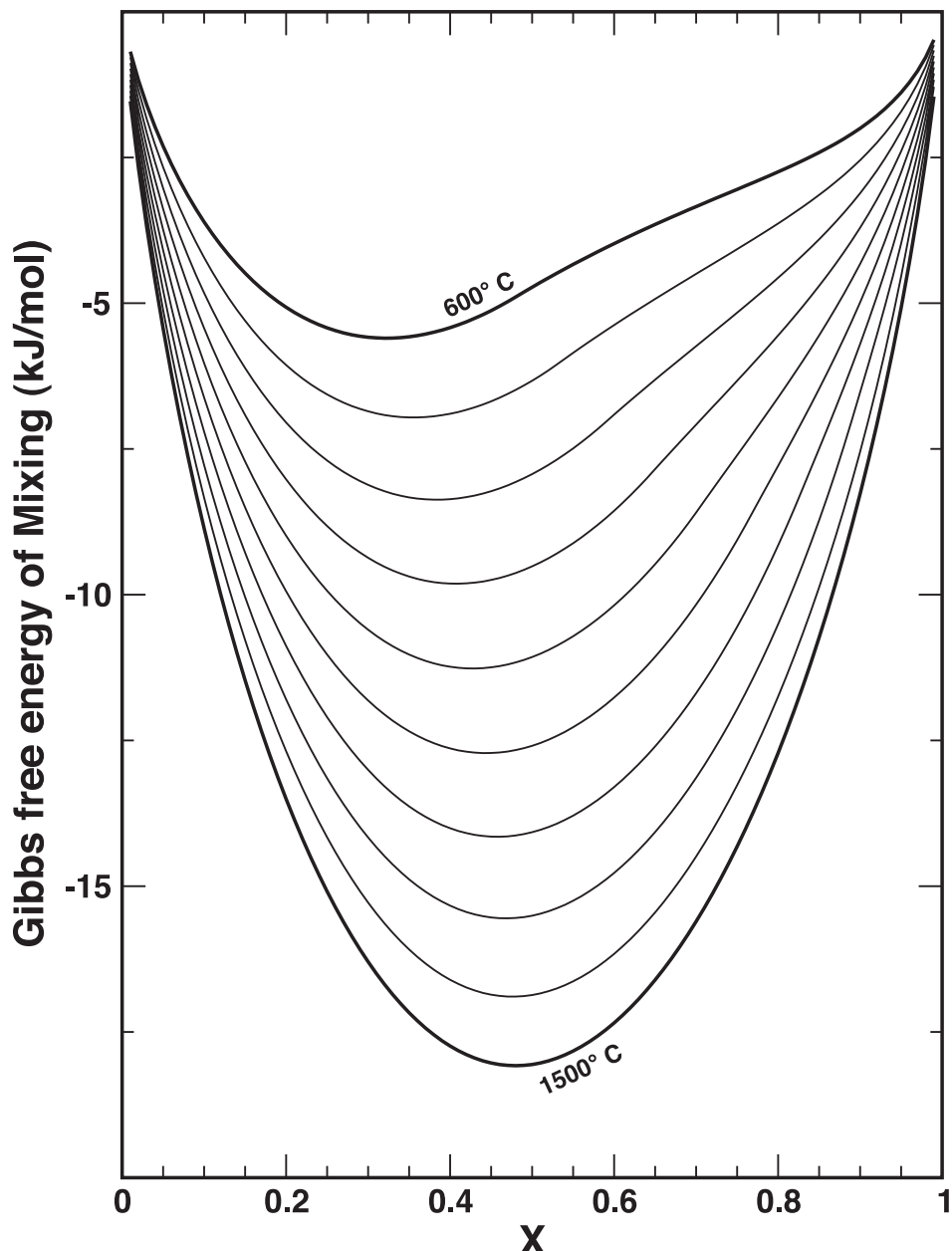


Fig. 17. Modeled Gibbs free energy of mixing in the system Fe_2O_3 - FeTiO_3 . Isotherms are spaced at 100°C.

The molar Gibbs free energy of mixing is plotted in figure 17. The most interesting feature of the diagram is the undulation in the low-temperature isotherms visible at $X > 0.5$. These undulations are the energetic expression of the miscibility gap. This somewhat subtle feature is easier to appreciate if a quantity is plotted that depends on the compositional derivative of the Gibbs energy, like the chemical potential or

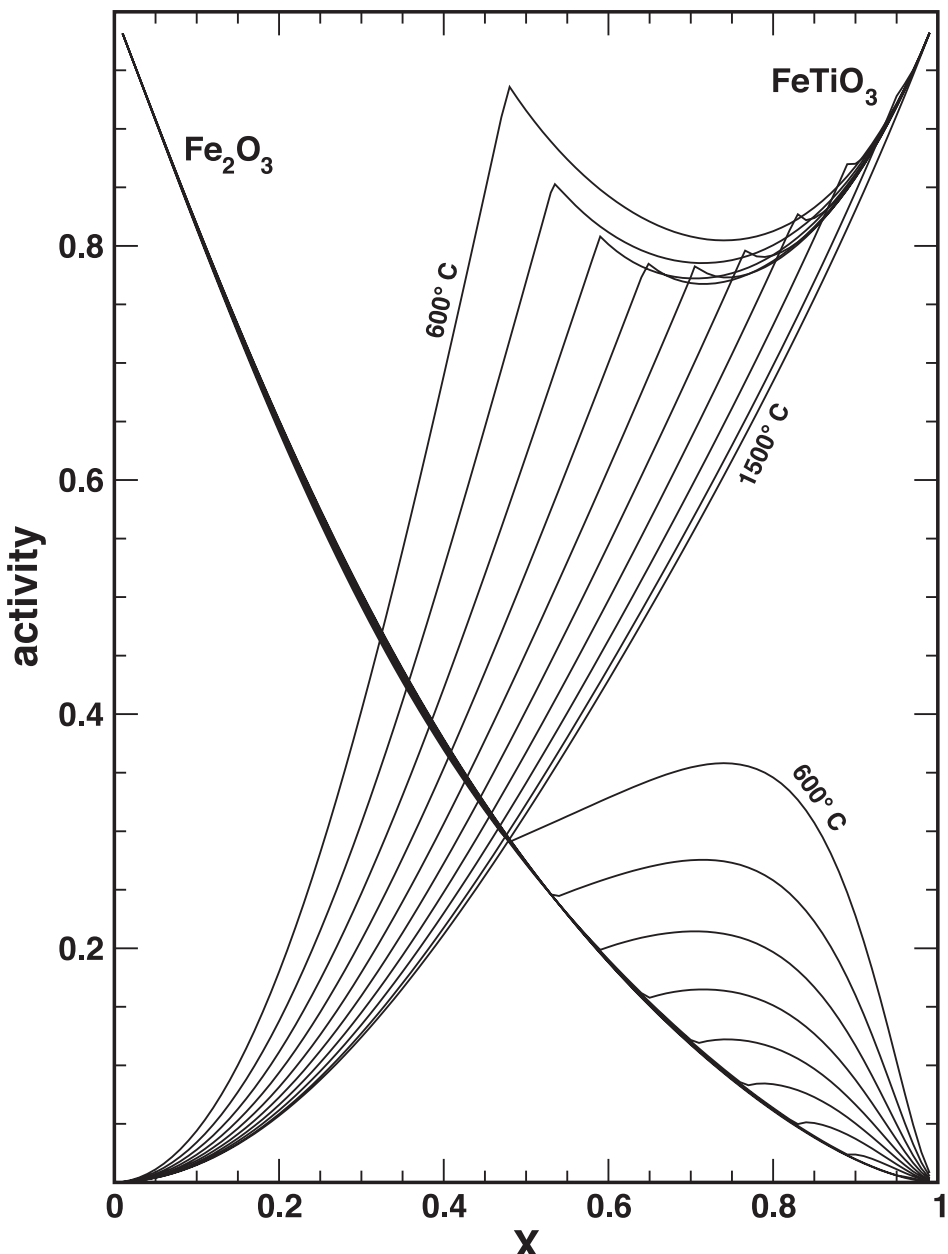


Fig. 18. Modeled activity-composition relations in the system Fe_2O_3 - FeTiO_3 . Isotherms are spaced at 100°C.

activity of either endmember. In figure 18, calculated activity composition relations are displayed. In this diagram distinct compositions that have identical activities of FeTiO_3 and Fe_2O_3 along any given isotherm can be identified; these are binoidal compositions that delineate the limbs of the miscibility gap. As mentioned above, in the vicinity of the miscibility gap the activity of either endmember is a weak function of composition,

which implies that the energetic response to compositional variation, that is, the effect of compositional variation on phase equilibria, geothermometry, *et cetera*, will be necessarily weak in this region. This weak relation between energy and composition is a consequence of the existence of the miscibility gap rather than an artifact of the model calibrated here. It is by perverse coincidence that natural occurrences of the Fe-Ti rhombohedral oxides found with coexisting spinel in volcanic dacites and rhyolites happen to have compositions and formation temperatures that generate a subtle dependence of activity on composition. Consequently, application of a thermodynamic model for this series to two-oxide geothermometry demands a level of model accuracy that exceeds typical requirements.

It is instructive to examine the effects of impurities on the activity-composition relations displayed in figure 18. To illustrate, the consequences of adding MgTiO_3 are examined in figure 19, where activity-composition relations at 700°, 800°, and 900° C along an $\text{MgTiO}_3/\text{FeTiO}_3$ pseudobinary from Fe_2O_3 are plotted and compared with corresponding curves from figure 18. The effect of the addition of MnTiO_3 would be qualitatively similar. Two features are apparent from the comparison. First, the onset of ordering has shifted to lower mole fractions of $\text{FeTiO}_3 + \text{MgTiO}_3$, which is evident from the translation of the activity-composition cusp to lower $X + Y$ on comparable isotherms. The implication is that the critical ordering curve has shifted to higher temperatures along the pseudobinary and that the addition of MgTiO_3 enhances the state of Ti^{4+} order. From a model perspective, this feature is a consequence of the large positive value for the parameter $W_{(H-Gk)^T}$, which is extracted during model calibration to reconcile the Mg-doped exchange/redox experiments of Evans and others (2006) and the natural two-oxide pairs with the simple system data. A similar, though less pronounced effect, should be evident with the addition of MnTiO_3 . Intuitively, one might expect the enhanced state of cation-order to widen the miscibility gap, because cation-ordering lowers the configurational entropy. The second important feature apparent from figure 19 demonstrates that this is not the case. The addition of only 10 percent MgTiO_3 (relative to FeTiO_3) eliminates the miscibility gap for the 800° and 900° C isotherms and nearly eliminates that for the 700° C isotherm. Energetically, the principal reason the gap diminishes in extent with the addition of MgTiO_3 is both entropic and enthalpic; the additional entropy derived from mixing of Fe^{2+} and Mg^{2+} counterbalances the reduction in entropy associated with Ti^{4+} ordering, but ordering also diminishes the enthalpy of mixing. This can be seen from the inset of figure 19, where enthalpy of mixing is plotted at 800° C for both the simple binary and for the pseudobinary composition. The enthalpy of mixing is largely dominated by the positive enthalpy of disorder, which is maximal at *pure ilmenite* (for example, fig. 15). Along any isotherm, the maximum in the enthalpy of mixing therefore occurs at the composition of the critical ordering curve. The closer that composition is to pure ilmenite, the larger the enthalpy of mixing at that composition. As the addition of MgTiO_3 shifts the critical ordering composition to lower ilmenite contents, the enthalpy of mixing is less positive in the pseudobinary than in the binary and consequently, the miscibility gap is diminished because the enthalpic drive for unmixing is reduced. As naturally occurring rhombohedral oxides have appreciable MgTiO_3 and MnTiO_3 contents, the energetic/topologic complications associated with the miscibility gap in the binary are expected to be of less consequence for natural materials.

Miscibility gap, spinodes, and other features of the $\text{FeTiO}_3\text{-Fe}_2\text{O}_3$ phase diagram.—Model parameter values for the supersystem calibration can be used to calculate a phase diagram for the $\text{FeTiO}_3\text{-Fe}_2\text{O}_3$ binary. This diagram is plotted in figure 20 and should be compared to the permissible set of preliminary phase diagrams plotted in figure 6. The supersystem calibration was made to accommodate the cation-ordering analysis

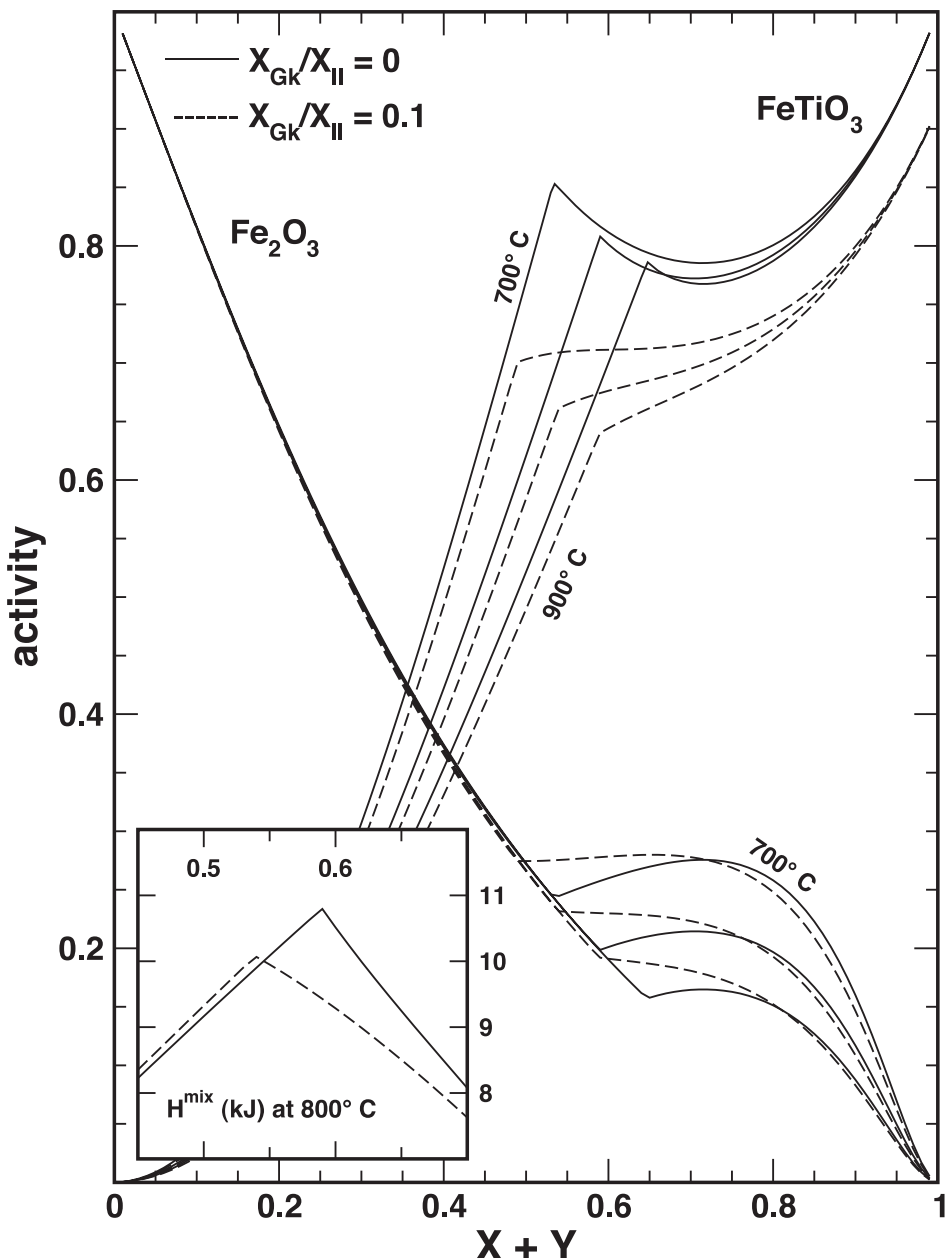


Fig. 19. Modeled activity-composition relations in the system Fe_2O_3 - FeTiO_3 (solid curves) and the system Fe_2O_3 - FeTiO_3 - MgTiO_3 . Isotherms are spaced at 100° C. The inset shows the enthalpy of mixing for both systems at 800° C. Units are in kJ/mol.

but was not constrained to accommodate the miscibility gap reversal experiments. Doing so in the manner of figure 6 would have prevented an adequate fit to the exchange/redox experiments. This is the case with or without the supersystem (*sensu stricto*) experiments, and exposes a fundamental inconsistency among the *binary* Fe-Ti

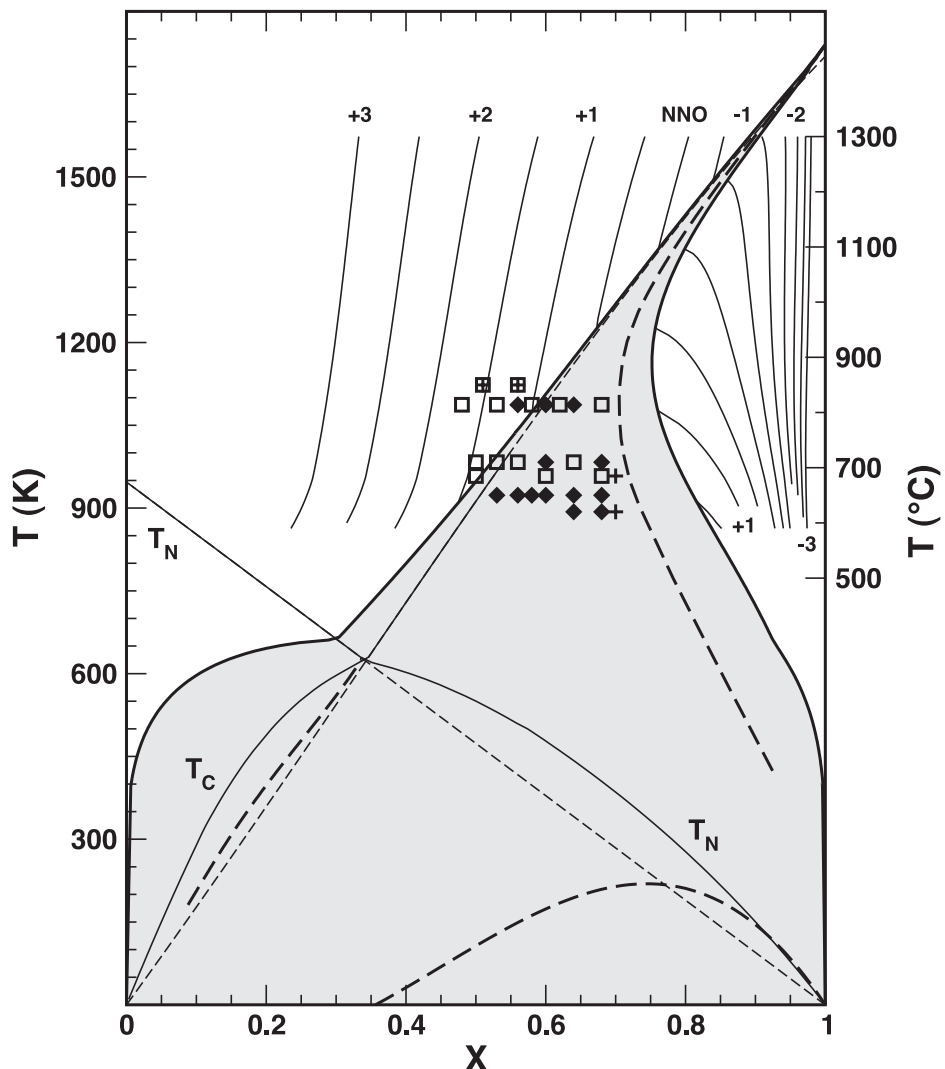


Fig. 20. Phase diagram for the system Fe_2O_3 - FeTiO_3 calculated from the supersystem calibration (table 2). Notation follows that of figure 6. The heavy dashed lines are spinodal curves. Magnetic effects on the miscibility gap and critical curves are estimated using the methods of Ghiorso (1997). Relative oxygen fugacity isopleths for two oxide equilibria are replotted from figure 14 and are labeled as previously described.

oxide exchange/redox experiments, the miscibility gap reversal experiments, and the model formulation proposed here. In the context of the supersystem calibration, the miscibility gap reversal constraints are more consistent with the location of the spinode (the heavy dashed curves in the figure) rather than the binode limb. The spinode is calculated by finding the locus of T - X pairs that zero equation (146). Note that the spinode exhibits complex behavior in this system, which results from both cation and magnetic ordering. In this context it is important to understand that the phase diagram displayed in figure 20 is actually an equilibrium cation- and magnetically-ordered “pseudosection” through composition-ordering space. Therefore the spi-

node, which, even if magnetic phenomena are ignored, is properly a manifold that defines a two-dimensional hypersurface in composition-ordering space, and intersects the equilibrium pseudosection only along the T - X cuts identified in the figure. Where the spinode terminates (at low T) it simply passes out of the equilibrium pseudosection. In alternate phase diagrams (for example, fig. 6B) the hematite-rich limb of the spinode terminates at the apex of a cone drawn up along the magnetic critical curve (T_N). In figure 20, the spinode terminates to the ilmenite-side of the intersection of the miscibility gap and the magnetic critical curve; no “magnetic cone” feature is predicted to form with the supersystem model calibration. The ilmenite-rich spinodal (at high T) terminates at pure- FeTiO_3 , and the miscibility gap is continuous throughout this interval.

Also shown in figure 20 are isopleths plotted at various relative oxidation states showing the T - X curves for coexistence of binary Fe-Ti rhombohedral and spinel oxides. The plotted curves demonstrate nicely the non-linear dependence and the sensitivity of the two-oxide geothermometer on composition of the rhombohedral phase.

GEOTHERMOMETER/OXYGEN BAROMETER AND APPLICATIONS

In this section we apply the thermodynamic model developed above as a geothermometer and oxygen barometer within a representative suite of silicic volcanic rocks. This exercise will serve two purposes. First, to compare results derived from this model to previous calibrations (Andersen and Lindsley, 1988; Lindsley and others, 1990; Ghiorso and Sack, 1991), and second, to explore the utility of the model as a petrologic tool and where possible test model predictions against phase equilibrium constraints or alternative thermometric estimates.

In order to carry out this exercise we have assembled a database of some 730 analyses of oxide pairs reported in the literature from volcanic rocks that are primarily dacitic and rhyolitic in bulk composition. The database is available as an electronic supplement to this paper⁶ and it contains all of the natural oxide pairs assembled by Ghiorso and Sack (1991, about 350 pairs) as well as selected data from the more recent literature. Analytical data from this database are plotted in figure 21 in terms of the mole fraction of ulvöspinel in the cubic oxide phase and mole fraction of ilmenite in the rhombohedral phase. Bear in mind that these are naturally occurring oxides often containing appreciable MgO , MnO and Al_2O_3 , so direct comparison of the position of plotted points to the calibration curves depicted in figure 14 will only yield qualitative results. Nevertheless, it is clear from comparison of these two figures that if the oxides have compositions that preserve pre-eruptive conditions of thermodynamic equilibrium, then analyses reflect a large range of temperatures and oxidation states. As an assessment of the quality of the analytical data and an indication of whether the tabulated oxide pairs have had their compositions altered by post-eruptive processes, the Mg-Mn exchange equilibrium distribution line of Bacon and Hirschmann (1988) is plotted in figure 22 along with ratios computed from database oxide pairs. Departures from the Bacon-Hirschmann line provide an empirical evaluation of the extent to which the two oxide pairs are out of Mn-Mg exchange equilibrium (see figure legend); oxide pairs from identified localities are excluded from subsequent figures if they plot outside of two standard deviations of the equilibrium line in figure 22. One can assume that if the two oxides are in Mn-Mg exchange equilibrium, then it is more likely that their bulk compositions reflect equilibration under the pre-eruptive T, f_{O_2} conditions. Ten suites of analyses are identified in figures 21 and 22 that represent well known volcanic centers. These suites of oxides largely satisfy the Mg-Mn exchange test and are

⁶ <http://earth.geology.yale.edu/~ajs/SupplementaryData/2008/04GhiorsoDataTable.xls>

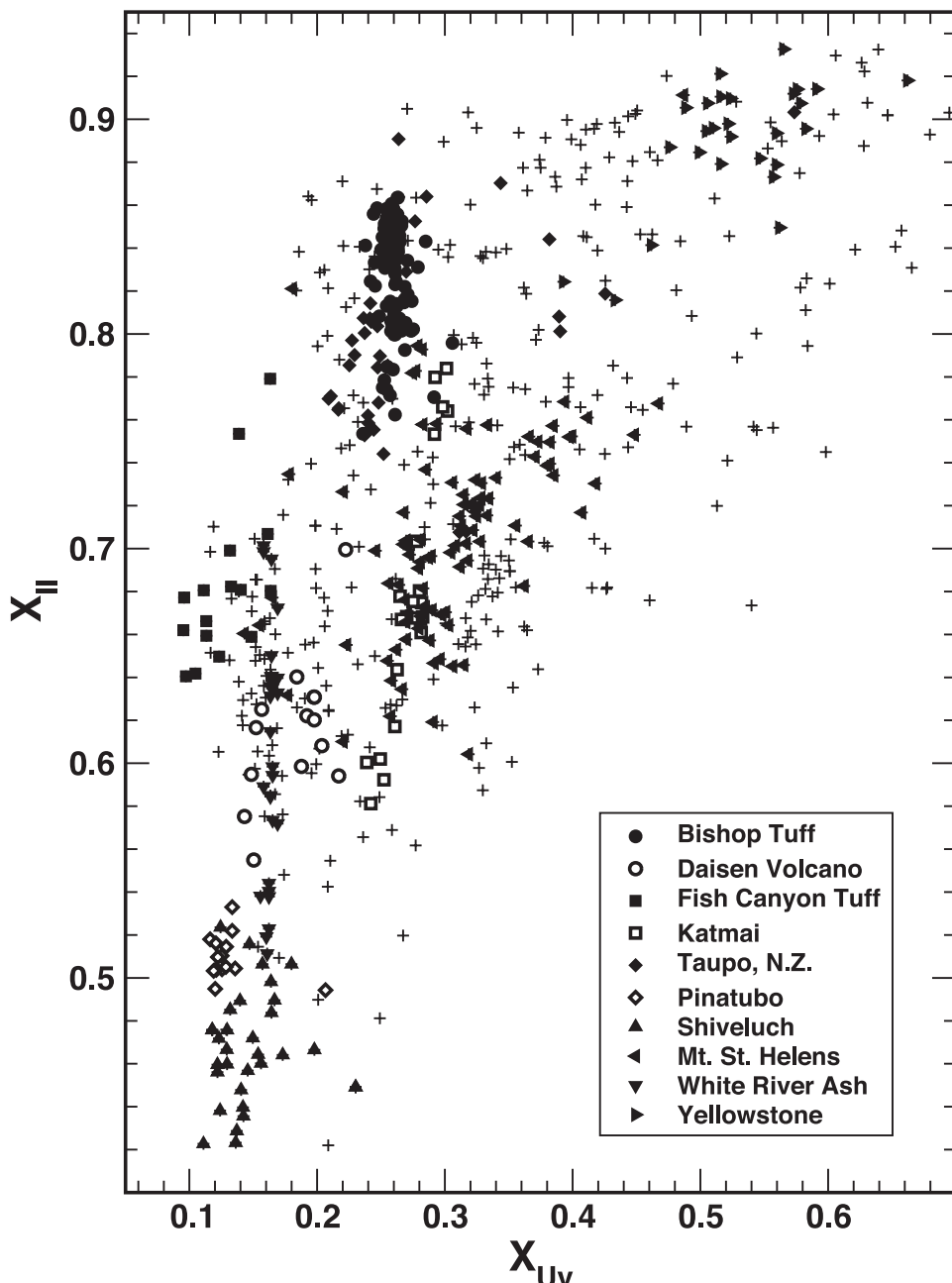


Fig. 21. Compositions of two-oxide pairs from selected dacitic and rhyolitic volcanic rocks (see text). X_{Uv} is the mole fraction of the Fe_2TiO_4 component in spinel calculated according to the component set of Sack and Ghiorso (1991a). X_U is the mole fraction of FeTiO_3 calculated according to the component set chosen for this paper. All non-identified two oxide pairs are plotted as crosses.

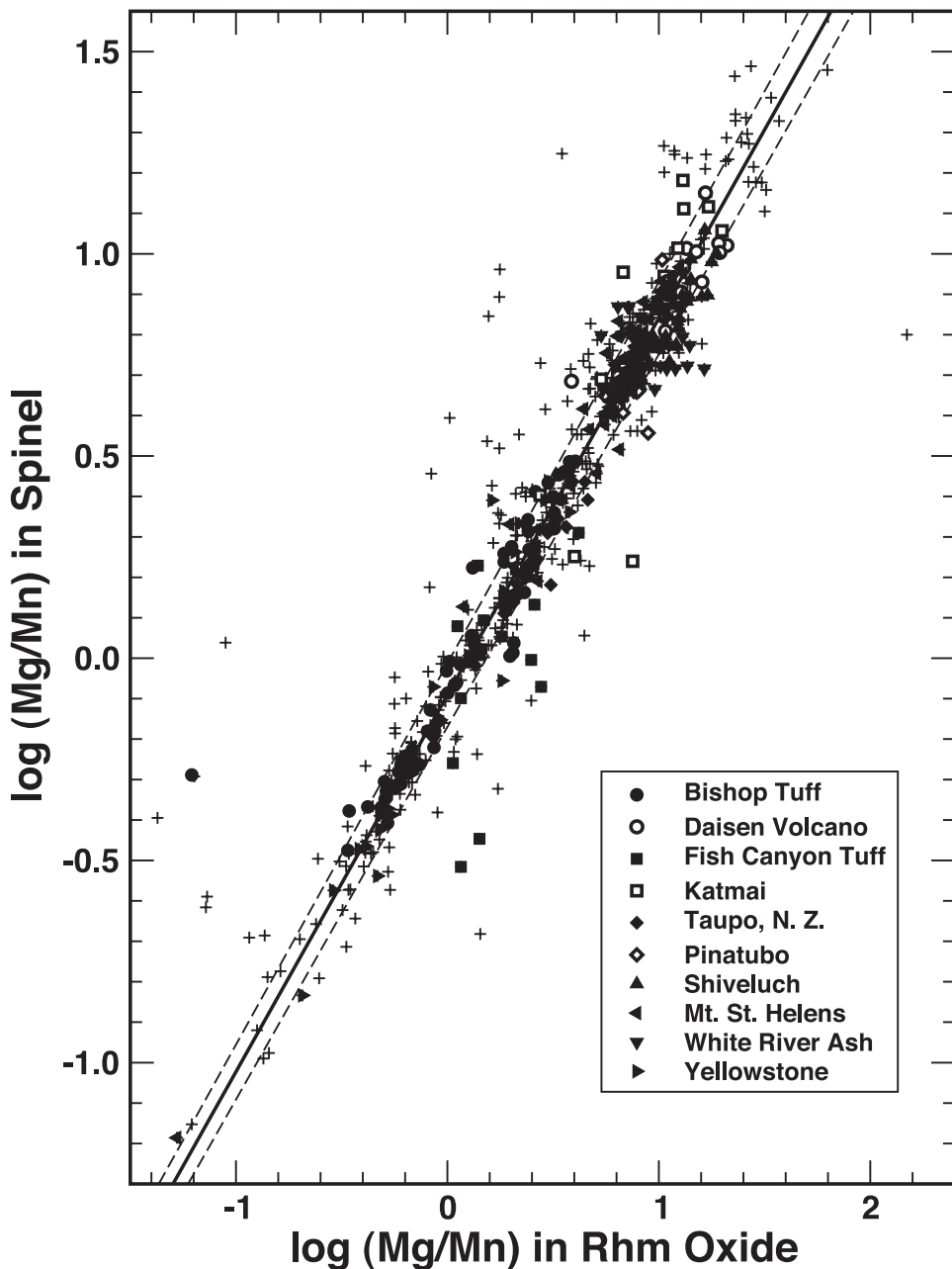


Fig. 22. Mn-Mg exchange test of Bacon and Hirschmann (1988) applied to the dataset of natural oxides displayed in figure 21. Symbols as previously. The lines represent the mean regression line $\pm 2\sigma$ taken from Bacon and Hirschmann (1988).

representative of the spectrum of naturally occurring compositions. We will illustrate these suites repeatedly in the subsequent discussion and figures.

Estimates of temperature and oxidation state (f_{O_2}) are calculated from the database oxide pairs by solving equations (51) and (52) simultaneously with $\mu_n - \mu_{H_m}$

given by equation (133) and μ_{Hm} by equation (134). The “supersystem” model parameters of table 2 are used. Results are plotted in figure 23; f_{O_2} is plotted as $\log_{10} f_{O_2}$ relative to the nickel-nickel oxygen buffer (O’Neill and Pownceby, 1993) on this and all subsequent figures. The $T-f_{O_2}$ estimates derived from the new model differ systematically from the previous formulations of the geothermometer/oxygen barometer. These differences are best examined in figure 24, where we compare $T-f_{O_2}$ estimates from Ghiorso and Sack (1991), Andersen and Lindsley (1988) and Lindsley and others (1990) to the new model. Compared to Ghiorso and Sack (1991) the present estimates of temperature are significantly lower for “oxidized” oxide pairs ($\Delta NNO > 1$), and compared to all three previous formulations the oxidation states of the most oxidized pairs have diminished by as much as one $\log_{10} f_{O_2}$ unit. The reasons for these changes are a reflection of the greatly expanded two-oxide experimental dataset utilized in calibration of the new model; the total number of experimental constraints has increased nearly five-fold compared to that of Ghiorso and Sack (1991), from 57 to 267. Importantly, the new calibration dataset includes experiments at both high temperature and high ΔNNO that were unavailable for previous calibrations of the geothermometer/oxygen barometer. Consequently, virtually all of the high- ΔNNO estimates derived from previous models represent *extrapolations* whereas the new model is better grounded under these oxidized conditions (for example, fig. 14). The shift to lower temperatures at high ΔNNO demonstrates that the new model will affect most profoundly $T-f_{O_2}$ estimates from oxide pairs in oxidized to moderately oxidized rock suites.

Alternative Internally Consistent Estimates of Temperature

Because the rhombohedral oxide thermodynamic model developed in this paper includes geikielite ($MgTiO_3$) as a component and because we are utilizing this model in conjunction with the multicomponent spinel model of Sack and Ghiorso (1991a, 1991b) for thermometric calculations, we can evaluate whether the oxide pairs in our database reflect a condition of Fe^{+2} -Mg exchange equilibrium. To do so we calculate the Gibbs free energy of the exchange reaction



which is given by

$$\Delta \bar{G}_{FeMg}^{exchange} = (\mu_{FeTiO_3}^{rhm} - \mu_{MgTiO_3}^{rhm}) - (\mu_{FeAl_2O_4}^{spn} - \mu_{MgAl_2O_4}^{spn}) \quad (88)$$

The quantity $\mu_{FeTiO_3}^{rhm} - \mu_{MgTiO_3}^{rhm}$ can be evaluated from equations (128) and (129), and equations for $\mu_{FeAl_2O_4}^{spn} - \mu_{MgAl_2O_4}^{spn}$ are provided by Sack and Ghiorso (1991b). The exchange energy ($\Delta \bar{G}_{FeMg}^{exchange}$) will be zero if the two phases are in Fe^{+2} -Mg exchange equilibrium. Alternatively, a temperature may be extracted that zeroes equation (88) for a given oxide pair, effectively using the oxide pair as an Fe^{+2} -Mg exchange geothermometer. One would hope that temperature estimates obtained from evaluation of Fe^{+2} -Mg exchange would be internally consistent with those obtained from the more traditional thermometric two-oxide $Fe^{+2}Ti-(Fe^{+3})_2$ exchange. A comparison for all of the database oxide pairs is plotted in figure 25.

The results appear somewhat discouraging, but the comparison of thermometric measures shown in figure 25 is not quite as disparate as it seems. If we calculate model estimates of T_{FeTi} and T_{FeMg} for the experimental dataset of Evans and others (2006) for oxide pairs grown at $\sim 800^\circ C$ and $\sim 900^\circ C$ from Mg-doped haplorhyolitic liquids that were utilized as part of the calibration of the model, we obtain T_{FeTi} equals $821 \pm 80^\circ C$ and $936 \pm 66^\circ C$ ($\pm 2\sigma$); for T_{FeMg} we obtain $812 \pm 224^\circ C$ and $881 \pm 368^\circ C$ ($\pm 1\sigma$). These error brackets are plotted in figure 25 at the mean recovery temperatures.

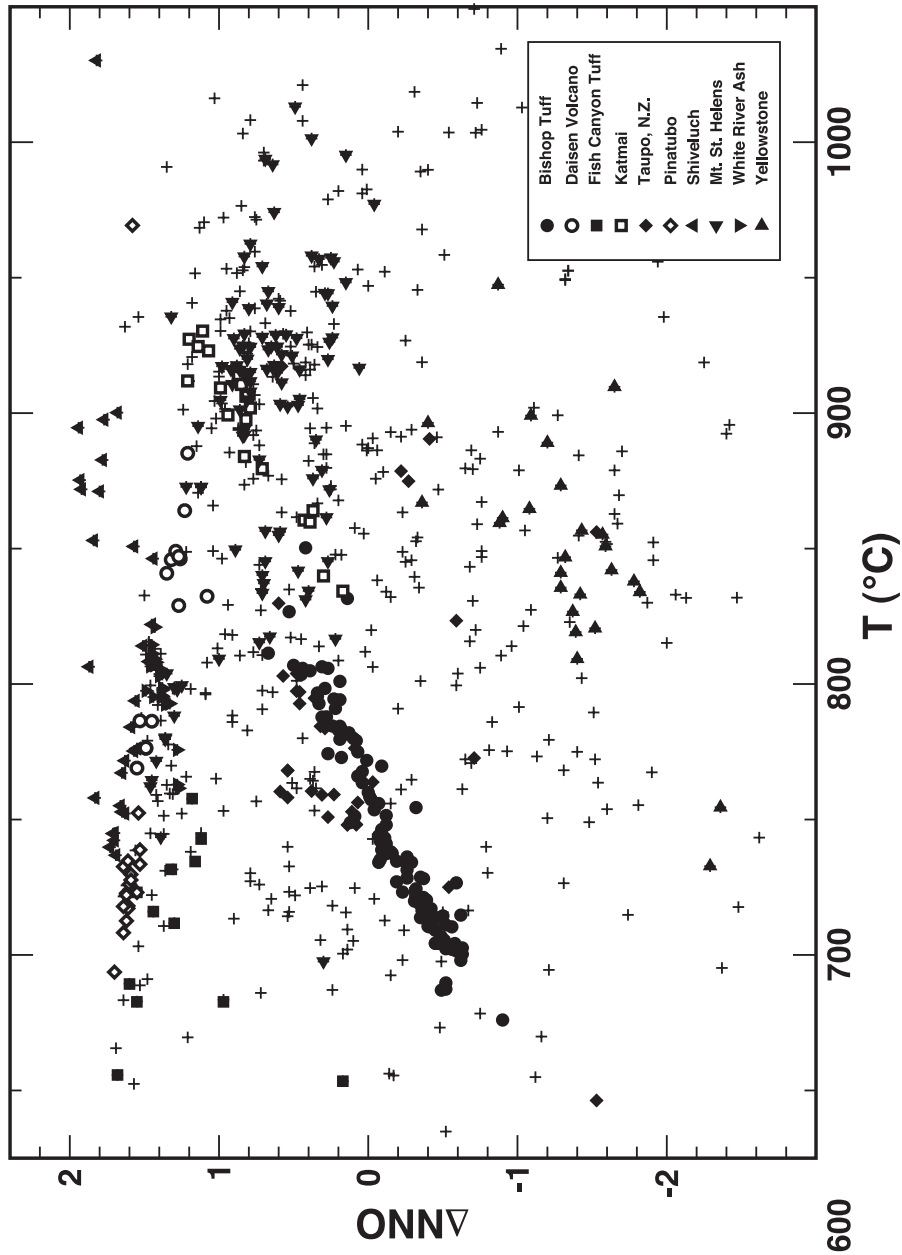


Fig. 23. Temperature (plotted as $^{\circ}\text{C}$) and f_{O_2} (plotted as $\log_{10} f_{\text{O}_2}$, relative to the nickel-nickel oxide oxygen buffer, O'Neill and Pownceby, 1993) calculated for the two-oxide dataset from dacitic and rhyolitic volcanics. Symbols as in figure 21. Data are excluded that fall the Bacon and Hirschmann (1988) test at the 2σ level.

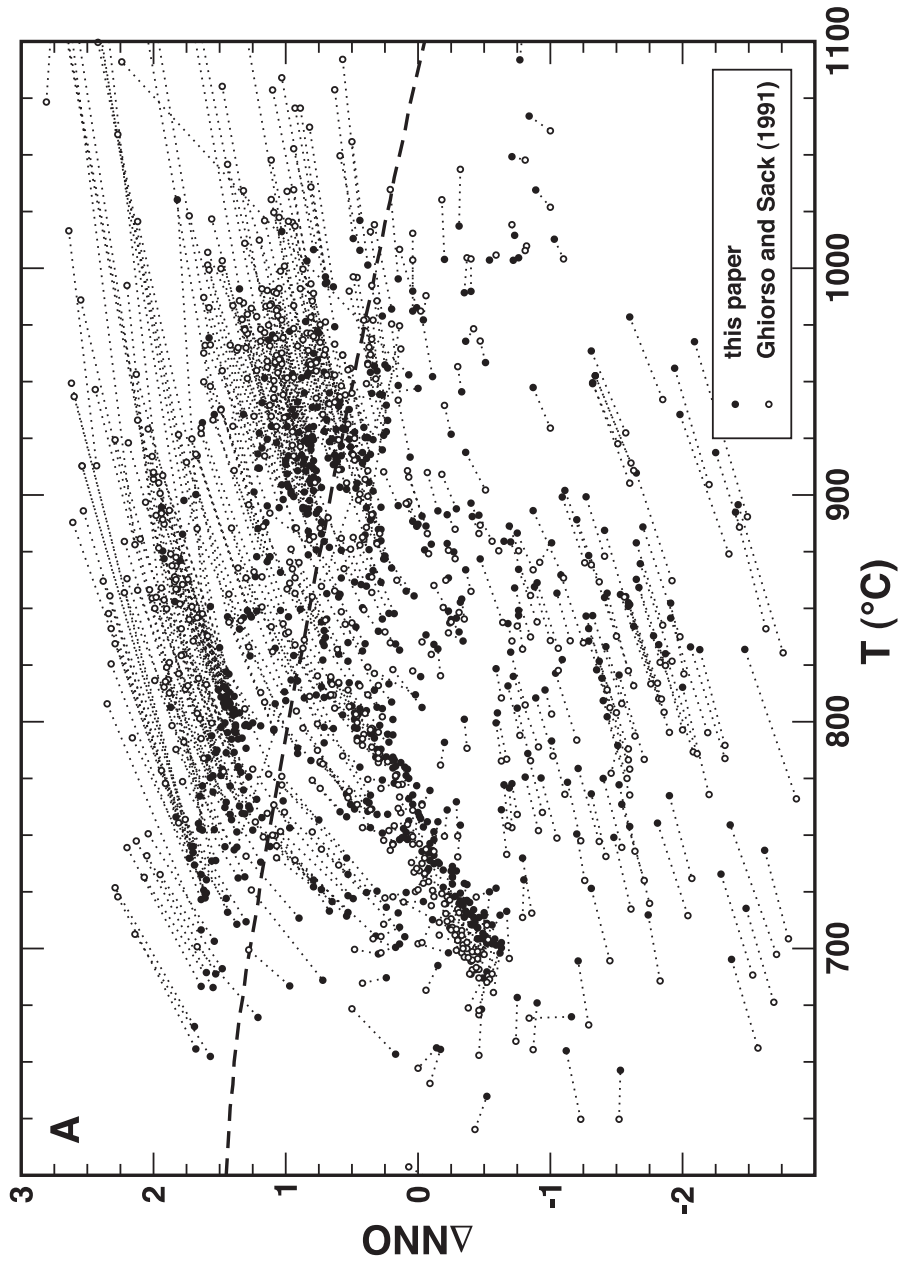


Fig. 24. Comparison of calculated T and f_{O_2} (plotted as in fig. 23) from the model proposed in this paper to that of (A) Ghiorso and Sack (1991).

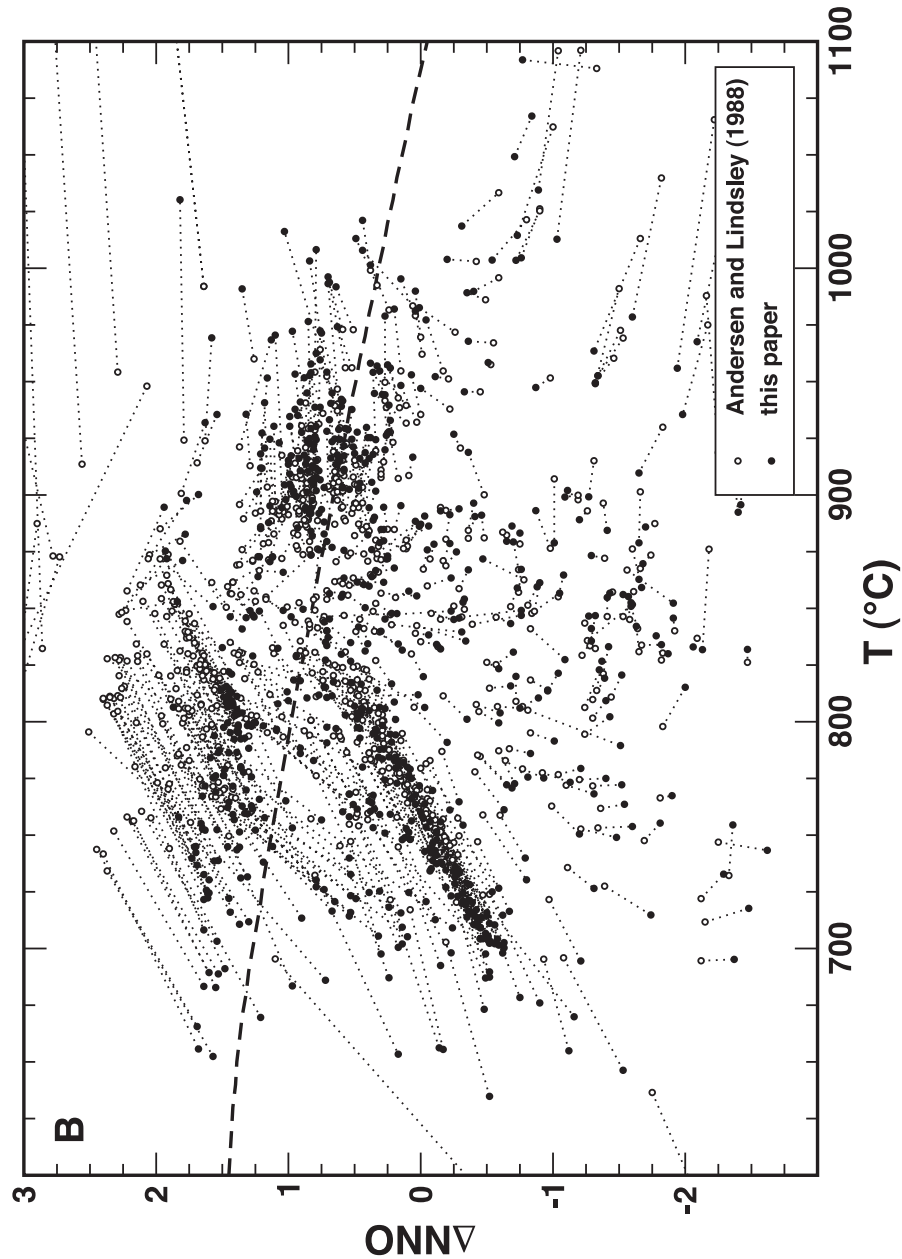


Fig. 24 (continued). (B) Andersen and Lindsley (1988).

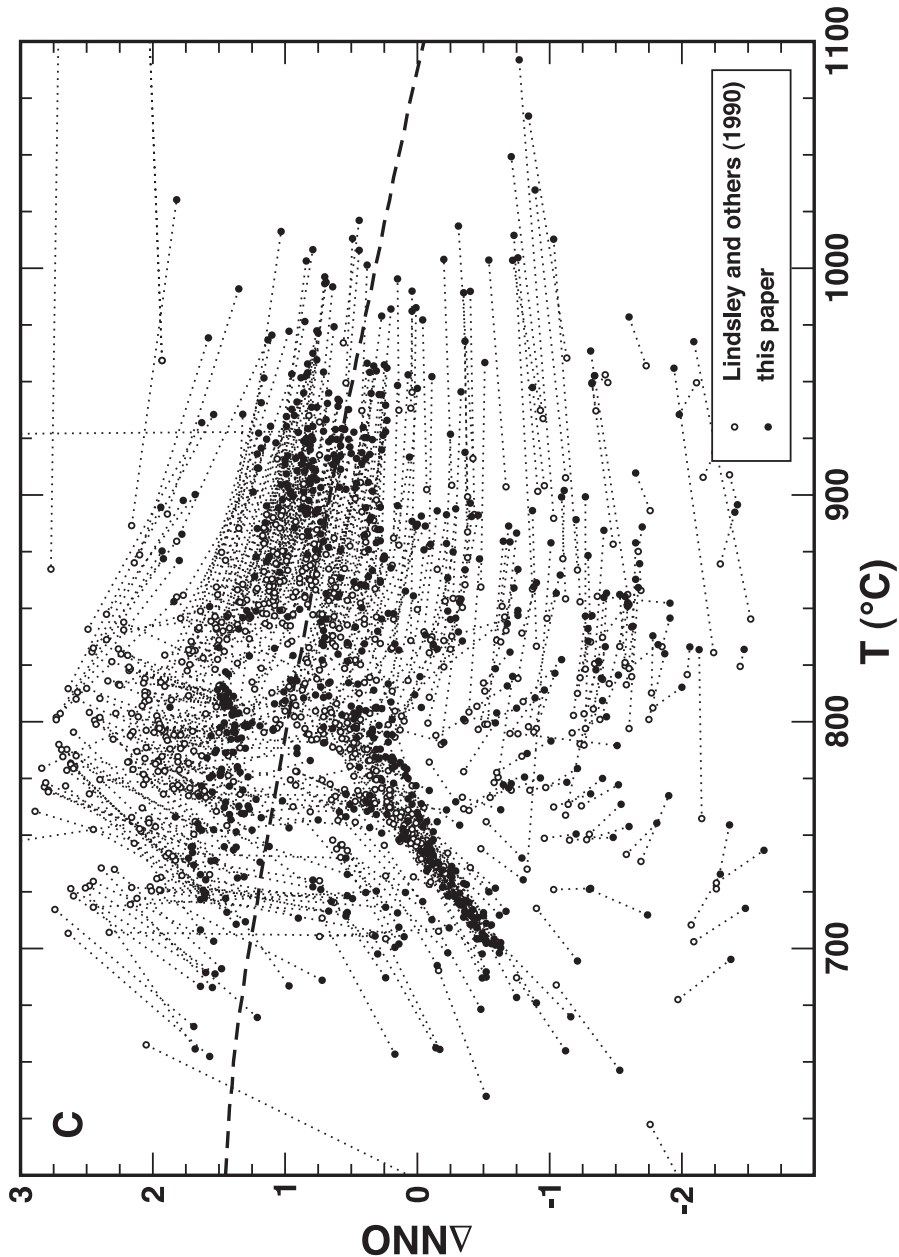


Fig. 24 (continued). (C) Lindsley and others (1990). Recommended methods for projecting natural oxide compositions into the modeled subsystem were followed for (B) and (C). The dotted lines connect derived T and f_{O_2} from the same oxide pair. The dashed curve is the trace of the critical ordering curve for the $\text{Fe}_2\text{O}_3\text{-FeTiO}_3$ binary.

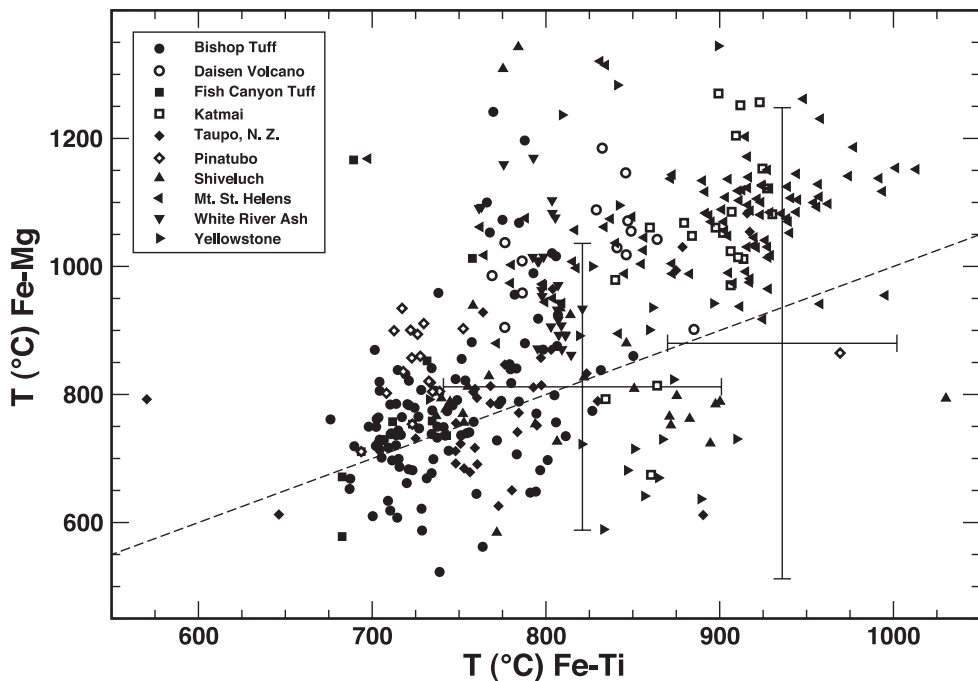


Fig. 25. Comparison of temperatures ($^{\circ}\text{C}$) calculated from two-oxide pairs in dacites and rhyolites from $\text{Fe}^{+2}\text{Ti-(Fe}^{+3})_2$ exchange (abscissa) and $\text{Fe}^{+2}\text{-Mg}$ exchange (ordinate). Symbols are the same as figure 21. Crosses represent average temperatures $\pm 2\sigma$ for recovery of the 800°C and 900°C Mg-doped haplorhylite oxide synthesis experiments of Evans and others (2006). Dashed line traces a 1:1 correlation. Data are excluded that fail the Bacon and Hirschmann (1988) test at the 2σ level.

The uncertainties on the temperature estimates from the $\text{Fe}^{+2}\text{-Mg}$ exchange are clearly larger by a factor of three or four compared to those from $\text{Fe}^{+2}\text{Ti-(Fe}^{+3})_2$ exchange. Recall from figure 13B that the variation in estimated $\text{Fe}^{+2}\text{Ti-(Fe}^{+3})_2$ -exchange temperature due to analytical uncertainty alone is on average $\pm 70^{\circ}\text{C}$ for this subset of the calibration data (much better than this at low to moderate f_{O_2} , much worse at elevated f_{O_2} , for example, fig. 14) and the expected error in T_{FeMg} due to analytical uncertainty is expected to be about a factor of two greater than this. So, the apparent scatter of points displayed in figure 25 can partly be ascribed to analytical error. However, it is also apparent from figure 25 that there are systematic offsets from the 1:1 correlation line that possibly reflect post-eruptive re-equilibration of the oxide pairs, or alternately, indicate some problem with calibration of MgTiO_3 potential in the underlying thermodynamic model. For example, the oxide pairs from dacites at Mt. Pinatubo have T_{FeMg} on average 100°C higher than their $\text{Fe}^{+2}\text{Ti-(Fe}^{+3})_2$ -exchange temperatures and those of Mt. Saint Helens 200°C higher. By contrast, oxides from the Bishop Tuff, Fish Canyon Tuff, Shiveluch volcano, Yellowstone, and the rhyolites of New Zealand have compositions that produce agreement between the two temperature estimates. For those rock suites that show a systematic offset of mean T_{FeMg} , analyses can be chosen whose exchange temperatures are coincident and perhaps suggest a *likely* magmatic condition: Katmai at $\sim 850^{\circ}\text{C}$, Pinatubo at $\sim 710^{\circ}\text{C}$, White River Ash at $\sim 800^{\circ}\text{C}$, and Mt St. Helens with the range 900°C to 950°C.

Surely the lowest temperatures obtained from the $\text{Fe}^{+2}\text{-Mg}$ exchange goethermometer (fig. 25) are unrealistic because they fall below the expected solidus of rhyolitic

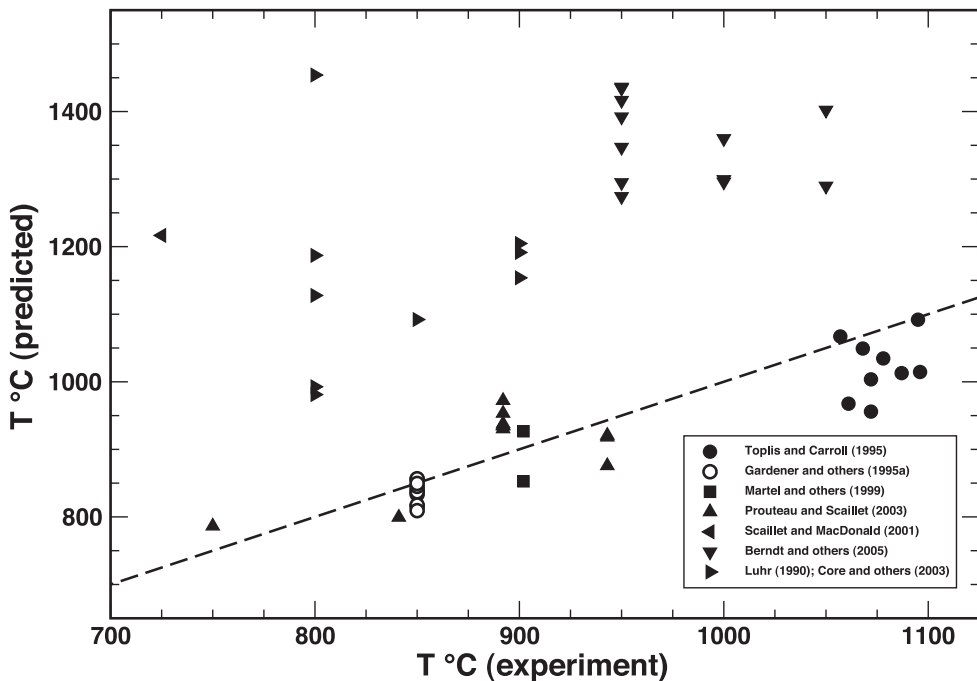


Fig. 26. Temperature recovery from $\text{Fe}^{+2}\text{Ti-(Fe}^{+3})_2$ exchange between experimentally grown pairs of oxides. Dashed line traces a 1:1 correlation.

and dacitic magma. Similarly, the higher temperature estimates are clearly in violation of known experimental constraints on the paragenesis of two-oxide assemblages.

Comparing Model Results to Experimental Data

We can test the reliability of the new model geothermobarometer by extracting T and ΔNNO from the compositions of oxide pairs crystallized experimentally under controlled conditions in complex natural systems. We will exclude the data of Scaillet and Evans (1999) that are incorporated in the calibration of the model. Figure 26 shows the results of this test, based on data from Luhr (1990), Core and others (2003), Toplis and Carroll (1995), Gardner and others (1995a, 1995b), Martel and others (1999), Prouteau and Scaillet (2003), and Berndt and others (2005). This comparison emphasizes an offset in temperature in the very high f_{O_2} region (Luhr and Berndt data), where the isotherms are very closely spaced (fig. 14), but otherwise the agreement is satisfactory. The comparison of extracted versus experimental f_{O_2} (fig. 27) is very satisfactory, even for those experiments where the thermometer is obviously a failure.

The closeness of isotherms at the opposite origins of the Roozeboom diagram (fig. 14) inevitably reduces the accuracy of the $\text{Fe}^{+2}\text{Ti-(Fe}^{+3})_2$ -exchange thermometer when compositions fall in those regions ($\Delta\text{NNO} > +3$ and < -3). Fortunately, analytical accuracy at the high- f_{O_2} extreme is good, because the mole fractions of ilmenite and ulvöspinel depend almost entirely on the contents of Ti, which can be determined at low concentrations using the microprobe with high accuracy. Conversely, the contents of hematite and magnetite close to the Ti-endmember compositions are obtained from the relative amounts of Ti and Fe, both of which are present in

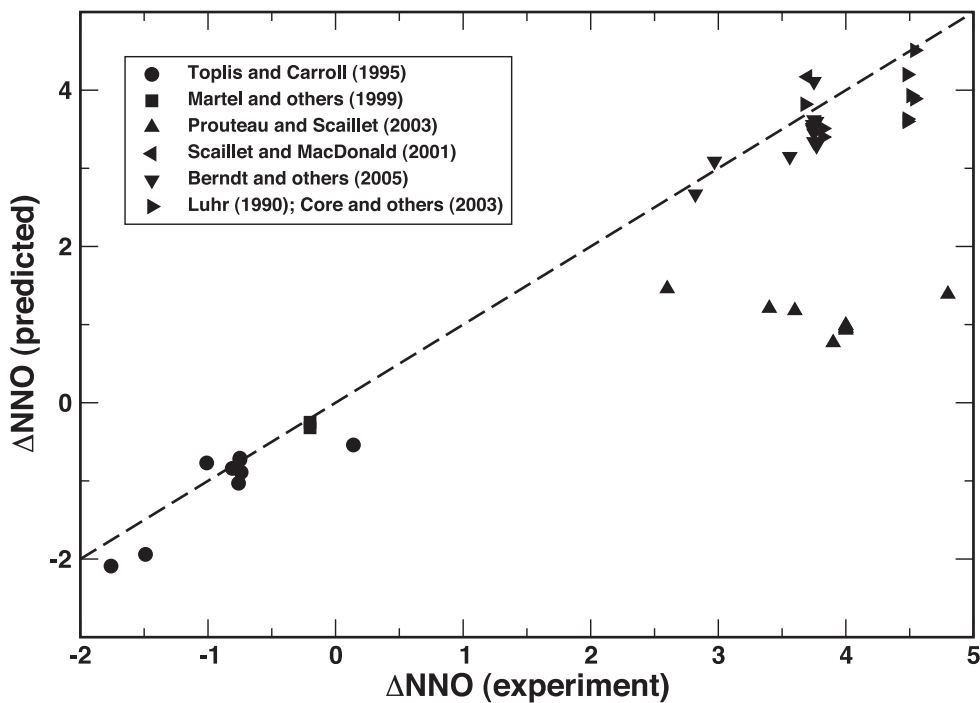


Fig. 27. f_{O_2} recovery from $\text{Fe}^{+2}\text{Ti-(Fe}^{+3})_2$ exchange between experimentally grown pairs of oxides. Dashed line traces a 1:1 correlation.

high concentration, and this is a more difficult analytical problem. Also at this end of the Roozeboom diagram the existence of cation deficiencies in both minerals at high temperatures (Lattard and others, 2005) further complicates the situation. Finally, we noted (Evans and others, 2006) that TiO_2 and FeO by microprobe is apparently subject to uncertainties of 1 to 2 percent relative, depending on the use of pure TiO_2 and Fe_2O_3 standards as opposed to natural analyzed ilmenites.

Comparing Model Results with Petrologic Constraints

In theory there are many independent igneous geothermometers that could serve to test the accuracy of the FeTi-oxide geothermometer in the same rock sample. Of these, however, only those that record equilibration under the conditions of final solidification or those immediately prior to eruption are likely to be useful. As pointed out long ago (Carmichael, 1967), the quench provided by explosive eruption justifies the focus on pyroclastic volcanic rather than plutonic igneous rocks for oxide thermometry. Because they tend not to readjust on cooling in the magma chamber, many if not all of the mineral net-transfer, exchange, and solvus equilibria relevant to igneous thermometry cannot necessarily be expected to corroborate the FeTi-oxide geothermometer/oxygen barometer given the faster cation exchange kinetics of the oxides. On the other hand, if $P_{\text{H}_2\text{O}}$ can be constrained, experimental phase appearance/disappearance diagrams can be useful. In the absence of late to post-magmatic events, thermometry on an erupted magma should give numbers that put it at a temperature sufficiently higher than its solidus for approximately 50 percent liquid to be present. Our calibration rarely gives $\text{Fe}^{+2}\text{Ti-(Fe}^{+3})_2$ -exchange temperatures that are below the solidus, but in some cases may fail to give a temperature estimate that indicates a liquid fraction in excess of 50 percent.

Some high- f_{O_2} silicic magmas crystallize rhombohedral oxide solid solution sufficiently rich in hematite to be cation-disordered ($R\bar{3}c$ structure) at magmatic temperatures. These oxides will tend to show self-reversal of remanent magnetization as a result of cooling through the order-disorder transition and formation of ordered antiphase domains. Our geothermometer should recover temperatures for such magmas that place the crystallization temperature of the rhombohedral oxide in the fully or near-fully disordered state. We find this to be true for the Natib dacite, Philippines (Kennedy and Osborne, 1987), the Nevado del Ruiz andesite (Haag and others, 1990a, 1990b), the Mount Shasta dacite (Lawson and others, 1987), but not for the 1991 Mount Pinatubo dacite (Hoffmann and Fehr, 1996). We return to this last problem below.

There are some petrologic observations that constrain the limbs of the miscibility gap in the rhombohedral oxide supersystem. Two populations of rhombohedral oxide coexisting with magnetite from the rhyodacitic White River Ash, Alaska and Yukon Territory (Lerbekmo and others, 1975) show a compositional gap between 31.6 and 34.3 wt.% TiO_2 (MgO 1.7 wt.%, that is ~ 3.7 mol.% Gk). This corresponds to an interval of about ~ 3 mol.% $FeTiO_3$ between the two limbs (54% and 57%) of the miscibility gap. Further evidence for the gap can be construed from the range of $FeTiO_3$ -contents in the White River ilmenites (20 mole %), compared to the constancy of the compositions of coexisting spinels. Derived temperatures and f_{O_2} for this suite of rocks are tightly clustered, implying that the chemical potentials of $FeTiO_3$ and Fe_2O_3 in the rhombohedral phase are relatively insensitive to compositional variation. This insensitivity is always found for T - X conditions near the crest of a miscibility gap or solvus (for example, figs. 18 and 19). Additional constraints can be found in 47 low-MgMn ilmenites and hematites in $680^\circ C$ metapelites from the Barrovian type area (Ague and others, 2001), which show a spread in $FeTiO_3$ mole fraction from 0.29 to 0.95. Most values are < 0.50 or > 0.78 , consistent with the binary system miscibility gap (fig. 19); only 5 samples fall inside this range—not only inside our spinodal but also the experimental miscibility gap limits of Lindsley (1973) and Burton (1984).

A small proportion of natural siliceous volcanic rocks (Wood and Carmichael, 1973) contain phenocrysts of cummingtonite along with hornblende and Fe-Ti-oxides. By virtue of its breakdown to orthopyroxene, quartz and H_2O , the crystallization of cummingtonite supplies an upper temperature limit on the magma. This is calculated to be $790^\circ C$ at 2 kbar for cummingtonite with $X_{Mg} = 0.7$ and $760^\circ C$ for $X_{Mg} = 0.5$ (Evans and Ghiorso, 1995); about $760^\circ C$ between 200 and 300 MPa for conditions of $a_{H_2O} = 1.0$ and 0.75 in experiments on two samples of rhyolite from the Taupo Volcanic Zone, New Zealand (Nicholls and others, 1992); $730^\circ C$ at 200 to 300 MPa in a synthetic assemblage of two-amphiboles, two pyroxenes, plagioclase (An_{20}), quartz and liquid (Oba and Nicholls, 1986); up to $790^\circ C$ for cummingtonite with $X_{Mg} = 0.62$ based on experiments on Mount St. Helens dacite (Geschwind and Rutherford, 1992); and up to $780^\circ C$ at 220 to 300 MPa for experiments on crushed 1991 Mt. Pinatubo dacite (Rutherford and Devine, 1996).

Thus the “window of opportunity” for magmatic cummingtonite is between, at most, $790^\circ C$ (depending on its X_{Mg}) and the solidus: $\sim 700^\circ C$ for H_2O saturated dacite and $680^\circ C$ for rhyolite at 2 kbar (Ebadi and Johannes, 1991). The uppermost temperatures in this range are less likely because they require formation of cummingtonite at unit activity of quartz and H_2O , the terminal reaction in reverse, as suggested by Rutherford and Devine (1996) in their experiments on the 1991 Mt. Pinatubo dacite. Alternatively, orthopyroxene may react out at higher temperatures in peritectic reactions forming hornblende or biotite (for example, Geschwind and Rutherford, 1992, their fig. 2; Evans and Scaillet, 1997; and B. Scaillet, personal communication, 2002). Rather than as a reaction rim around orthopyroxene, cummingtonite typically

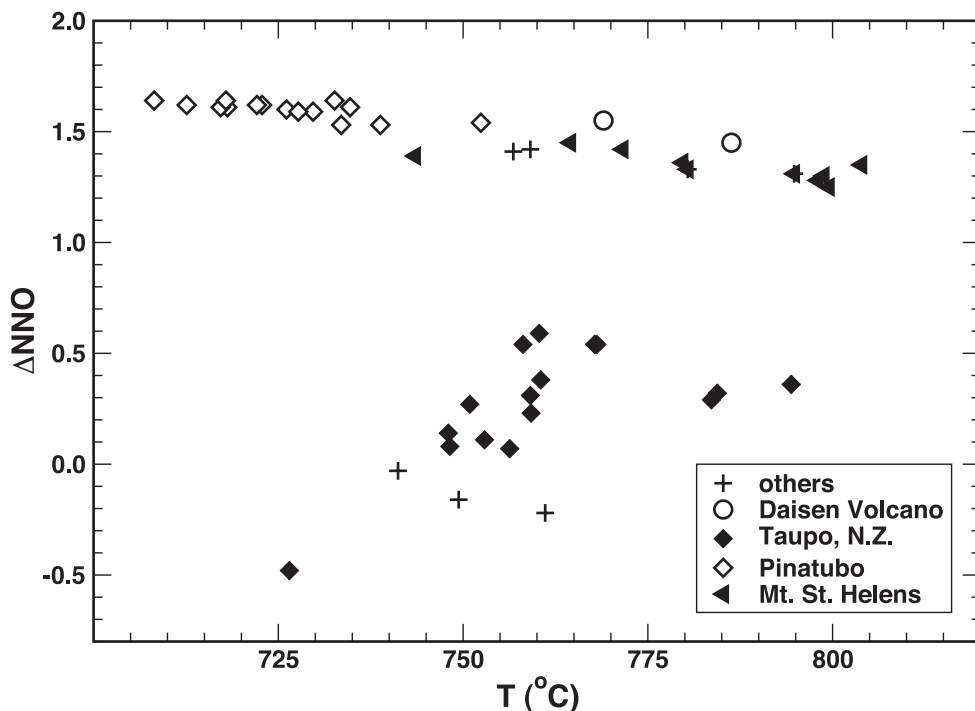


Fig. 28. Temperature and f_{O_2} calculated for the two-oxide dataset from cummingtonite-bearing dacitic and rhyolitic volcanics.

forms separate crystals in lavas (for example, St. Helens dacite, Taupo rhyolite) or rims around the hornblende (for example, Mt. Pinatubo).

In perfect agreement with this window, our new model places all 44 cummingtonite-bearing lavas from the Taupo Volcanic Zone, New Zealand, Daisen Volcano, Mt. Pinatubo, Mt. St. Helens and other scattered localities in the temperature range 705° to 805°C (fig. 28). Ca pfu of cummingtonite coexisting with hornblende in 20 natural rhyolite samples (mostly from the Taupo Volcanic Province) is 0.28 ($2\sigma = 0.055$), indicating temperatures of 700 to 780°C according to the quadrilateral amphibole solvus (Ghiorso and Evans, 2002). So, it appears that the $\text{Fe}^{+2}\text{Ti-(Fe}^{+3})_2$ -exchange temperatures obtained from cummingtonite-bearing assemblages are consistent with the stability field of cummingtonite, implying that in the case of Pinatubo the Fe^{+2}/Mg ratio of one or both oxides has altered post-eruption (fig. 25).

We conclude this section with some observations and comments on two selected volcanic suites.

Bishop Tuff

Hildreth (1979) interpreted $T-f_{\text{O}_2}$ trends in pyroclastic deposits that were erupted during formation of the Long Valley caldera in Southeastern California to represent a pre-eruptive thermal gradient in the parental magma body. Two-oxide $\text{Fe}^{+2}\text{Ti-(Fe}^{+3})_2$ -exchange temperatures, calculated using the original graphical Fe-Ti oxide geothermometer of Buddington and Lindsley (1964) correlated well with the sequence of erupted units, giving temperatures in the range 720° to 790°C. More recent $\text{Fe}^{+2}\text{Ti-(Fe}^{+3})_2$ -exchange geothermometers confirm a $T-f_{\text{O}_2}$ trend but not the same

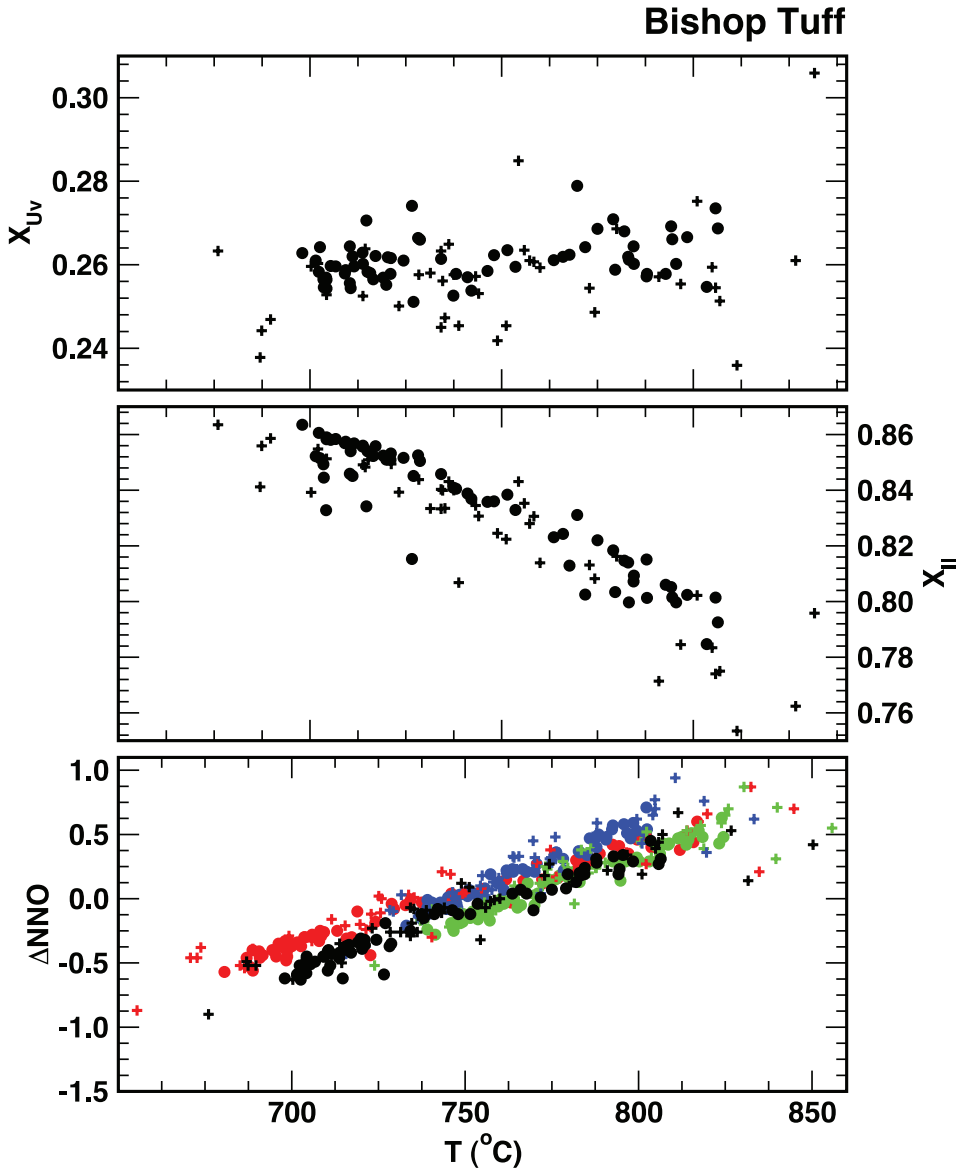


Fig. 29. Analysis of two-oxide pairs from the Bishop Tuff volcanic center. Data are taken from Hildreth (ms, 1977, solid circles) and Hildreth and Wilson (2007, crosses). Upper panel: Spinel compositions (as X_{Uv} , see legend fig. 21) plotted against $\text{Fe}^{+2}\text{Ti-(Fe}^{+3})_2$ exchange temperature. Middle panel: Ilmenite compositions (as X_H , see legend fig. 21) plotted against $\text{Fe}^{+2}\text{Ti-(Fe}^{+3})_2$ exchange temperature. Lower panel: Temperature and f_{O_2} calculated from two-oxide pairs using the $\text{Fe}^{+2}\text{Ti-(Fe}^{+3})_2$ exchange geothermometer. Black symbols: model from this paper; Red symbols: model from Ghiorso and Sack (1991); Green symbols: model from Andersen and Lindsley (1988); Blue symbols: model from Lindsley and others (1990). Data are excluded that fail the Bacon and Hirschmann (1988) test at the 2σ level.

range of temperatures (fig. 29). Both Ghiorso and Sack (1991) and Lindsley and others (1990) have argued that this $T-f_{\text{O}_2}$ range is an artifact of post-eruptive re-equilibration of the oxides. This argument is based primarily on the lack of correlation of oxide composition to that of coexisting phenocrysts of ferromagnesian silicates, the

latter possibly inherited from an early stage in the fractionation history of the body. As the $T_{f\text{O}_2}$ trend is essentially a manifestation of variation in the FeTiO_3 -content of the rhombohedral phase (fig. 29), Lindsley and others (1990) have argued that the trend results from post-eruptive alteration of the Fe/Ti ratio of ilmenite; this argument is supported by the petrographic observation that ilmenite is far less abundant than spinel as a phenocryst phase and that the small size of the ilmenite phenocrysts relative to spinel makes them more susceptible to re-equilibration.

Recently, Wark and others (2007) have applied the titanium-in-quartz geothermometer (Wark and Watson, 2006) to quartz phenocrysts from the Bishop Tuff deposits. Their analysis reveals that temperatures inferred from Ti-contents of the cores of quartz phenocrysts are fairly uniform throughout the body, ranging from 715° to 760°C, with an average at ~720°C in the earliest erupted deposits and ~740°C in the later units⁷. This temperature range is consistent with the two-oxide exchange temperatures recovered from our geothermometer (fig. 29). The rims of Bishop quartzes often contain higher concentrations of Ti, however, and these rims sometimes give temperatures as high as 830°C, though rim and core temperatures appear to coincide in the earliest erupted material. The high-Ti rims on quartz phenocrysts have steep Ti-gradients with respect to the cores, and Gualda (ms, 2007) has calculated that these high-Ti rims probably grew within months or at most years of the onset of eruption. Wark and others (2007) interpret the formation of high-Ti rims on quartz as a result of ejection of hotter magma. Gualda (ms, 2007) has documented however, that both zoned (Ti-rich rimmed) and unzoned (no Ti-rim) quartzes *coexist together* in the same pumice fragment on the scale of one cubic centimeter samples throughout the deposit. He also finds mixed populations of sanidine phenocrysts, some with Ba-rich rims, others without, intimately mixed at the same scale throughout the deposit. Gualda (ms, 2007) concludes that these mixed populations of phenocrysts make it unlikely that any global magmatic event, like an increase in temperature or injection of more primitive magma (Wark and others, 2007), is responsible for the Ti-rims on the quartzes, and he dismisses crystal settling (Anderson and others, 2000) as a mechanism for generation of these mixed populations because large scale movement of crystals is inconsistent with the timescale of rim growth. Gualda (ms, 2007) attributes rim formation to local melt heterogeneity at the mm scale, perhaps sourced by breakdown of biotite phenocrysts. We can conclude from Gualda's (ms, 2007) observations that either quartz phenocrysts were not in chemical equilibrium even within several millimeters of each other just prior to eruption (with the same conclusion applied to phenocrysts of sanidine), or that quartz and sanidine phenocrysts were harvested from spatially distant regions of the magma body and mixed during eruption at the thin section scale (Ruprecht and others, 2008). Gualda's (ms, 2007) petrographic observations of disequilibrium tell us that the highest (quartz rim) temperatures obtained by Wark and others (2007), which are at the extreme high-end of the temperature range calculated from two-oxide pairs (fig. 29), are probably not representative of the whole magma body.

While there appear to be good grounds to argue that some mixed phenocryst populations found in the Bishop pyroclastic deposits were not in chemical equilibrium just prior to eruption, it could be countered that the kinetics of re-equilibration of the Fe-Ti oxides is rapid enough that these phases would record the intensive variables of the late magmatic events—even the eruptive event—with more fidelity. The model

⁷ In order to apply the Ti-in-quartz geothermometer to the Bishop magma, Wark and others (2007) must estimate the activity of TiO_2 in the liquid prior to eruption. This number is subject to some uncertainty. They adopt a value of 0.6 for the entire magma body; a variation of ± 0.1 in a_{TiO_2} translates to a temperature uncertainty of ~20°C.

thermometers we develop in this paper lend some support to this contention: The two-oxide $\text{Fe}^{+2}\text{Ti-(Fe}^{+3})_{\text{2}}$ -exchange temperatures are broadly consistent with Fe^{+2} -Mg-exchange temperatures, and the lowermost of these temperature estimates (fig. 29) is supported by experimental evidence. Bruno Scaillet (personal communication, 2002) performed experiments at 200 MPa on a Bishop Tuff early ignimbrite bulk composition and obtained a water-saturated solidus temperature of 680°C (Quartz in at 710°C, postassium feldspar in at 700°C, plagioclase in at 690°C). His experimental results place the quartz-two feldspar-water saturated “eutectic” at ~690°C, and as quartz, sanidine and plagioclase are ubiquitous phenocryst phases in the erupted pyroclastic material in the Bishop deposit, the experimental evidence suggests that the pre-eruptive temperature of the magma should be at or a bit below the “eutectic” temperature. The temperature gradient of ~100° inferred from the oxides (fig. 29) is inconsistent with Scaillet’s experimental results if the oxides equilibrated with a magma that produced the silicate phenocryst population evidenced by the eruptive deposits. A pressure gradient of 200 or 300 MPa would not be sufficient to reconcile this discrepancy (Tuttle and Bowen, 1958 and Holland and Powell, 2001 for additional data). As the Ti in quartz-cores temperatures span ~720° to 740°C (Wark and others, 2007), which overlap the temperature range derived from the oxides (fig. 29), the experimental and geothermometric observations appear irreconcilable with the conclusion that the quartz-two feldspar-oxide assemblage crystallized at the vapor saturated “eutectic.” Of course, if the bulk composition of the Bishop magma was not that of the early-erupted ignimbrite, as assumed by Scaillet, then the conundrum vanishes, but there is ample evidence from the compositions of melt inclusions in quartz (Hildreth and Wilson, 2007) that the composition of bulk pumice from the early-erupted ignimbrite is representative of the parental liquid. The collected inconsistencies become less troublesome if the erupted products are viewed as sampling a large volume of the original magma body so that phenocrysts associated at the thin section scale need not necessarily be cogenetic (Ruprecht and others, 2008).

Pinatubo

$\text{Fe}^{+2}\text{Ti-(Fe}^{+3})_{\text{2}}$ -exchange temperatures and oxygen fugacities calculated using our new model for the 1991 cummingtonite-bearing Mt. Pinatubo dacite fall in the range 690° to 755°C and NNO+1.5 to NNO+1.7, which is in marked contrast to results obtained from previous formulations (fig. 30). The predicted range of oxygen fugacity is consistent with the experimental study of Evans and Scaillet (1997), who concluded that the Pinatubo oxides formed at $\text{NNO+1.7} \pm 0.2$.

In experiments on the 1991 Mt. Pinatubo dacite, Scaillet and Evans (1999) found no cummingtonite at 780°C and 200 MPa, although charges with added sulfur produced a Ca,Al-rich cummingtonite at these conditions (Evans and others, 2007). However, in the latter case, the normative Hy/Di ratio of the liquid was increased through the uptake of Ca in anhydrite, and the synthetic cummingtonite so produced is distinctly richer in Ca and Al than all natural volcanic cummingtonites. The inference to be drawn from the experiments is that cummingtonite begins to crystallize below 780°C in the Pinatubo magma. The Ca-content of the Mt. Pinatubo cummingtonite, which coexists with hornblende, (0.24 to 0.30 Ca pfu) suggests crystallization temperatures of 710 to 770°C (Ghiorso and Evans, 2002). So, the lines of evidence from both the silicate and the oxide phases converge on a temperature of $\sim 725 \pm 20^\circ\text{C}$.

A potential difficulty that arises if we adopt a temperature like 725°C for the Pinatubo magma is reconciliation of this temperature with the self-reversed remnant magnetization displayed by the rhombohedral phase (Ozima and others, 1992; Hoffman and Fehr, 1996; Bina and others, 1999). Nord and Lawson (1989, 1992) and most recently Harrison and others (2005) discuss the conditions for generation of self-

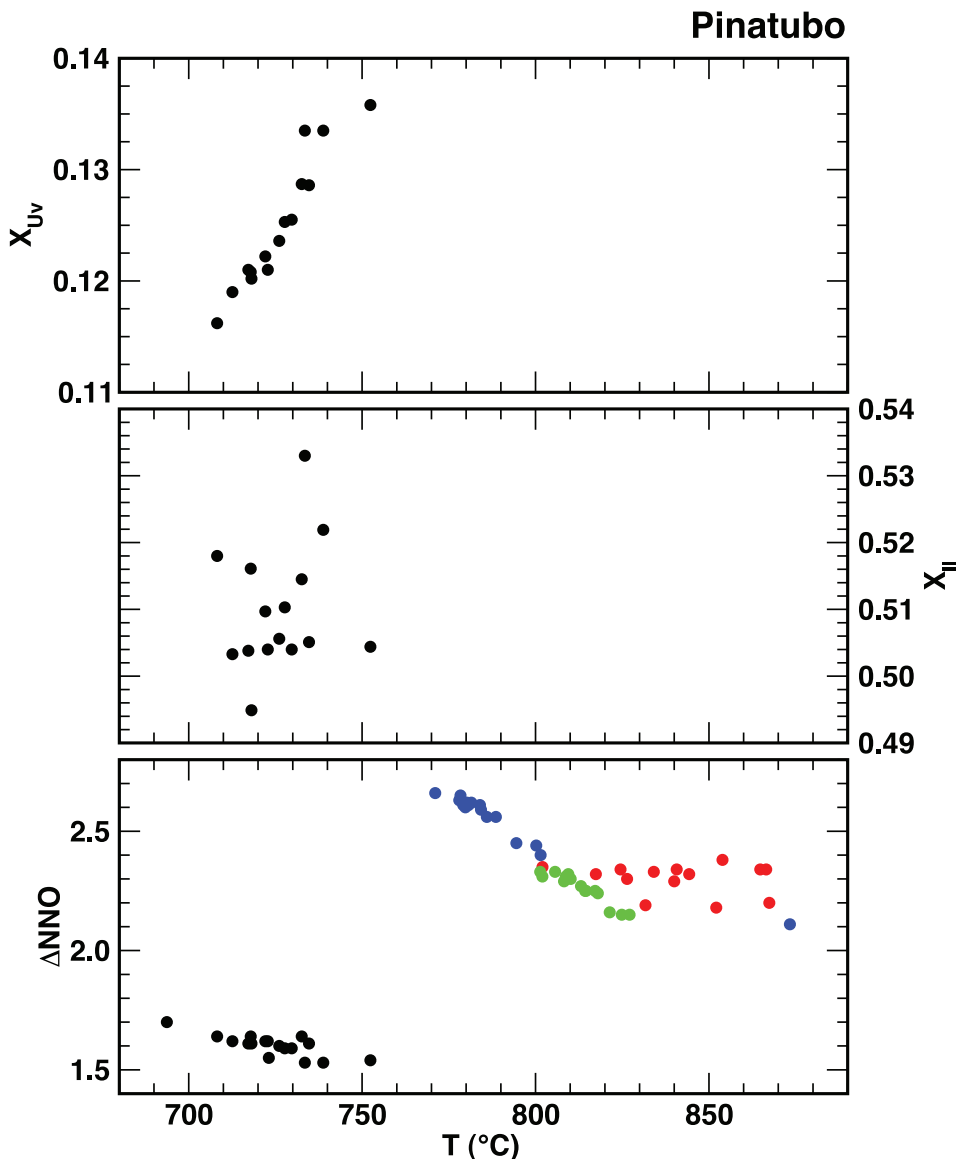


Fig. 30. Analysis of two-oxide pairs from the Mt Pinatubo eruption of 15 June 1991. Arrangement and symbols as in figure 29. Data sources: Rutherford and Devine (1996); Hattori (1996); Pallister and others (1996); and Imai and others (1996). Data are excluded that fail the Bacon and Hirschmann (1988) test at the 2σ level.

reversed thermo-remanent magnetization (SR-TRM) in ilmenite solid solutions. Self-reversal requires the presence of two phases that differ in Fe-content. The less abundant Fe-rich phase acquires a magnetic moment at a higher-temperature than the more abundant Fe-poor phase. At a temperature low enough for the Fe-poor phase to become magnetic, the field generated by the minor phase forces the major phase to acquire a reverse magnetic moment. In the case of ilmenite solid solutions that exhibit SR-TRM and are otherwise chemically homogeneous, the “minor” Fe-rich phase refers

to anti-phase domain boundaries of twins (Harrison and others, 2005) formed on cooling across the critical ordering curve. Nord and Lawson (1989) showed that in this case the strength of SR-TRM relates to the twin boundary surface area per unit volume, and consequently the strongest SR-TRM occurs in samples quenched rapidly through the symmetry transition. On the other hand, annealing below the critical ordering curve allows larger twin domains to form, minimizing twin boundary surface area and reducing or eliminating SR-TRM (Nord and Lawson, 1992). Thus in chemically homogenous ilmenite phenocrysts, it is more likely for SR-TRM to develop in oxides that are grown at temperatures above the critical ordering curve and rapidly erupted. For the Mt. Pinatubo oxides, the critical ordering temperature is calculated to be $\sim 750^\circ\text{C}$, which appears to contradict our suggested equilibration temperature of $\sim 725^\circ\text{C}$. However, Hoffmann and Fehr (1996) have documented that a 60 micron diameter ilmenite phenocyst from the 1991 eruption of Pinatubo exhibits *macroscopic* zonation: a ~ 10 micron Fe-rich hemo-ilmenite rim surrounds a less Fe-rich core. The SR-TRM of this crystal is related to its macroscopic zonation (Hoffmann and Fehr, 1996), supporting the logical suggestion that SR-TRM recorded in the majority of rhombohedral oxides from Pinatubo is of like origin. If that is the case, then the temperature of the critical ordering curve ($\sim 750^\circ\text{C}$) is not an applicable constraint for SR-TRM in these rocks. Whether the macroscopic zonation seen by Hoffmann and Fehr (1996) is derived from sub-solvus exsolution (which would constrain the temperature to be $< 750^\circ\text{C}$) or some pre-eruptive magmatic event requires further investigation of these rocks.

SUMMARY

The thermodynamic model for rhombohedral oxide solid solutions developed in this paper contrasts with the previous work of Ghiorso (1990a) in three principal ways. First, the model is calibrated from data that provide a markedly different temperature and compositional dependence of cation ordering in the system $\text{Fe}_2\text{O}_3\text{-FeTiO}_3$ than that utilized in the previous study. Unlike before, these newer data imply that the $R\bar{3}c$ to $R\bar{3}$ symmetry-breaking phase transition changes character from 2nd to 1st order at a composition close to pure ilmenite. As a consequence the miscibility gap in the series now extends to pure ilmenite; there is no cusp or tricritical termination point to the gap along the binary $\text{Fe}_2\text{O}_3\text{-FeTiO}_3$ join. Second, model parameters are calibrated from an expanded data set of two-oxide phase equilibria spanning the temperature range 800° to 1300°C and oxygen fugacity range NNO—3 to NNO + 3; two-oxide $\text{Fe}^{2+}\text{-Ti}$ exchange data at elevated temperature and under highly-oxidizing conditions were unavailable to the previous calibration. Third, the model makes explicit provision for short-range cation order, whose effect is to reduce the configurational entropy of mixing so that the maximum entropy of a fully random cation distribution is never fully developed.

In combination with a model for the thermodynamics of spinel solid solutions previously published by Sack and Ghiorso (1991a, 1991b), the rhombohedral oxide model developed in this paper is applied to the estimation of temperatures and oxidation state from two-oxide pairs in silicic volcanic rocks. Two measures of temperature may be obtained by examining both $\text{Fe}^{2+}\text{Ti}(\text{Fe}^{3+})_{.2}$ and $\text{Fe}^{2+}(\text{Mg})_{.1}$ exchange between oxides. The results of our new thermometer/oxygen barometer differ from previously calibrated formulations (Andersen and Lindsley, 1988; Lindsley and others, 1990; Ghiorso and Sack, 1991) most notably in the estimation of oxidation state under relatively oxidized conditions ($> \text{NNO}+1$). As an example, oxide pairs from lavas produced during the 1991 Mt. Pinatubo eruption indicated very high redox conditions (NNO + 2.5) from previous thermobarometers, but now correctly reflect more modest oxidation states (NNO + 1.7 \pm 0.1). In other portions of T- f_{O_2} space differences between the previous and proposed thermobarometers is less significant.

SOFTWARE AVAILABILITY

Software for implementing the thermodynamic model developed in this paper is available along with a new version of the Fe-Ti oxide geothermometer/oxygen barometer at the URL <http://www.ofm-research.org/publications.html>.

ACKNOWLEDGMENTS

We would like to thank Dominique Lattard, Ursula Sauerzapf and Bruno Scaillet for sharing data prior to publication and for thoughtful discussions. Jack Lerbekmo kindly donated samples of the White River Ash (Yukon territory) for analysis. Richard Harrison provided valuable insight into methods of dealing approximately with short-range cation-ordering. Discussions with George Bergantz, Joe Dufek and Guilherme Gualda helped clarify a number of issues regarding the Bishop magma body. Reviews by Ben Burton, Jiba Ganguly, and Don Lindsley helped improve the presentation. Material support for this investigation was generously provided by the National Science Foundation through EAR-0207475. This is OFM Research Contribution #9.

APPENDIX

*Alternative Parameterizations of Higher-order Polynomial Expansions
of the Excess Gibbs Free Energy of Solution*

It is convenient to develop alternative parameterizations of higher-order polynomial expansions of the excess Gibbs free energy in order to interpret model parameters in a more physically meaningful way. For example, it is common practice to write the molar excess Gibbs free energy (\bar{G}^{excess}) of a two-component asymmetric regular solution as

$$\bar{G}^{\text{excess}} = X_1 X_2 (W_{112} X_1 + W_{122} X_2) \quad (89)$$

where the Margules parameters (W_{112} , W_{122}) are subscripted to reflect the mole fraction product terms they modify. The parameters of equation (89) can easily be related to the parameters of a symmetric (second order, regular solution) expansion,

$$\bar{G}^{\text{excess}} = X_1 X_2 W_{12} \quad (90)$$

via the mapping

$$W_{12} = \frac{W_{112} + W_{122}}{2} \quad (91)$$

$$\Delta W_{12} = \frac{W_{112} - W_{122}}{2} \quad (92)$$

which transforms equation (89) into

$$\bar{G}^{\text{excess}} = X_1 X_2 [W_{12} + \Delta W_{12}(X_1 - X_2)] \quad (93)$$

and renders obvious the interpretation of the new parameter ΔW_{12} as a measure of the energetic deviation from a regular solution model.

Proceeding along a similar line of argument, a fourth order polynomial expansion of the molar Gibbs free energy in a two-component (binary) solution, given by

$$\bar{G}^{\text{excess}} = X_1 X_2 (W_{1112} X_1^2 + 2W_{1122} X_1 X_2 + W_{1222} X_2^2) \quad (94)$$

can be transformed by adopting the parameter mappings

$$W_{112} = \frac{W_{1112} + W_{1122}}{2} \quad (95)$$

$$\Delta W_{112} = \frac{W_{1112} - W_{1122}}{2} \quad (96)$$

$$W_{122} = \frac{W_{1122} + W_{1222}}{2} \quad (97)$$

and

$$\Delta W_{122} = \frac{W_{1122} - W_{1222}}{2} \quad (98)$$

Given these transformations equation (94) becomes

$$\bar{G}^{excess} = X_1 X_2 \{X_1 [W_{112} + \Delta W_{112} (X_1 - X_2)] + X_2 [W_{122} + \Delta W_{122} (X_1 - X_2)]\} \quad (99)$$

or, alternately,

$$\bar{G}^{excess} = X_1 X_2 [X_1 W_{112} + X_2 W_{122} + (X_1 - X_2)(X_1 \Delta W_{112} + X_2 \Delta W_{122})] \quad (100)$$

Making additional parameter mappings given by

$$\Delta W_{12} = \frac{W_{112} - W_{122}}{2} = \frac{\Delta W_{112} + \Delta W_{122}}{2} \quad (101)$$

and

$$\Delta^2 W_{12} = \frac{\Delta W_{112} - \Delta W_{122}}{2} \quad (102)$$

along with equation (91), allows equation (100) to be written:

$$\bar{G}^{excess} = X_1 X_2 [W_{12} + \Delta W_{12} (X_1 - X_2) + \Delta^2 W_{12} (X_1 - X_2)^2] \quad (103)$$

The advantage of equation (103) is that the parameters W_{12} , ΔW_{12} , and $\Delta^2 W_{12}$ explicitly and *uniquely* account for 2nd, 3rd, and 4th order perturbations in the excess Gibbs free energy, whereas these effects are mixed in the original Margules parameters (W_{1112} , W_{1122} , W_{1222}) of equation (94).

Finally, a fourth order expansion of the excess Gibbs free energy in a *strictly* ternary system (a three-component solution) can be written

$$\bar{G}^{excess} = X_1 X_2 X_3 [W_{1123} X_1 + W_{1223} X_2 + W_{1233} X_3] \quad (104)$$

Adopting

$$W_{123} = \frac{1}{3} (W_{1123} + W_{1223} + W_{1233}) \quad (105)$$

$$\Delta W_{1123} = W_{1123} - W_{123} \quad (106)$$

$$\Delta W_{1223} = W_{1223} - W_{123} \quad (107)$$

$$\Delta W_{1233} = W_{1233} - W_{123} \quad (108)$$

(from which it is clear that $\Delta W_{1123} + \Delta W_{1223} + \Delta W_{1233} = 0$), equation (104) may be transformed to one of three equivalent alternate expressions:

$$\bar{G}^{excess} = X_1 X_2 X_3 [W_{123} + \Delta W_{1223} (X_2 - X_1) + \Delta W_{1233} (X_3 - X_1)] \quad (109)$$

$$\bar{G}^{excess} = X_1 X_2 X_3 [W_{123} + \Delta W_{1123} (X_1 - X_2) + \Delta W_{1233} (X_3 - X_2)] \quad (110)$$

$$\bar{G}^{excess} = X_1 X_2 X_3 [W_{123} + \Delta W_{1123} (X_1 - X_3) + \Delta W_{1223} (X_2 - X_3)] \quad (111)$$

where the parameters ΔW_{1123} , ΔW_{1223} , and ΔW_{1233} embody 4th order deviations from the symmetric ternary term (W_{123}).

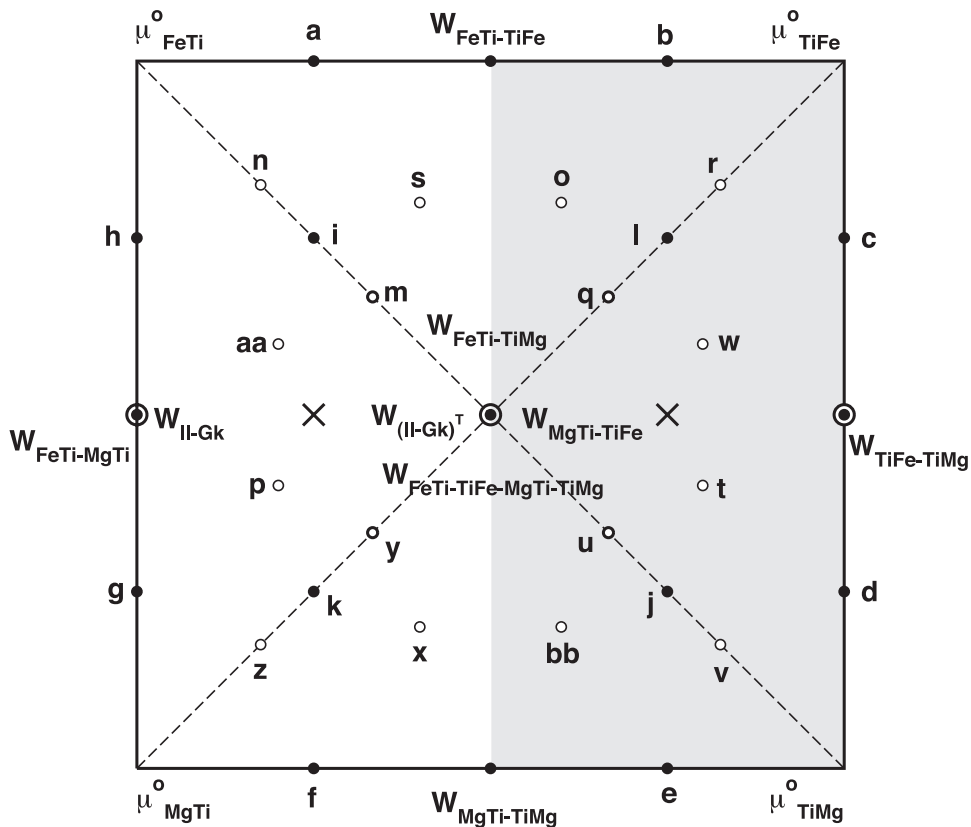


Fig. 31. Composition-ordering space projection for the system $\text{FeTiO}_3\text{-MgTiO}_3$. FeTi and MgTi refer to FeTiO_3 and MgTiO_3 endmembers with Ti^{4+} ordered on “B” octahedral layers. TiFe and TiMg denote structures with Ti^{4+} on “A” octahedral layers. Taylor expansion parameters are plotted at the location of greatest influence on the shape of the Gibbs surface, that is the position where the mole fraction product that multiplies the parameter in equation (112) has a maximal value. See table 3 for legend of parameter abbreviations. Note that the Gibbs energy of the system is mirrored along the section that separates the shaded and unshaded regions of the plot.

Molar Vibrational Gibbs Free Energy in the Supersystem $\text{FeTiO}_3\text{-MgTiO}_3\text{-MnTiO}_3\text{-Fe}_2\text{O}_3\text{-Al}_2\text{O}_5$

The purpose of this section is to describe the extension of equation (16) and its symmetry-reduced equivalent, equation (29), to the compositional super-system of interest. The major complication that arises in this analysis is the recognition of the functional form of the energetic coupling between order parameters; specifically, terms that are permitted by energetic symmetry in the Taylor expansion of the molar vibrational Gibbs free energy must be identified. This discovery can be most easily undertaken by first examining order-parameter coupling along the $\text{FeTiO}_3\text{-MgTiO}_3$ join. Following that examination, the $\text{FeTiO}_3\text{-MgTiO}_3$ model expression can readily be extended to the system $\text{FeTiO}_3\text{-MgTiO}_3\text{-Fe}_2\text{O}_3$ by mimicking the analysis of the system $\text{FeTiO}_3\text{-Fe}_2\text{O}_3$ presented in the text. Energetic terms for the remaining components (MnTiO_3 , Al_2O_5) can subsequently be added by inspection. Recall from the text that the bulk mole fraction of FeTiO_3 , MgTiO_3 , MnTiO_3 , Al_2O_5 , and Fe_2O_3 in the solid solution are given by variables X , Y , Z , C , and $1-X-Y-Z-C$, respectively. The order parameter for partitioning of Fe^{2+} between B and A octahedral layers is denoted s , that for Mg is given by t , and that for Mn is denoted u . Ti partitions between the A and B octahedral layers as the order parameter sum $s + t + u$.

The $\text{FeTiO}_3\text{-MgTiO}_3$ join.—The vertices of composition-ordering space for the $\text{FeTiO}_3\text{-MgTiO}_3$ join are, $[\text{Fe}^{2+}]^A[\text{Ti}^{4+}]^B\text{O}_3$, $[\text{Ti}^{4+}]^A[\text{Fe}^{2+}]^B\text{O}_3$, $[\text{Mg}^{2+}]^A[\text{Ti}^{4+}]^B\text{O}_3$, and $[\text{Ti}^{4+}]^A[\text{Mg}^{2+}]^B\text{O}_3$, which are abbreviated as FeTi , TiFe , MgTi , and TiMg , respectively (fig. 31). A 4th order Taylor expansion of the vibrational Gibbs free energy of solution is given by

TABLE 3
Table of abbreviations for notation in Figure 31

$a = W_{FeTi-TiFe} + \frac{1}{2}\Delta W_{FeTi-TiFe} + \frac{1}{4}\Delta^2 W_{FeTi-TiFe}$	$o = W_{FeTi-TiFe-MgTi} + \Delta W_{FeTi-TiFe^2-MgTi}$
$b = W_{FeTi-TiFe} - \frac{1}{2}\Delta W_{FeTi-TiFe} + \frac{1}{4}\Delta^2 W_{FeTi-TiFe}$	$p: redundant combination of m, n and o$
$c = W_{TiFe-TiMg} + \frac{1}{2}\Delta W_{TiFe-TiMg} + \frac{1}{4}\Delta^2 W_{TiFe-TiMg}$	$q = W_{FeTi-TiFe-TiMg}$
$d = W_{TiFe-TiMg} - \frac{1}{2}\Delta W_{TiFe-TiMg} + \frac{1}{4}\Delta^2 W_{TiFe-TiMg}$	$r = W_{FeTi-TiFe-TiMg} + \Delta W_{FeTi-TiFe^2-TiMg}$
$e = W_{MgTi-TiMg} - \frac{1}{2}\Delta W_{MgTi-TiMg} + \frac{1}{4}\Delta^2 W_{MgTi-TiMg}$	$s = W_{FeTi-TiFe-TiMg} + \Delta W_{FeTi^2-TiFe-TiMg}$
$f = W_{MgTi-TiMg} + \frac{1}{2}\Delta W_{MgTi-TiMg} + \frac{1}{4}\Delta^2 W_{MgTi-TiMg}$	$t: redundant combination of q, r and s$
$g = W_{FeTi-MgTi} - \frac{1}{2}\Delta W_{FeTi-MgTi} + \frac{1}{4}\Delta^2 W_{FeTi-MgTi}$	$u = W_{TiFe-MgTi-TiMg}$
$h = W_{FeTi-MgTi} + \frac{1}{2}\Delta W_{FeTi-MgTi} + \frac{1}{4}\Delta^2 W_{FeTi-MgTi}$	$v = W_{TiFe-MgTi-TiMg} + \Delta W_{TiFe-MgTi-TiMg^2}$
$i = W_{FeTi-TiMg} + \frac{1}{2}\Delta W_{FeTi-TiMg} + \frac{1}{4}\Delta^2 W_{FeTi-TiMg}$	$w: redundant combination of u, v and x$
$j = W_{FeTi-TiMg} - \frac{1}{2}\Delta W_{FeTi-TiMg} + \frac{1}{4}\Delta^2 W_{FeTi-TiMg}$	$x = W_{TiFe-MgTi-TiMg} + \Delta W_{TiFe-MgTi^2-TiMg}$
$k = W_{MgTi-TiFe} - \frac{1}{2}\Delta W_{MgTi-TiFe} + \frac{1}{4}\Delta^2 W_{MgTi-TiFe}$	$y = W_{FeTi-MgTi-TiMg}$
$l = W_{MgTi-TiFe} + \frac{1}{2}\Delta W_{MgTi-TiFe} + \frac{1}{4}\Delta^2 W_{MgTi-TiFe}$	$z = W_{FeTi-MgTi-TiMg} + \Delta W_{FeTi-MgTi^2-TiMg}$
$m = W_{FeTi-TiFe-MgTi}$	$aa: redundant combination of y, z and bb$
$n = W_{FeTi-TiFe-MgTi} + \Delta W_{FeTi^2-TiFe-MgTi}$	$bb = W_{FeTi-MgTi-TiMg} + \Delta W_{FeTi-MgTi-TiMg^2}$

$$\begin{aligned}
 \bar{G}^* = & X_{FeTi} \mu_{FeTi} + X_{TiFe} \mu_{TiFe} + X_{MgTi} \mu_{MgTi} + X_{TiMg} \mu_{TiMg} + X_{FeTi} X_{TiFe} [W_{FeTi-TiFe} + \Delta W_{FeTi-TiFe} (X_{FeTi} - X_{TiFe}) \\
 & + \Delta^2 W_{FeTi-TiFe} (X_{FeTi} - X_{TiFe})^2] + X_{FeTi} X_{MgTi} [W_{FeTi-MgTi} + \Delta W_{FeTi-MgTi} (X_{FeTi} - X_{MgTi}) + \Delta^2 W_{FeTi-MgTi} (X_{FeTi} \\
 & - X_{MgTi})^2] + X_{FeTi} X_{TiMg} [W_{FeTi-TiMg} + \Delta W_{FeTi-TiMg} (X_{FeTi} - X_{TiMg}) + \Delta^2 W_{FeTi-TiMg} (X_{FeTi} - X_{TiMg})^2] \\
 & + X_{TiFe} X_{MgTi} [W_{TiFe-MgTi} + \Delta W_{TiFe-MgTi} (X_{TiFe} - X_{MgTi}) + \Delta^2 W_{TiFe-MgTi} (X_{TiFe} - X_{MgTi})^2] + X_{TiFe} X_{TiMg} [W_{TiFe-TiMg} \\
 & + \Delta W_{TiFe-TiMg} (X_{TiFe} - X_{TiMg}) + \Delta^2 W_{TiFe-TiMg} (X_{TiFe} - X_{TiMg})^2] + X_{MgTi} X_{TiMg} [W_{MgTi-TiMg} \\
 & + \Delta W_{MgTi-TiMg} (X_{MgTi} - X_{TiMg}) + \Delta^2 W_{MgTi-TiMg} (X_{MgTi} - X_{TiMg})^2] \\
 & + X_{FeTi} X_{TiFe} X_{MgTi} \left[\begin{array}{l} W_{FeTi-TiFe-MgTi} + \Delta W_{FeTi^2-TiFe-MgTi} (X_{FeTi} - X_{MgTi}) \\ + \Delta W_{FeTi-TiFe^2-MgTi} (X_{TiFe} - X_{MgTi}) \end{array} \right] \\
 & + X_{FeTi} X_{TiFe} X_{TiMg} \left[\begin{array}{l} W_{FeTi-TiFe-TiMg} + \Delta W_{FeTi^2-TiFe-TiMg} (X_{FeTi} - X_{TiMg}) \\ + \Delta W_{FeTi-TiFe^2-TiMg} (X_{TiFe} - X_{TiMg}) \end{array} \right] \\
 & + X_{FeTi} X_{MgTi} X_{TiMg} \left[\begin{array}{l} W_{FeTi-MgTi-TiMg} + \Delta W_{FeTi-MgTi^2-TiMg} (X_{MgTi} - X_{FeTi}) \\ + \Delta W_{FeTi-MgTi-TiMg^2} (X_{TiMg} - X_{FeTi}) \end{array} \right] \\
 & + X_{TiFe} X_{MgTi} X_{TiMg} \left[\begin{array}{l} W_{TiFe-MgTi-TiMg} + \Delta W_{TiFe-MgTi^2-TiMg} (X_{MgTi} - X_{TiFe}) \\ + \Delta W_{TiFe-MgTi-TiMg^2} (X_{TiMg} - X_{TiFe}) \end{array} \right] \\
 & + X_{FeTi} X_{TiFe} X_{MgTi} X_{TiMg} W_{FeTi-TiFe-MgTi-TiMg} \quad (112)
 \end{aligned}$$

where advantage has been taken of the parameter simplification developed earlier in this Appendix for mapping 4th order terms to alternative binary and ternary parameters, with higher order deviations expressed as delta quantities. In figure 31 the preferred set of parameters identified in equation (112) are plotted at locations in composition ordering space where they have maximal influence on the shape of the Gibbs surface.

Certain symmetrical relations must exist between the parameters in equation (112). As an example, consider the Gibbs free energy of the system at the composition identified by the symbol "X" in the unshaded quadrant of figure 31:

$$X_{\text{FeTi}} = \frac{1}{2}, \quad X_{\text{TiFe}} = \frac{1}{4}, \quad X_{\text{MgTi}} = \frac{1}{2}, \quad X_{\text{TiMg}} = \frac{1}{4} \quad (113)$$

This energy must be identical to that at the composition "X" in the shaded quadrant:

$$X_{\text{FeTi}} = \frac{1}{4}, \quad X_{\text{TiFe}} = \frac{1}{2}, \quad X_{\text{MgTi}} = \frac{1}{4}, \quad X_{\text{TiMg}} = \frac{1}{2} \quad (114)$$

The difference between these two energies should be zero:

$$\begin{aligned} \Delta \bar{G}^* = 0 &= \frac{1}{2} \frac{1}{4} \frac{1}{2} \Delta W_{\text{FeTi}-\text{TiFe}} + \frac{1}{2} \frac{1}{4} \frac{1}{2} \Delta W_{\text{MgTi}-\text{TiMg}} + \left(\frac{1}{2} \frac{1}{2} - \frac{1}{4} \frac{1}{4} \right) (W_{\text{FeTi}-\text{MgTi}} - W_{\text{TiFe}-\text{TiMg}}) \\ &+ \frac{1}{2} \frac{1}{2} \frac{1}{4} (\Delta W_{\text{FeTi}-\text{TiMg}} - \Delta W_{\text{TiFe}-\text{MgTi}}) + \left(\frac{1}{2} \frac{1}{2} \frac{1}{4} - \frac{1}{2} \frac{1}{4} \frac{1}{4} \right) (W_{\text{FeTi}-\text{TiFe}-\text{MgTi}} - W_{\text{FeTi}-\text{TiFe}-\text{TiMg}}) \\ &+ \left(\frac{1}{2} \frac{1}{2} \frac{1}{4} - \frac{1}{2} \frac{1}{4} \frac{1}{4} \right) (W_{\text{FeTi}-\text{MgTi}-\text{TiMg}} - W_{\text{TiFe}-\text{MgTi}-\text{TiMg}}) + \left(\frac{1}{2} \frac{1}{4} \frac{1}{4} + \frac{1}{2} \frac{1}{2} \frac{1}{4} \right) (\Delta W_{\text{FeTi}^2-\text{TiFe}-\text{TiMg}} \\ &- \Delta W_{\text{FeTi}-\text{TiFe}^2-\text{MgTi}}) + \left(\frac{1}{2} \frac{1}{4} \frac{1}{4} + \frac{1}{2} \frac{1}{2} \frac{1}{4} \right) (\Delta W_{\text{TiFe}-\text{MgTi}^2-\text{TiMg}} - \Delta W_{\text{FeTi}-\text{MgTi}-\text{TiMg}^2}) \end{aligned} \quad (115)$$

which is true if and only if

$$\left. \begin{aligned} \Delta W_{\text{FeTi}-\text{TiFe}} &= 0 \\ \Delta W_{\text{MgTi}-\text{TiMg}} &= 0 \\ W_{\text{FeTi}-\text{MgTi}} &= W_{\text{TiFe}-\text{TiMg}} \\ \Delta W_{\text{FeTi}-\text{TiMg}} &= \Delta W_{\text{TiFe}-\text{MgTi}} \\ W_{\text{FeTi}-\text{TiFe}-\text{MgTi}} &= W_{\text{FeTi}-\text{TiFe}-\text{TiMg}} \\ W_{\text{FeTi}-\text{MgTi}-\text{TiMg}} &= W_{\text{TiFe}-\text{MgTi}-\text{TiMg}} \\ \Delta W_{\text{FeTi}^2-\text{TiFe}-\text{TiMg}} &= \Delta W_{\text{FeTi}-\text{TiFe}^2-\text{MgTi}} \\ \Delta W_{\text{TiFe}-\text{MgTi}^2-\text{TiMg}} &= \Delta W_{\text{FeTi}-\text{MgTi}-\text{TiMg}^2} \end{aligned} \right\} \quad (116)$$

Substituting equation (116) into equation (112) (and abbreviating $\text{FeTi} = \text{I}$ and $\text{MgTi} = \text{G}$), gives

$$\begin{aligned} G &= X\mu_{\text{I}}^o + Y\mu_{\text{G}}^o + \frac{1}{4}(X^2 - s^2)[W_{\text{II}-\text{I}} + \Delta^2 W_{\text{II}-\text{I}} s^2] + \frac{1}{4}(Y^2 - t^2)[W_{\text{GK}-\text{G}} + \Delta^2 W_{\text{GK}-\text{G}} t^2] + \frac{1}{2}XY(W_{\text{II}-\text{G}} \\ &+ W_{(\text{II}-\text{G})^2}) + \frac{1}{2}st(W_{\text{II}-\text{G}} - W_{(\text{II}-\text{G})^2}) + \frac{1}{4}(X^2 + s^2)Y(\Delta W_{\text{II}-\text{G}} + \Delta W_{(\text{II}-\text{G})^2}) - \frac{1}{4}(Y^2 + t^2)X(\Delta W_{\text{II}-\text{G}} \\ &+ \Delta W_{(\text{II}-\text{G})^2}) + \frac{1}{2}(X - Y)st(\Delta W_{\text{II}-\text{G}} - \Delta W_{(\text{II}-\text{G})^2}) - \frac{1}{4}(Y^2 + t^2)(X^2 + s^2)(\Delta^2 W_{\text{II}-\text{G}} + \Delta^2 W_{(\text{II}-\text{G})^2}) + \frac{1}{8}(X^2 \\ &+ Y^2)XY(\Delta^2 W_{\text{II}-\text{G}} + \Delta^2 W_{(\text{II}-\text{G})^2}) + \frac{3}{8}(s^2 + t^2)XY(\Delta^2 W_{\text{II}-\text{G}} \\ &+ \Delta^2 W_{(\text{II}-\text{G})^2}) + \frac{1}{8}(s^2 + t^2)st(\Delta^2 W_{\text{II}-\text{G}} - \Delta^2 W_{(\text{II}-\text{G})^2}) + \frac{3}{8}(X^2 + Y^2)st(\Delta^2 W_{\text{II}-\text{G}} - \Delta^2 W_{(\text{II}-\text{G})^2}) \end{aligned}$$

$$\begin{aligned}
 & - XYst(\Delta^2 W_{II-Gk} - \Delta^2 W_{(II-Gk)^T}) + \frac{1}{4}(X^2 - s^2)YW_{II^2-Gk} + \frac{1}{4}(Y^2 - t^2)XW_{II-Gk^2} - \frac{1}{8}(Y^2 + t^2)(X^2 - s^2)(\Delta W_{II^3-Gk} \\
 & + \Delta W_{(II^3-Gk)^T}) + \frac{1}{8}(X^2 - s^2)XY(\Delta W_{II^3-Gk} + \Delta W_{(II^3-Gk)^T}) + \frac{1}{8}(X^2 - s^2)st(\Delta W_{II^3-Gk} - \Delta W_{(II^3-Gk)^T}) - \frac{1}{8}(X^2 \\
 & + s^2)(Y^2 - t^2)(\Delta W_{II-Gk^3} + \Delta W_{(II-Gk^3)^T}) + \frac{1}{8}(Y^2 - t^2)XY(\Delta W_{II-Gk^3} \\
 & + \Delta W_{(II-Gk^3)^T}) + \frac{1}{8}(Y^2 - t^2)st(\Delta W_{II-Gk^3} - \Delta W_{(II-Gk^3)^T}) + \frac{1}{16}(X^2 - s^2)(Y^2 - t^2)W_{II^2-Gk^2} \quad (117)
 \end{aligned}$$

where the terms in bold describe energetic contributions arising from order-parameter coupling. Note that the energetic symmetry enforces the constraint that the sum of exponents of order parameters in any term of the expression must be even, but if a given term contains distinct order parameters (terms involving s and t), these may appear individually as odd powers as long as the product exponent sum is even.

Along the fully ordered $\text{FeTiO}_3\text{-MgTiO}_3$ join, equation (117) reduces to:

$$\bar{G}^* = X\mu_H^o + Y\mu_{Gk}^o + XY[W_{II-Gk} + (X - Y)\Delta W_{II-Gk} + (X - Y)^2\Delta^2 W_{II-Gk}]$$

Experimental constraints on the enthalpy of mixing along this join (for example, Pownceby and Fisher-White, 1999) suggests that both parameters ΔW_{II-Gk} and $\Delta^2 W_{II-Gk}$ may be taken to be zero. By analogy, we take $\Delta W_{(II-Gk)^T}$ and $\Delta^2 W_{(II-Gk)^T}$ to be zero, and for simplicity, we assume that all 3rd and 4th order parameters that are strictly interior to composition-ordering space are zero (that is, $W_{II^2-Gk^2}$, $W_{II^2-Gk^3}$, W_{II-Gk^3} , ΔW_{II^3-Gk} , $\Delta W_{(II^3-Gk)^T}$, ΔW_{II-Gk^3} , and $\Delta W_{(II-Gk^3)^T}$). These assumptions reduce equation (117) to

$$\begin{aligned}
 \bar{G}^* = & X\mu_H^o + Y\mu_{Gk}^o + (X^2 - s^2)\frac{W_{II-II}}{4} + (Y^2 - t^2)\frac{W_{Gk-Gk}}{4} \\
 & + XY\frac{W_{II-Gk} + W_{(II-Gk)^T}}{2} + st\frac{W_{II-Gk} - W_{(II-Gk)^T}}{2} \\
 & + (X^2 - s^2)s^2\frac{\Delta^2 W_{II-II}}{4} + (Y^2 - t^2)t^2\frac{\Delta^2 W_{Gk-Gk}}{4} \quad (118)
 \end{aligned}$$

which we adopt as the preferred model expression for the $\text{FeTiO}_3\text{-MgTiO}_3$ join.

FeTiO₃-MgTiO₃-Fe₂O₃ join.—Taking $\Delta^2 W_{Hm-II}$ and ΔW_{Hm-II^3} to be zero (which is consistent with the analysis of cation-ordering, miscibility gap data, enthalpy of solution and two-oxide phase equilibria developed in the body of the text), equation (29) can be written in simplified form

$$\begin{aligned}
 \bar{G}^* = & (1 - X)\mu_{Hm}^o + X\mu_{II}^o + (1 - X)X[W_{Hm-II} + (1 - X - Y)\Delta W_{Hm-II}] \\
 & + (X^2 - s^2)\left[\frac{W_{II-II}}{4} + (1 - X)\left(\frac{\Delta W_{Hm-II}}{2} + \frac{W_{Hm-II-II}}{4}\right)\right] + (X^2 - s^2)s^2\frac{\Delta^2 W_{II-II}}{4} \quad (119)
 \end{aligned}$$

By inspection of equations (118) and (119) an expression for the vibrational Gibbs free energy of the combined system may be inferred:

$$\begin{aligned}
 G = & (1 - X - Y)\mu_{Hm}^o + X\mu_{II}^o + Y\mu_{Gk}^o \\
 & + \{W_{Hm-II} + [(1 - X - Y) - X]\Delta W_{Hm-II}\}(1 - X - Y)X \\
 & + \{W_{Hm-Gk} + [(1 - X - Y) - Y]\Delta W_{Hm-Gk}\}(1 - X - Y)Y \\
 & + \frac{1}{2}XY(W_{II-Gk} + W_{(II-Gk)^T}) + \frac{1}{2}st(W_{II-Gk} - W_{(II-Gk)^T}) \\
 & + \left[\frac{W_{II-II}}{4} + (1 - X - Y)\left(\frac{1}{2}\Delta W_{Hm-II} + \frac{W_{Hm-II-II}}{4}\right)\right](X^2 - s^2) \\
 & + \left[\frac{W_{Gk-Gk}}{4} + (1 - X - Y)\left(\frac{1}{2}\Delta W_{Hm-Gk} + \frac{W_{Hm-Gk-Gk}}{4}\right)\right](Y^2 - t^2) \\
 & + \frac{\Delta^2 W_{II-II}}{4}(X^2 - s^2)s^2 + \frac{\Delta^2 W_{Gk-Gk}}{4}(Y^2 - t^2)t^2 \quad (120)
 \end{aligned}$$

The new parameters in equation (120), namely W_{Hm-Gk} , ΔW_{Hm-Gk} , W_{Gk-Gk} , $\Delta^2 W_{Gk-Gk}$ and $W_{Hm-Gk-Gk}$, are completely analogous to those for ilmenite. A more rigorous analysis starting from a 4th order expansion and following the energetic symmetry reduction rules developed above verifies equation (120). For the sake of brevity this analysis will not be reported here.

FeTiO₃-MgTiO₃-MnTiO₃-Fe₂O₃-Al₂O₃.—The addition of a pyrophanite component (MnTiO₃) to the model expression for \bar{G}^* follows exactly the steps necessary for the inclusion of geikielite. The addition of corundum (Al₂O₃) is treated analogous to hematite, and for the sake of simplicity, the formation of the ordered compound along the Fe₂O₃-Al₂O₃ join (Muan and Gee, 1956; Majzlan and others, 2002) is ignored. This assumption is justified as long as fictitious excess free energy parameters are chosen for this join that compensate appropriately for the real shape of the energy surface and as long as the model is only used for solid solutions that contain minor concentrations of Al₂O₃. For application to Fe-Ti oxides found in nature, Al₂O₃ concentrations are rarely in excess of 1 or 2 mole percent, and a Henrian description of the excess free energy contribution is adequate.

With the addition of MnTiO₃ and Al₂O₃, equation (120) becomes

$$\begin{aligned}
 \bar{G}^* = & (1 - X - Y - Z - C)\mu_{Hm}^o + X\mu_{Il}^o + Y\mu_{Gk}^o + Z\mu_{Py}^o + C\mu_{Cr}^o \\
 & + \{W_{Hm-II} + [(1 - X - Y - Z - C) - X]\Delta W_{Hm-II}\}(1 - X - Y - Z - C)X \\
 & + \{W_{Hm-Gk} + [(1 - X - Y - Z - C) - Y]\Delta W_{Hm-Gk}\}(1 - X - Y - Z - C)Y \\
 & + \{W_{Hm-Py} + [(1 - X - Y - Z - C) - Z]\Delta W_{Hm-Py}\}(1 - X - Y - Z - C)Z \\
 & + \{W_{Hm-Cr} + [(1 - X - Y - Z - C) - C]\Delta W_{Hm-Cr}\}(1 - X - Y - Z - C)C + \frac{1}{2}XY(W_{Il-Gk} + W_{Il-Gk}) \\
 & + \frac{1}{2}st(W_{Il-Gk} - W_{(Il-Gk)^t}) + \frac{1}{2}XZ(W_{Il-Py} + W_{(Il-Py)^t}) + \frac{1}{2}su(W_{Il-Py} - W_{(Il-Py)^t}) \\
 & + \frac{1}{2}YZ(W_{Gk-Py} + W_{(Gk-Py)^t}) + \frac{1}{2}tu(W_{Gk-Py} - W_{(Gk-Py)^t}) + [W_{Il-Cr} + (X - C)\Delta W_{Il-Cr}]XC \\
 & + [W_{Gk-Cr} + (Y - C)\Delta W_{Gk-Cr}]YC + [W_{Py-Cr} + (Z - C)\Delta W_{Py-Cr}]ZC \\
 & + \left[\frac{W_{Il-II}}{4} + (1 - X - Y - Z - C) \left(\frac{1}{2}\Delta W_{Hm-II} + \frac{W_{Hm-II-Il}}{4} \right) - \frac{1}{2}C\Delta W_{Il-Cr} \right] (X^2 - s^2) \\
 & + \left[\frac{W_{Gk-Gk}}{4} + (1 - X - Y - Z - C) \left(\frac{1}{2}\Delta W_{Hm-Gk} + \frac{W_{Hm-Gk-Gk}}{4} \right) - \frac{1}{2}C\Delta W_{Gk-Cr} \right] (Y^2 - t^2) \\
 & + \left[\frac{W_{Py-Py}}{4} + (1 - X - Y - Z - C) \left(\frac{1}{2}\Delta W_{Hm-Py} + \frac{W_{Hm-Py-Py}}{4} \right) - \frac{1}{2}C\Delta W_{Py-Cr} \right] (Z^2 - u^2) \\
 & + \frac{\Delta^2 W_{Il-II}}{4}(X^2 - s^2)s^2 + \frac{\Delta^2 W_{Gk-Gk}}{4}(Y^2 - t^2)t^2 + \frac{\Delta^2 W_{Py-Py}}{4}(Z^2 - u^2)u^2
 \end{aligned} \tag{121}$$

The expression can be derived rigorously from a 4th order expansion and symmetry analysis, but this somewhat laborious procedure will not be presented here.

Derivatives of the Molar Gibbs Free Energy of Solution in the Supersystem

The long-range configurational entropy in the supersystem that is analogous to equation (11) is given by

$$\begin{aligned}
 -\frac{\bar{S}^{conf}}{R} = & 2(1 - X - Y - Z - C)\ln(1 - X - Y - Z - C) + 2C\ln C + \frac{X+s}{2}\ln\frac{X+s}{2} + \frac{Y+t}{2}\ln\frac{Y+t}{2} \\
 & + \frac{Z+u}{2}\ln\frac{Z+u}{2} + \frac{X-s}{2}\ln\frac{X-s}{2} + \frac{Y-t}{2}\ln\frac{Y-t}{2} + \frac{Z-u}{2}\ln\frac{Z-u}{2} \\
 & + \frac{X+Y+Z-s-t-u}{2}\ln\frac{X+Y+Z-s-t-u}{2} \\
 & + \frac{X+Y+Z+s+t+u}{2}\ln\frac{X+Y+Z+s+t+u}{2}
 \end{aligned} \tag{122}$$

In the high-symmetry phase (that is, the disordered limit), equation (122) reduces to

$$-\frac{\bar{S}^{conf}}{R} = 2(1 - X - Y - Z - C) \ln(1 - X - Y - Z - C) + 2C \ln C + X \ln X + Y \ln Y + Z \ln Z + (X + Y + Z) \ln(X + Y + Z) - 2(X + Y + Z) \ln 2 \quad (123)$$

Equations (122) and (123) may be combined to account for short range order, extending equation (57) to the supersystem

$$\begin{aligned} -\frac{\bar{S}^{conf}}{R} = & \frac{X+s}{2} \ln \frac{X+s}{2} + \frac{X-s}{2} \ln \frac{X-s}{2} - \alpha X \ln \frac{X}{2} + \frac{Y+t}{2} \ln \frac{Y+t}{2} + \frac{Y-t}{2} \ln \frac{Y-t}{2} - \alpha Y \ln \frac{Y}{2} \\ & + \frac{Z+u}{2} \ln \frac{Z+u}{2} + \frac{Z-u}{2} \ln \frac{Z-u}{2} - \alpha Z \ln \frac{Z}{2} + \frac{X+Y+Z-s-t-u}{2} \ln \frac{X+Y+Z-s-t-u}{2} \\ & + \frac{X+Y+Z+s+t+u}{2} \ln \frac{X+Y+Z+s+t+u}{2} - \alpha(X+Y+Z) \ln \left(\frac{X+Y+Z}{2} \right) \\ & + 2(1-\alpha)(1-X-Y-Z-C) \ln(1-X-Y-Z-C) + 2(1-\alpha)C \ln C \end{aligned} \quad (124)$$

From equations (121) and (124), expressions can be developed for the equilibrium state of cation-order:

$$\begin{aligned} \frac{\partial \bar{G}}{\partial s} = 0 = & \frac{RT}{2} \left[\ln \frac{X+s}{X-s} + \ln \frac{X+Y+Z+s+t+u}{X+Y+Z-s-t-u} \right] + \frac{1}{2} t (W_{Il-Gk} - W_{(Il-Gk)r}) \\ & + \frac{1}{2} u (W_{Il-Py} - W_{(Il-Py)r}) - 2s \left[\frac{W_{Il-Il}}{4} + (1-X-Y-Z-C) \left(\frac{1}{2} \Delta W_{Hm-Il} + \frac{W_{Hm-Il-Il}}{4} \right) - \frac{1}{2} C \Delta W_{Il-Cr} \right] \\ & + 2 \frac{\Delta^2 W_{Il-Il}}{4} s (X^2 - 2s^2) \end{aligned} \quad (125)$$

$$\begin{aligned} \frac{\partial \bar{G}}{\partial t} = 0 = & \frac{RT}{2} \left[\ln \frac{Y+t}{Y-t} + \ln \frac{X+Y+Z+s+t+u}{X+Y+Z-s-t-u} \right] + \frac{1}{2} s (W_{Il-Gk} - W_{(Il-Gk)r}) \\ & + \frac{1}{2} u (W_{Gk-Py} - W_{(Gk-Py)r}) - 2t \left[\frac{W_{Gk-Gk}}{4} + (1-X-Y-Z-C) \left(\frac{1}{2} \Delta W_{Hm-Gk} + \frac{W_{Hm-Gk-Gk}}{4} \right) - \frac{1}{2} C \Delta W_{Gk-Cr} \right] \\ & + 2 \frac{\Delta^2 W_{Gk-Gk}}{4} t (Y^2 - 2t^2) \end{aligned} \quad (126)$$

$$\begin{aligned} \frac{\partial \bar{G}}{\partial u} = 0 = & \frac{RT}{2} \left[\ln \frac{Z+u}{Z-u} + \ln \frac{X+Y+Z+s+t+u}{X+Y+Z-s-t-u} \right] + \frac{1}{2} s (W_{Il-Py} - W_{(Il-Py)r}) + \frac{1}{2} t (W_{Gk-Py} - W_{(Gk-Py)r}) \\ & - 2u \left[\frac{W_{Py-Py}}{4} + (1-X-Y-Z-C) \left(\frac{1}{2} \Delta W_{Hm-Py} + \frac{W_{Hm-Py-Py}}{4} \right) - \frac{1}{2} C \Delta W_{Py-Cr} \right] \\ & + 2 \frac{\Delta^2 W_{Py-Py}}{4} u (Z^2 - 2u^2) \end{aligned} \quad (127)$$

all three of which must be satisfied simultaneously at equilibrium.

The chemical potentials of ilmenite, geikielite, pyrophanite, corundum and hematite are given by (Ghiorso, 1990b):

$$\mu_{Il} = \bar{G} + (1-X) \frac{\partial \bar{G}}{\partial X} - Y \frac{\partial \bar{G}}{\partial Y} - Z \frac{\partial \bar{G}}{\partial Z} - C \frac{\partial \bar{G}}{\partial C} - s \frac{\partial \bar{G}}{\partial s} - t \frac{\partial \bar{G}}{\partial t} - u \frac{\partial \bar{G}}{\partial u} \quad (128)$$

$$\mu_{Gk} = \bar{G} - X \frac{\partial \bar{G}}{\partial X} + (1-Y) \frac{\partial \bar{G}}{\partial Y} - Z \frac{\partial \bar{G}}{\partial Z} - C \frac{\partial \bar{G}}{\partial C} - s \frac{\partial \bar{G}}{\partial s} - t \frac{\partial \bar{G}}{\partial t} - u \frac{\partial \bar{G}}{\partial u} \quad (129)$$

$$\mu_{Py} = \bar{G} - X \frac{\partial \bar{G}}{\partial X} - Y \frac{\partial \bar{G}}{\partial Y} + (1-Z) \frac{\partial \bar{G}}{\partial Z} - C \frac{\partial \bar{G}}{\partial C} - s \frac{\partial \bar{G}}{\partial s} - t \frac{\partial \bar{G}}{\partial t} - u \frac{\partial \bar{G}}{\partial u} \quad (130)$$

$$\mu_{Cr} = \bar{G} - X \frac{\partial \bar{G}}{\partial X} - Y \frac{\partial \bar{G}}{\partial Y} - Z \frac{\partial \bar{G}}{\partial Z} + (1 - C) \frac{\partial \bar{G}}{\partial C} - s \frac{\partial \bar{G}}{\partial s} - t \frac{\partial \bar{G}}{\partial t} - u \frac{\partial \bar{G}}{\partial u} \quad (131)$$

$$\mu_{Hm} = \bar{G} - X \frac{\partial \bar{G}}{\partial X} - Y \frac{\partial \bar{G}}{\partial Y} - Z \frac{\partial \bar{G}}{\partial Z} - C \frac{\partial \bar{G}}{\partial C} - s \frac{\partial \bar{G}}{\partial s} - t \frac{\partial \bar{G}}{\partial t} - u \frac{\partial \bar{G}}{\partial u} \quad (132)$$

from which it may be found that the exchange energy, $\mu_{II} - \mu_{Hm}$, is given by $\mu_{II} - \mu_{Hm} = \frac{\partial \bar{G}}{\partial X}$, which for the supersystem is found to be

$$\begin{aligned} \frac{\partial G}{\partial X} = & \mu_{II}^o - \mu_{Hm}^o + RT \left[\begin{aligned} & \frac{1}{2} \ln \frac{X+s}{2} + \frac{1}{2} \ln \frac{X-s}{2} - \alpha \ln \frac{X}{2} \\ & + \frac{1}{2} \ln \frac{X+Y+Z-s-t-u}{2} + \frac{1}{2} \ln \frac{X+Y+Z+s+t+u}{2} \\ & - \alpha \ln \left(\frac{X+Y+Z}{2} \right) - 2(1-\alpha) \ln (1-X-Y-Z-C) \end{aligned} \right] \\ & + \{W_{Hm-II} + [(1-X-Y-Z-C)-X]\Delta W_{Hm-II}\}[(1-X-Y-Z-C)-X] \\ & - 2\Delta W_{Hm-II}(1-X-Y-Z-C)X \\ & - \{W_{Hm-Gk} + [(1-X-Y-Z-C)-Y]\Delta W_{Hm-Gk}\}Y - \Delta W_{Hm-Gk}(1-X-Y-Z-C)Y \\ & - \{W_{Hm-Py} + [(1-X-Y-Z-C)-Z]\Delta W_{Hm-Py}\}Z - \Delta W_{Hm-Py}(1-X-Y-Z-C)Z \\ & - \{W_{Hm-Cr} + [(1-X-Y-Z-C)-C]\Delta W_{Hm-Cr}\}C - \Delta W_{Hm-Cr}(1-X-Y-Z-C)C \\ & + \frac{1}{2} Y(W_{II-Gk} + W_{(II-Gk)^T}) + \frac{1}{2} Z(W_{II-Py} + W_{(II-Py)^T}) + [W_{II-Cr} + (X-C)\Delta W_{II-Cr}]C + \Delta W_{II-Cr}XC \\ & - \left(\frac{1}{2} \Delta W_{Hm-II} + \frac{W_{Hm-II-II}}{4} \right) (X^2 - s^2) + \left[\frac{W_{II-II}}{4} + (1-X-Y-Z-C) \left(\frac{1}{2} \Delta W_{Hm-II} + \frac{W_{Hm-II-II}}{4} \right) \right. \\ & \left. - \frac{1}{2} C \Delta W_{II-Cr} \right] 2X + \frac{\Delta^2 W_{II-II}}{4} 2Xs^2 \end{aligned} \quad (133)$$

The model expression for the chemical potential of hematite in the supersystem is

$$\begin{aligned} \mu_{Hm} = & \mu_{Hm}^o + \{W_{Hm-II} + [3(1-X-Y-Z-C)-X]\Delta W_{Hm-II}\}X(X+Y+Z+C) \\ & + \{W_{Hm-Gk} + [3(1-X-Y-Z-C)-Y]\Delta W_{Hm-Gk}\}Y(X+Y+Z+C) \\ & + \{W_{Hm-Py} + [3(1-X-Y-Z-C)-Z]\Delta W_{Hm-Py}\}Z(X+Y+Z+C) \\ & + \{W_{Hm-Cr} + [3(1-X-Y-Z-C)-C]\Delta W_{Hm-Cr}\}C(X+Y+Z+C) \\ & - \frac{1}{2} XY(W_{II-Gk} + W_{(II-Gk)^T}) - \frac{1}{2} st(W_{II-Gk} - W_{(II-Gk)^T}) - \frac{1}{2} XZ(W_{II-Py} + W_{(II-Py)^T}) \\ & - \frac{1}{2} su(W_{II-Py} - W_{(II-Py)^T}) - \frac{1}{2} YZ(W_{Gk-Py} + W_{(Gk-Py)^T}) - \frac{1}{2} tu(W_{Gk-Py} - W_{(Gk-Py)^T}) \\ & - [W_{II-Cr} + 2(X-C)\Delta W_{II-Cr}]XC - [W_{Gk-Cr} + 2(Y-C)\Delta W_{Gk-Cr}]YC - [W_{Py-Cr} + 2(Z-C)\Delta W_{Py-Cr}]ZC \\ & - \left[\frac{W_{II-II}}{4} + (1-X-Y-Z-C) \left(\frac{1}{2} \Delta W_{Hm-II} + \frac{W_{Hm-II-II}}{4} \right) - \frac{1}{2} C \Delta W_{II-Cr} \right] (X^2 - s^2) \\ & + \left(\frac{1}{2} \Delta W_{Hm-II} + \frac{W_{Hm-II-II}}{4} \right) (X+Y+Z+C)(X^2 - s^2) - \frac{1}{2} \Delta W_{II-Cr}C(X^2 - s^2) \\ & - \left[\frac{W_{Gk-Gk}}{4} + (1-X-Y-Z-C) \left(\frac{1}{2} \Delta W_{Hm-Gk} + \frac{W_{Hm-Gk-Gk}}{4} \right) - \frac{1}{2} C \Delta W_{Gk-Cr} \right] (Y^2 - t^2) \\ & + \left(\frac{1}{2} \Delta W_{Hm-Gk} + \frac{W_{Hm-Gk-Gk}}{4} \right) (X+Y+Z+C)(Y^2 - t^2) - \frac{1}{2} C \Delta W_{Gk-Cr}(Y^2 - t^2) \end{aligned}$$

$$\begin{aligned}
 & - \left[\frac{W_{Py-Py}}{4} + (1 - X - Y - Z - C) \left(\frac{1}{2} \Delta W_{Hm-Py} + \frac{W_{Hm-Py-Py}}{4} \right) - \frac{1}{2} C \Delta W_{Py-Cr} \right] (Z^2 - u^2) \\
 & + \left(\frac{1}{2} \Delta W_{Hm-Py} + \frac{W_{Hm-Py-Py}}{4} \right) (X + Y + Z + C) (Z^2 - u^2) - \frac{1}{2} C \Delta W_{Py-Cr} (Z^2 - u^2) \\
 & - 3 \frac{\Delta^2 W_{Hm-Hm}}{4} (X^2 - s^2) s^2 - 3 \frac{\Delta^2 W_{Gk-Gk}}{4} (Y^2 - t^2) t^2 - 3 \frac{\Delta^2 W_{Py-Py}}{4} (Z^2 - u^2) u^2
 \end{aligned} \quad (134)$$

Heat Capacity of Ulvöspinel (Fe_2TiO_4)

In their calibration of the Fe-Ti oxide geothermometer/oxygen barometer, Ghiorso and Sack (1991) adopted an expression for the isobaric heat capacity (C_p) of ulvöspinel from Berman and Brown (1985). This expression is of the form

$$C_p = k_0 + \frac{k_1}{\sqrt{T}} + \frac{k_2}{T^2} + \frac{k_3}{T^3} \quad (135)$$

and was parameterized (by Berman and Brown, 1985) from high-temperature heat content data reported by Bonnickson (1955) and low-temperature adiabatic calorimetry data reported by Todd and King (1953). Robie and others (1995) also fitted these same experimental results with an equation of different form,

$$C_p = A_1 + A_2 T + \frac{A_3}{T^2} + \frac{A_4}{\sqrt{T}} + A_5 T^2 \quad (136)$$

and obtained a superior calibration, particularly at temperatures in excess of 1000 K, where the expression of Berman and Brown (1985) underestimates the heat content data of Bonnickson (1955) by as much as 3 kJ/mol. The underlying source of the misfit is the anomalous curvature of the heat content data of ulvöspinel in reference to other titanates (Fe_2TiO_5 , Al_2TiO_5 , and Zn_2TiO_4 , Bonnickson, 1955). Bonnickson's (1955) own parameterization of the data, which adopts a Meyer-Kelly form for the C_p expression, also failed to account for this anomalous behavior; he speculated that the origin may be related to disordering of Ti^{4+} or to additional electronic terms arising from Fe^{2+} at elevated T . Significantly, the anomaly is not seen in magnetite (Fe_3O_4). Regardless of the origin of the anomaly, some accounting must be made in order to correctly calculate the temperature dependence of the standard state properties of ulvöspinel.

For reasons of stability in extrapolation to elevated T the heat capacity form of equation (135) is preferred. Berman and Brown (1985) provide a means of parameterizing anomalous contributions to the heat capacity by extending their expression with a so-called lambda-term:

$$\left. \begin{aligned} C_p &= k_0 + \frac{k_1}{\sqrt{T}} + \frac{k_2}{T^2} + \frac{k_3}{T^3} + T(l_1 + l_2 T)^2 & T \leq T_\lambda \\ C_p &= k_0 + \frac{k_1}{\sqrt{T}} + \frac{k_2}{T^2} + \frac{k_3}{T^3} & T > T_\lambda \end{aligned} \right\} \quad (137)$$

In equation (137) T_λ is the maximum temperature exhibited by the anomalous behavior. As the C_p expression of Berman and Brown (1985) reproduces the data of Bonnickson (1955) at temperatures below 800 K, numerical values for the parameters k_0 , k_1 , k_2 , and k_3 are adopted from their analysis. Values for l_1 and l_2 are fitted from central difference numerical derivatives of Bonnickson's (1955) heat content data, assuming T_λ is above the highest temperature reported. The result of this analysis gives the following expression for the heat capacity of ulvöspinel:

$$C_p = 249.63 - \frac{1817.4}{\sqrt{T}} - \frac{5.453 \times 10^7}{T^3} + T(-0.039452 + 7.54197 \times 10^{-5} T)^2 \quad (138)$$

Data recovery is illustrated in figure 32.

Higher Order Compositional Derivatives of the Gibbs Free Energy in the System $FeTiO_3-Fe_2O_3$

The first compositional derivative of the molar Gibbs free energy is obtained from the formal definition of the total derivative,

$$d\bar{G} = \frac{\partial \bar{G}}{\partial X} dX + \frac{\partial \bar{G}}{\partial s} ds \quad (139)$$

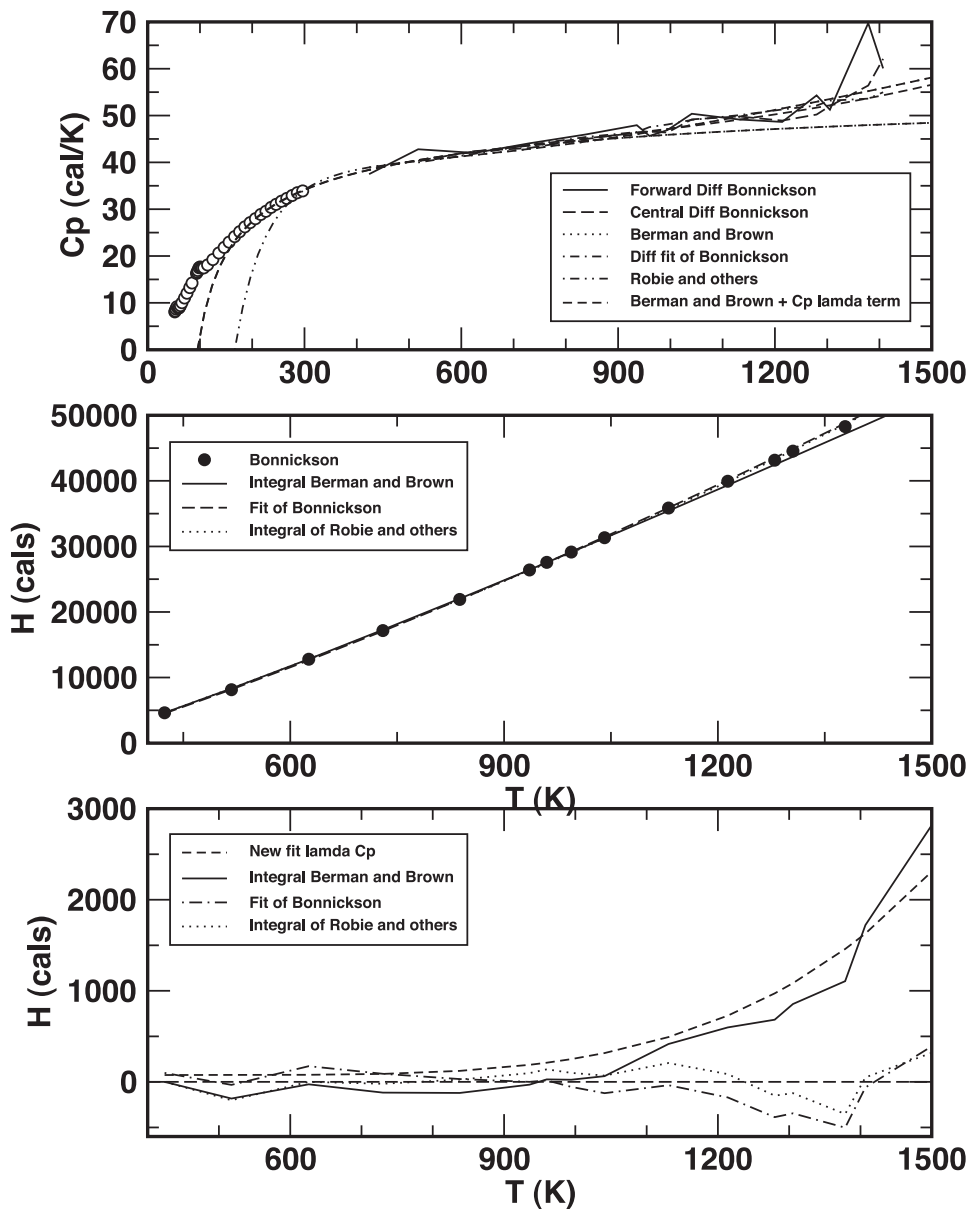


Fig. 32. Analysis of the high-temperature heat content data of Bonnickson (1955) for Fe_2TiO_4 (ulvöspinel). Comparison is made between measurements and the parameterizations of Berman and Brown (1985) and Robie and Hemingway (1995). A revised model fit is given by (138). *Top Panel:* Modeled isobaric heat capacity (C_p) plotted as a function of temperature (K). *Middle Panel:* Measured heat contents compared to model curves. *Lower Panel:* Solid curves are residuals between model C_p expressions and the data of Bonnickson (1955). Dashed curve shows the fit to the Berman and Brown (1985) residuals, which yields the “lambda” term of the preferred model.

from which

$$\frac{d\bar{G}}{dX} = \frac{\partial \bar{G}}{\partial X} + \frac{\partial \bar{G}}{\partial s} \frac{ds}{dX} \quad (140)$$

In a state of equilibrium cation-order (denoted by *eq*), the partial derivative $\frac{\partial \bar{G}}{\partial s}$ is zero by definition, consequently

$$\left. \frac{d\bar{G}}{dX} \right|_{eq} = \frac{\partial \bar{G}}{\partial X} \quad (141)$$

The second compositional derivative is obtained from the first by again forming the total derivative

$$d\left(\frac{d\bar{G}}{dX}\right)_{eq} = \frac{\partial^2 \bar{G}}{\partial X^2} dX + \frac{\partial^2 \bar{G}}{\partial X \partial s} ds \quad (142)$$

from which

$$\left. \frac{d^2 \bar{G}}{dX^2} \right|_{eq} = \frac{\partial^2 \bar{G}}{\partial X^2} + \left. \frac{\partial^2 \bar{G}}{\partial X \partial s} \frac{ds}{dX} \right|_{eq} \quad (143)$$

Although $\frac{\partial \bar{G}}{\partial s}$ is zero in a state of equilibrium cation-order, $\frac{\partial^2 \bar{G}}{\partial X \partial s}$ is not necessarily so. Therefore, the equilibrium variation of *s* with respect to *X* must be determined. This variation is constrained by

$$d \frac{\partial \bar{G}}{\partial s} = 0 = \frac{\partial^2 \bar{G}}{\partial X \partial s} dX + \frac{\partial^2 \bar{G}}{\partial s^2} ds \quad (144)$$

from which

$$\left. \frac{ds}{dX} \right|_{eq} = - \frac{\partial^2 \bar{G}}{\partial X \partial s} / \frac{\partial^2 \bar{G}}{\partial s^2} \quad (145)$$

Consequently,

$$\left. \frac{d^2 \bar{G}}{dX^2} \right|_{eq} = \frac{\partial^2 \bar{G}}{\partial X^2} + \left. \frac{\partial^2 \bar{G}}{\partial X \partial s} \frac{ds}{dX} \right|_{eq} = \frac{\partial^2 \bar{G}}{\partial X^2} - \left(\frac{\partial^2 \bar{G}}{\partial X \partial s} \right)^2 / \frac{\partial^2 \bar{G}}{\partial s^2} \quad (146)$$

Following a similar line of argument, the third derivative is obtained from

$$\left. \frac{d^3 \bar{G}}{dX^3} \right|_{eq} = \frac{\partial^3 \bar{G}}{\partial X^3} + 2 \left. \frac{\partial^3 \bar{G}}{\partial X^2 \partial s} \frac{ds}{dX} \right|_{eq} + \frac{\partial^3 \bar{G}}{\partial X \partial s^2} \left(\left. \frac{ds}{dX} \right|_{eq} \right)^2 + \frac{\partial^2 \bar{G}}{\partial X \partial s} \frac{d^2 s}{dX^2} \Big|_{eq} \quad (147)$$

The quantity $\left. \frac{d^2 s}{dX^2} \right|_{eq}$ is obtained from differentiation of equation (145)

$$\left. \frac{d^2 s}{dX^2} \right|_{eq} = - \frac{\frac{\partial^2 \bar{G}}{\partial s^2} \left(\frac{\partial^3 \bar{G}}{\partial X^2 \partial s} + \frac{\partial^3 \bar{G}}{\partial X \partial s^2} \frac{ds}{dX} \Big|_{eq} \right)}{\left(\frac{\partial^2 \bar{G}}{\partial s^2} \right)^2} - \frac{\partial^2 \bar{G}}{\partial X \partial s} \left(\frac{\partial^3 \bar{G}}{\partial X \partial s^2} + \frac{\partial^3 \bar{G}}{\partial s^3} \frac{ds}{dX} \Big|_{eq} \right) \quad (148)$$

Substitution of equation (145) into equation (148) gives

$$\left. \frac{d^2 s}{dX^2} \right|_{eq} = - \frac{\partial^3 \bar{G}}{\partial X^2 \partial s} / \frac{\partial^2 \bar{G}}{\partial s^2} + 2 \frac{\partial^3 \bar{G}}{\partial X \partial s^2} \frac{\partial^2 \bar{G}}{\partial X \partial s} / \left(\frac{\partial^2 \bar{G}}{\partial s^2} \right)^2 - \frac{\partial^3 \bar{G}}{\partial s^3} \left(\frac{\partial^2 \bar{G}}{\partial X \partial s} \right)^2 / \left(\frac{\partial^2 \bar{G}}{\partial s^2} \right)^3 \quad (149)$$

Substitution of both equations (145) and (149) into equation (147) gives

$$\left. \frac{d^3 \bar{G}}{dX^3} \right|_{eq} = \frac{\partial^3 \bar{G}}{\partial X^3} - 3 \frac{\partial^3 \bar{G}}{\partial X^2 \partial s} \frac{\partial^2 \bar{G}}{\partial X \partial s} / \frac{\partial^2 \bar{G}}{\partial s^2} + 3 \frac{\partial^3 \bar{G}}{\partial X \partial s^2} \left(\frac{\partial^2 \bar{G}}{\partial X \partial s} / \frac{\partial^2 \bar{G}}{\partial s^2} \right)^2 - \frac{\partial^3 \bar{G}}{\partial s^3} \left(\frac{\partial^2 \bar{G}}{\partial X \partial s} / \frac{\partial^2 \bar{G}}{\partial s^2} \right)^3 \quad (150)$$

REFERENCES

- Ague, J. J., Baxter, E. F., and Eckert, J. O., Jr., 2001, High f_{O_2} during sillimanite zone metamorphism of part of the Barrovian type locality, Glen Clova, Scotland: *Journal of Petrology*, v. 42, p. 1301–1320, doi:10.1093/petrology/42.7.1301.
- Andersen, D. J., and Lindsley, D. H., 1979, The olivine-ilmenite thermometer, in *Proceedings of the 10th Lunar and Planetary Science Conference*, March 19–23, 1979, Houston, Texas: New York, Pergamon Press, Inc., p. 493–507.
- , 1988, Internally consistent solution models for Fe-Mg-Mn-Ti oxides: Fe-Ti oxides: *American Mineralogist*, v. 73, p. 714–726.
- Anderson, A. T., Davis, A. M., and Lu, F. Q., 2000, Evolution of Bishop Tuff rhyolitic magma based on melt and magnetite inclusions and zoned phenocrysts: *Journal of Petrology*, v. 41, p. 449–473, doi:10.1093/petrology/41.3.449.
- Bacon, C. R., and Hirschmann, M. M., 1988, Mg/Mn partitioning as a test for equilibrium between Fe-Ti oxides: *American Mineralogist*, v. 73, p. 57–61.
- Berman, R. G., 1988, Internally-consistent thermodynamic data for minerals in the system $\text{Na}_2\text{O}-\text{K}_2\text{O}-\text{CaO}-\text{MgO}-\text{FeO}-\text{Fe}_2\text{O}_3-\text{Al}_2\text{O}_3-\text{SiO}_2-\text{TiO}_2-\text{H}_2\text{O}-\text{CO}_2$: *Journal of Petrology*, v. 29, p. 445–522.
- Berman, R. G., and Brown, T. H., 1985, Heat capacity of minerals in the system $\text{Na}_2\text{O}-\text{K}_2\text{O}-\text{CaO}-\text{MgO}-\text{FeO}-\text{Fe}_2\text{O}_3-\text{Al}_2\text{O}_3-\text{SiO}_2-\text{TiO}_2-\text{H}_2\text{O}-\text{CO}_2$: *Contributions to Mineralogy and Petrology*, v. 89, p. 168–183, doi:10.1007/BF00379451.
- Bernadt, J., Koepke, J., and Holz, F., 2005, An experimental investigation of the influence of water and oxygen fugacity on differentiation of MORB at 200 MPa: *Journal of Petrology*, v. 46, p. 135–167, doi:10.1093/petrology/egh066.
- Bina, M., Tanguy, J. C., Hoffman, V., Prévot, M., Listanco, E. L., Keller, R., Fehr, K. Th., Goguitchaichvili, A. T., and Punongbayan, R. S., 1999, A detailed magnetic and mineralogical study of self-reversed dacite pumices from the 1991 Pinatubo eruption (Philippines): *Geophysical Journal International*, v. 138, p. 159–178, doi:10.1046/j.1365-246x.1999.00865.x.
- Bonnickson, K. R., 1955, High temperature heat contents of some titanates of aluminum, iron and zinc: *Journal of the American Chemical Society*, v. 77, p. 2152–2154, doi:10.1021/ja01613a033.
- Brown, N. E., and Navrotsky, A., 1994, Hematite-ilmenite ($\text{Fe}_2\text{O}_3-\text{FeTiO}_3$) solid solutions: The effects of cation ordering on the thermodynamics of mixing: *American Mineralogist*, v. 79, p. 485–496.
- Buddington, A. F., and Lindsley, D. H., 1964, Iron-titanium oxide minerals and synthetic equivalents: *Journal of Petrology*, v. 5, p. 310–357.
- Burton, B. P., ms, 1982, Thermodynamic analysis of the systems calcium carbonate—magnesium carbonate, alpha—ferric oxide, and ferric oxide—ferrous titanate: Stony Brook, New York, State University of New York, Ph. D. thesis, 170 p.
- , 1984, Thermodynamic analysis of the system $\text{Fe}_2\text{O}_3-\text{FeTiO}_3$: *Physics and Chemistry of Minerals*, v. 11, p. 132–139, doi:10.1007/BF00309251.
- Burton, B., and Davidson, P. M., 1988, Multicritical phase relations in minerals, in Ghose, S., Coey, J. M. D., and Salje, E., editors, *Structural and Magnetic Phase Transitions in Minerals: Advances in Physical Geochemistry*, v. 7, p. 60–90.
- Burton, B., and Kikuchi, R., 1984, The antiferromagnetic-paramagnetic transition in $\alpha\text{Fe}_2\text{O}_3$ in the single prism approximation of the cluster variation method: *Physics and Chemistry of Minerals*, v. 11, p. 125–131, doi:10.1007/BF00309250.
- Burton, B. P., Chaka, A., and Singh, D. J., 2005, Chemical, magnetic and charge ordering in the system hematite-ilmenite, $\text{Fe}_2\text{O}_3-\text{FeTiO}_3$: *Phase Transitions*, v. 78, p. 239–249, doi:10.1080/01411590412331316555.
- Carmichael, I. S. E., 1967, The iron-titanium oxides of saline volcanic rocks and their associated ferromagnetic silicates: *Contributions to Mineralogy and Petrology*, v. 14, p. 36–64, doi:10.1007/BF00370985.
- Core, D. P., Essene, E. J., and Luhr, J. F., 2003, Oxide equilibria in calc-alkaline magmas at high oxygen fugacity: *Geological Society of America Abstracts with Programs*, v. 35, p. 393–394.
- Ebad, A., and Johanns, W., 1991, Beginning of melting and composition of first melts in the system $\text{Qz}-\text{Ab}-\text{Or}-\text{H}_2\text{O}-\text{CO}_2$: *Contributions to Mineralogy and Petrology*, v. 106, p. 286–295, doi:10.1007/BF00324558.
- Evans, B. W., and Ghiorso, M. S., 1995, Thermodynamics and petrology of cummingtonite: *American Mineralogist*, v. 80, p. 649–663.
- Evans, B. W., and Scaillet, B., 1997, The redox state of Pinatubo dacite and the ilmenite-hematite solvus: *American Mineralogist*, v. 82, p. 625–629.
- Evans, B. W., Scaillet, B., and Kuehner, S. M., 2006, Experimental determination of co-existing iron-titanium oxides in the systems FeTiAlO , FeTiAlMgO , FeTiAlMnO , and FeTiAlMgMnO at 800 and 900° C, 1–4 kbar, and relatively high oxygen fugacity: *Contributions to Mineralogy and Petrology*, v. 152, p. 149–167, doi:10.1007/s00410-006-0098-z.
- , 2007, Take dacite, add fire and brimstone, get peraluminous: *Abstracts of the sixth annual Hutton Symposium on the Origin of Granitic Rocks*, July 2, 2007–July 6, 2007, University of Stellenbosch, South Africa.
- Frost, B. R., Lindsley, D. H., and Andersen, D. J., 1988, Fe-Ti oxide-silicate equilibria; Assemblages with fayalitic olivine: *American Mineralogist*, v. 73, p. 727–740.
- Gardner, J. E., Rutherford, M., Carey, S., and Sigurdsson, H., 1995a, Experimental constraints on pre-eruptive water contents and changing magma storage prior to explosive eruption of Mount St. Helens volcano: *Bulletin of Volcanology*, v. 57, p. 1–17, doi:10.1007/s004450050073.
- Gardner, J. R., Carey, S., and Rutherford, M., 1995b, Petrologic diversity in Mount St. Helens dacites during

- the last 4,000 years: implications for magma mixing: Contributions to Mineralogy and Petrology, v. 119, p. 224–238, doi:10.1007/BF00307283.
- Geschwind, C.-H., and Rutherford, M. J., 1992, Cummingtonite and the evolution of the Mount St. Helens (Washington) magma system: An experimental study: Geology, v. 20, p. 1011–1014, doi:10.1130/0091-7613(1992)020<1011:CATEOT>2.3.CO;2.
- Ghiorso, M. S., 1990a, Thermodynamic properties of hematite-ilmenite-geikielite solid solutions: Contributions to Mineralogy and Petrology, v. 104, p. 645–667, doi:10.1007/BF01167285.
- , 1990b, A note on the application of the Darken equation to mineral solid solutions with variable degrees of order-disorder: American Mineralogist, v. 75, p. 539–543.
- , 1997, Thermodynamic analysis of the effect of magnetic ordering on miscibility gaps in the Fe-Ti cubic and rhombohedral oxide minerals and the Fe-Ti oxide geothermometer: Physics and Chemistry of Minerals, v. 25, p. 28–38, doi:10.1007/s002690050083.
- Ghiorso, M. S., and Evans, B. W., 2002, Thermodynamics of the amphiboles: Ca-Mg-Fe²⁺ Quadrilateral: American Mineralogist, v. 87, p. 79–98.
- Ghiorso, M. S., and Sack, R. O., 1991, Fe-Ti oxide geothermometry: thermodynamic formulation and the estimation of intensive variables in silicic magmas: Contributions to Mineralogy and Petrology, v. 108, p. 485–510, doi:10.1007/BF00303452.
- Gualda, G. A. R., ms, 2007, Crystal and bubble populations in the early-erupted Bishop rhyolitic magma: Microscopy, X-ray tomography, and microanalysis of pumice clasts: Chicago, Illinois, University of Chicago, Ph. D. thesis, University of Chicago, 267 p.
- Haag, M., Heller, F., Allenspach, R., and Roche, K., 1990a, Self-reversal of natural remanent magnetization in andesitic pumice: Physics of the Earth and Planetary Interiors, v. 65, p. 104–108, doi:10.1016/0031-9201(90)90079-D.
- Haag, M., Heller, F., Carracedo, J. C., and Soler, V., 1990b, Remanent magnetization of andesitic and dacitic pumice from the 1985 eruption of Nevado del Ruiz (Colombia) reversed due to self-reversal: Journal of Volcanology and Geothermal Researches, v. 41, p. 369–377, doi:10.1016/0377-0273(90)90097-Y.
- Harrison, R. J., 2006, Microstructure and magnetism in the ilmenite-hematite solid solution: A Monte Carlo simulation study: American Mineralogist, v. 91, p. 1006–1023, doi:10.2138/am.2006.2008.
- Harrison, R. J., and Redfern, S. A. T., 2001, Short- and long-range ordering in the ilmenite-hematite solid solution: Physics and Chemistry of Minerals, v. 28, p. 399–412, doi:10.1007/s002690100167.
- Harrison, R. J., Redfern, S. A. T., and Smith, R. I., 2000a, In-situ study of the R̄3 to R̄3c phase transition in the ilmenite-hematite solid solution using time-of-flight neutron powder diffraction: American Mineralogist, v. 85, p. 194–205.
- Harrison, R. J., Becker, U., and Redfern, S. A. T., 2000b, Thermodynamics of the R̄3 to R̄3c phase transition in the ilmenite-hematite solid solution: American Mineralogist, v. 85, p. 1694–1705.
- Harrison, R. J., Kasama, T., White, T. A., Simpson, E. T., and Dunin-Borkowski, R. E., 2005, Origin of self-reversed thermoremanent magnetization: Physical Review Letters, v. 95, 268501-1/4.
- Harrison, R. J., Stone, H. J., and Redfern, S. A. T., 2006, Pressure dependence of Fe-Ti order in the ilmenite-hematite solid solution: Implications for the origin of lower crustal magnetization: Physics of the Earth and Planetary Interiors, v. 154, p. 266–275, doi:10.1016/j.pepi.2005.04.016.
- Hattori, K., 1996, Occurrence and origin of sulfide and sulfate in the 1991 Mount Pinatubo eruption products, in Newhall, C. G., and Punongbayan, R. S., editors, Fire and Mud: Eruptions and Lahars of Mount Pinatubo, Philippines: Seattle, Washington, University of Washington Press and the Philippine Institute of Volcanology and Seismology, Quezon City, 1126 p.
- Hildreth, W., ms, 1977, The magma chamber of the Bishop Tuff: Gradients, temperature, pressure and composition: Berkeley, California, University of California, Ph. D. thesis, 328 p.
- Hildreth, W., 1979, The Bishop Tuff: Evidence for the origin of compositional zonation in silicic magma bodies: Geological Society of America Special Paper, v. 180, p. 43–75.
- Hildreth, W., and Wilson, C. J. N., 2007, Compositional zoning of the Bishop Tuff: Journal of Petrology, v. 48, p. 951–999, doi:10.1093/petrology/egm007.
- Hoffmann, V., and Fehr, K. Th., 1996, Micromagnetic, rockmagnetic and mineralogical studies on dacite pumice from the Pinatubo eruption (1991, Philippines) showing self-reversed TRM: Geophysical Research Letters, v. 23, no. 20, p. 2835–2838, doi:10.1029/96GL01317.
- Holland, T., and Powell, R., 2001, Calculation of Phase Relations Involving Haplogranitic Melts Using an Internally Consistent Thermodynamic Dataset: Journal of Petrology, v. 42, p. 673–683, doi:10.1093/petrology/42.4.673.
- Imai, A., Listanco, E. L., and Fujii, T., 1996, Highly Oxidized and Sulfur-Rich Dacitic Magma of Mount Pinatubo: Implication for Metallogenesis of Porphyry Copper Mineralization in the Western Luzon Arc, in Newhall, C. G., and Punongbayan, R. S., editors, Fire and Mud: Eruptions and Lahars of Mount Pinatubo, Philippines: Seattle, Washington, University of Washington and the Philippine Institute of Volcanology and Seismology, 1126 p.
- Ishikawa, Y., 1958, An order-disorder transformation phenomena in the FeTiO₃-Fe₂O₃ solid solution series: Journal of the Physical Society of Japan, v. 13, p. 828–837, doi:10.1143/JPSJ.13.828.
- Kennedy, L. P., and Osborne, M. D., 1987, Composite titanomagnetite-ferrian ilmenite grains and correlative magnetic components in a dacite with self-reversed TRM: Earth and Planetary Science Letters, v. 84, p. 479–486, doi:10.1016/0012-821X(87)90012-4.
- Lattard, D., Sauerzapf, U., and Käsemann, M., 2005, New calibration data for the Fe-Ti oxide thermo-oxybarometers from experiments in the Fe-Ti-O system at 1 bar, 1,000–1,300°C and a large range of oxygen fugacities: Contributions to Mineralogy and Petrology, v. 149, p. 735–754, doi:10.1007/s00410-005-0679-2.

- Lawson, C. A., Nord, G. L., Jr., and Champion, D. E., 1987, Fe-Tioxide mineralogy and the origin of normal and reverse remanent magnetization in dacite pumice blocks from Mt. Shasta (California): Physics of the Earth and Planetary Interiors, v. 46, p. 270–288, doi:10.1016/0031-9201(87)90190-7.
- Lerbekmo, J. F., Westgate, J. A., Smith, D. W. G., and Denton, G. H., 1975, New data on the character and history of the White River volcanic eruption, Alaska, in Suggate, R. P., and Cresswell, M. M., editors, Quaternary Studies: The Royal Society of New Zealand, p. 203–209.
- Lindsley, D. H., 1973, Delimitation of the hematite-ilmenite miscibility gap: Geological Society of America Bulletin, v. 84, p. 657–662, doi:10.1130/0016-7606(1973)84<657:DOTHMG>2.0.CO;2.
- Lindsley, D. H., Frost, B. R., Andersen, D. J., and Davidson, P. M., 1990, Fe-Ti oxide-silicate equilibria: Assemblages with orthopyroxene, in Spencer, R. J., and Chou, I-M., editors, Fluid-Mineral Interactions: A tribute to H. P. Eugster: Geochemical Society Special Publication, v. 2, p. 103–119.
- Lucchesi, S., Russo, U., and DellaGiusta, A., 1997, Crystal chemistry and cation distribution in some Mn-rich natural and synthetic spinels: European Journal of Mineralogy, v. 9, p. 31–42.
- Luhr, J. F., 1990, Experimental phase relations of water- and sulfur-saturated arc magmas and the 1982 eruptions of El Chichón Volcano: Journal of Petrology, v. 31, p. 1071–1114, doi:10.1093/petrology/31.5.1071.
- Majzlan, J., Navrotsky, A., and Evans, B. J., 2002, Thermodynamics and crystal chemistry of the hematite-corundum solid solution and the FeAlO_3 phase: Physics and Chemistry of Minerals, v. 29, p. 515–526, doi:10.1007/s00269-002-0261-7.
- Martel, C., Pichavant, M., Holz, F., Scaillet, B., Bourdier, J-L., and Trainea, H., 1999, Effects of f_{O_2} and H_2O on andesite phase relations between 2 and 4 kbar: Journal of Geophysical Research, v. 104, no. B12, p. 29,453–29,470.
- Muan, A., and Gee, C. L., 1956, Phase equilibrium studies in the system iron oxide— Al_2O_3 in air and at 1 atm. O_2 pressure: Journal of the American Ceramic Society, v. 39, p. 207–215, doi:10.1111/j.1151-2916.1956.tb15647.x.
- Nicholls, I. A., Oba, T., and Conrad, W. K., 1992, The nature of primary rhyolitic magmas involved in crustal evolution: Evidence from an experimental study of cummingtonite-bearing rhyolites, Taupo Volcanic Zone, New Zealand: Geochimica et Cosmochimica Acta, v. 56, p. 955–962, doi:10.1016/0016-7037(92)90039-L.
- Nord, G. L., and Lawson, C. A., 1989, Order-disorder transition-induced twin domains and magnetic properties in ilmenite-hematite: American Mineralogist, v. 74, p. 160–176.
- Nord, G. L., Jr., and Lawson, C. A., 1992, Magnetic properties of ilmenite₇₀-hematite₃₀: Effect of transformation-induced twin-boundaries: Journal of Geophysical Research, v. 97, No. B7, p. 10897–10910, doi:10.1029/91JB02259.
- Oba, T., and Nicholls, I. A., 1986, Experimental study of cummingtonite and Ca-Na amphibole relations in the system Cum-Act-Pl-Qz- H_2O : American Mineralogist, v. 71, p. 1354–1365.
- O'Neill, H. St.C., and Pownceby, M. L., 1993, Thermodynamic data from redox reactions at high temperatures. I. An experimental and theoretical assessment of the electro-chemical method using stabilized zirconia electrolytes, with revised values for the Fe-“FeO”, Co-CoO, Ni-NiO, and Cu-Cu₂O oxygen buffers, and new data for the W-WO₂ buffer: Contributions to Mineralogy and Petrology, v. 114, p. 296–314, doi:10.1007/BF01046533.
- O'Neill, H. St. C., Pownceby, M. L., and Wall, V. J., 1989, Activity-composition relations in $\text{FeTiO}_3\text{-MnTiO}_3$ ilmenite solid solutions from EMF measurements at 1050–1300 K: Contributions to Mineralogy and Petrology, v. 103, p. 216–222, doi:10.1007/BF00378507.
- Ozima, M., Funaki, M., Hamada, N., Aramaki, S., and Fuji, T., 1992, Self-reversal of thermo-remanent magnetization in pyroclastic from the 1991 eruption of Mt. Pinatubo, Philippines: Journal of Geomagnetism and Geoelectricity, v. 44, p. 979–984.
- Pallister, J. S., Hoblitt, R. P., Meeker, G. P., Knight, R. J., and Siems, D. F., 1996, Magma Mixing at Mount Pinatubo: Petrographic and Chemical Evidence from the 1991 Deposits, in Newhall, C. G., and Punongbayan, R. S., editors, Fire and Mud: Eruptions and Lahars of Mount Pinatubo, Philippines: Philippine Institute of Volcanology and Seismology and the University of Washington, Seattle, 1126 p.
- Pownceby, M. L., and Fisher-White, M. J., 1999, Phase equilibria in the systems $\text{Fe}_3\text{O}_4\text{-MgO-TiO}_2$ and FeO-MgO-TiO_2 between 1173 and 1473 K, and $\text{Fe}^{2+}\text{-Mg}$ mixing properties of ilmenite, ferrous-pseudobrookite and ulvöspinel solid solutions: Contributions to Mineralogy and Petrology, v. 135, p. 198–211, doi:10.1007/s004100050506.
- Prigogine, I., and Defay, R., 1954, Chemical Thermodynamics: New York, Longmans, Green and Co., 543 p.
- Prouteau, G., and Scaillet, B., 2003, Experimental constraints on the origin of the 1991 Pinatubo dacite: Journal of Petrology, v. 44, p. 2203–2241, doi:10.1093/petrology/egg075.
- Robie, R. A., and Hemingway, B. S., 1995, Thermodynamic properties of minerals and related substances at 298.15 K and 1 Bar (10^5 Pascals) pressure and at high temperatures: United States Geological Survey Bulletin No. 2131, 461 p.
- Ruprecht, P., Bergantz, G. W., and Dufek, J., 2008, Modeling gas-driven magmatic over-turn: Tracking of phenocryst dispersal and gathering during magma mixing: Geochemistry, Geophysics, Geosystems, v. 9, Q07017, doi:10.1029/2008GC002022, 2008.
- Rutherford, M. J., and Devine, J. D., 1996, Preeruption pressure-temperature conditions and volatiles in the 1991 dacitic magma of Mount Pinatubo, in Newhall, C. G., and Punongbayan, R. S., editors, Fire and Mud: Eruptions and Lahars of Mount Pinatubo, Philippines: Philippine Institute of Volcanology and Seismology and the University of Washington, Seattle, 1126 p.
- Sack, R. O., and Ghiorso, M. S., 1991a, An internally consistent solution model for the thermodynamic properties of Fe-Mg-titanomagnetite-aluminite spinels: Contributions to Mineralogy and Petrology, v. 106, p. 474–505, doi:10.1007/BF00321989.

- 1991b, Chromium spinels as petrogenetic indicators: thermodynamics and a petrologic application: American Mineralogist, v. 76, p. 827–847.
- Scaillet, B., and Evans, B. W., 1999, The 15 June 1991 eruption of Mount Pinatubo. I. Phase equilibria and pre-eruption P - T - fO_2 - H_2O conditions of the dacite magma: Journal of Petrology, v. 40, p. 381–411, doi:10.1093/petrology/40.3.381.
- Scaillet, B., and MacDonald, R., 2001, Phase relations of peralkaline silicic magmas and petrogenetic implications: Journal of Petrology, v. 42, p. 825–845, doi:10.1093/petrology/42.4.825.
- Todd, S. S., and King, E. G., 1953, Heat capacities at low temperatures and entropies at 298.16° K. of titanomagnetic and ferric titanate: Journal of the American Chemical Society, v. 75, p. 4547–4549, doi:10.1021/ja01114a047.
- Toplis, M. J., and Carroll, M. R., 1995, An experimental study of the influence of oxygen fugacity on Fe-Ti oxide stability, phase relations, and mineral-melt equilibria in ferro-basaltic systems: Journal of Petrology, v. 36, p. 1137–1170, doi:10.1093/petrology/36.5.1137.
- Tuttle, O. F., and Bowen, N. L., 1958, Origin of granite in the light of experimental studies in the system NaAlSi₃O₈-KAlSi₃O₈-SiO₂-H₂O: Geological Society of America Memoir, v. 74, 153 p.
- Wark, D. A., and Watson, E. B., 2006, TitaniQ, a titanium-in-quartz geothermometer: Contributions to Mineralogy and Petrology, v. 152, p. 743–754, doi:10.1007/s00410-006-0132-1.
- Wark, D. A., Hildreth, W., Spear, F. S., Cherniak, D. J., and Watson, E. B., 2007, Pre-eruption recharge of the Bishop magma system: Geology, v. 35, p. 235–238, doi:10.1130/G23316A.1.
- Wood, B. E., and Carmichael, I. S. E., 1973, P_{Total} , PH_2O and the occurrence of cummingtonite in volcanic rocks: Contributions to Mineralogy and Petrology, v. 40, p. 149–158, doi:10.1007/BF00378172.